2021

Finding Common Ground: The Common Marmoset as a Model to Accessing and Providing Insight into the Social Brain

Margaret Fabiszak

FINDING COMMON GROUND: THE COMMON MARMOSET AS A MODEL TO ACCESSING AND PROVIDING INSIGHT INTO THE SOCIAL BRAIN

A Thesis Presented to the Faculty of
The Rockefeller University
in Partial Fulfillment of the Requirements for
the degree of Doctor of Philosophy

by
Margaret M. Fabiszak
June 2021

FINDING COMMON GROUND:
THE COMMON MARMOSET AS A MODEL TO ACCESSING AND PROVIDING INSIGHT INTO THE SOCIAL BRAIN

Margaret M. Fabiszak, Ph.D.
The Rockefeller University 2021

Utilizing the immense strengths of the common marmoset (*Callithrix jacchus*) as a model organism, we executed three efforts with the common goal of revealing key insights into dissecting the social brain.

First, we examined the hypothesis that there is a neural, functional architecture underlying face processing. Faces form a unique category of stimuli that bridge visual perception and social cognition. They are processed in dedicated areas of cortex, face patches, which are organized into an interconnected network. While insight into neurons within face patches has been explored through extracellular electrophysiology, the functional architecture of local ensembles of cells has remained elusive. Recently discovered face patches in the lissencephalic common marmoset brain provide the cortical access necessary in order to employ optical techniques to resolve both the functional properties as well as the spatial organization of these neural ensembles. Unique to marmoset face patches, the cortical boundaries of these patches overlap with areas usually attributed to early stage visual processing. In particular, the occipitally located face patch "O" overlaps with V2, an area usually thought to be composed of neurons with tuning properties to low-level visual stimuli such as, but not limited to, orientation and direction. Here, in the anesthetized marmoset, we demonstrated the areal parcelization of function along the dimensions of low-level visual stimuli and high-level visual stimuli including faces, objects, and bodies using two-photon microscopy. We found that the functional architecture revealed best supports naturalistic stimuli processing more so than face processing. This suggests the interpretation that face patch "O" is a selective measure of recurrent activity or feedback activity into natural scene processing of faces rather than an area of pure face perception. As an area of natural scene processing, there may be cell-type specific populations supporting such segregation and suppression of low-level feature responses. We developed a novel approach to characterize the entire region using iterative antibody staining with volumetric immunohistochemistry.

From a genetic and circuits approach, social cognition has been implicated in numerous circuits across brain structures. One such circuit includes pyramidal neurons projecting from layer V of the medial prefrontal cortex (mPFC) to the nucleus accumbens (NAc), given its involvement in social-reward behaviors and depression in rodents and primates. This circuit presents an opportunity not only to study the genetic blueprint of a socially relevant circuit, but also to determine how it is conserved across rodents and non-human primates. Here we established retrograde viral Translating Ribosome Affinity Purification (retro-vTRAP), using techniques previously implemented only in rodents. retro-vTRAP enables sequencing of mRNA bound to EGFP-tagged polyribosomes from chosen projection neurons that have been virally labeled with an *EGFP-L10a* transgene. retro-vTRAP facilitates the study of gene expression patterns in specific neural cell types to be studied in the complex, heterogeneous tissue of the

cortex, shedding new light on transcriptional differences in cognitively relevant cells across species. We implemented retro-vTRAP in marmosets, macaques, rats, and mice and found a single conserved, enriched gene ontology set across marmosets and the rodents. This gene set is involved in negative regulation of endoplasmic reticulum stress induced apoptosis and is implicated in depression and mechanisms of treatment. This enrichment specific to this projection may be part of a genetic signature of this projection and provide functional modulation in times of social stress.

Lastly, from a developmental approach, we detailed a critical embryonic period of protracted growth resulting in a developmental delay in the marmoset compared to other species, relative to gestation length. This was revealed through use of high-resolution, serial ultrasound scans of developing marmosets. We demonstrated that this delay period occurs during gastrulation and before neural tube closure. During this protracted period, the amnion undergoes massive restructuring and growth, creating a unique opportunity to utilize this window to introduce genetic manipulations creating a proxy of a transgenic animal without conventional transgenic methodologies. This may be transformative to building more accurate models of disorders, particularly cognitive disorders that cannot be fully replicated in rodent models.

To James
To joy; to adventure
To those fighting to create a better world in uncertain times

"At that degree, equivalence encounters passionate understanding… In so far as it thinks it solves the paradox, it reinstates it intact. On this score, it is stirring. On this score, everything resumes its place and the absurd world is reborn in all its splendor and diversity.
But it is bad to stop, hard to be satisfied with a single way of seeing, to go without contradiction, perhaps the most subtle of all spiritual forces. The preceding merely defines a way of thinking. But the point is to live."
The Myth of Sisyphus, Albert Camus

"Form is certainty. All nature knows this, and we have no greater adviser. Clouds have forms, porous and shape-shifting, bumptious, fleecy. They are what clouds need to be, to be clouds. See a flock of them come, on the sled of the wind, all kneeling above the blue sea. And in the blue water, see the dolphin built to leap, the sea mouse skittering; see the ropy kelp with its air filled bladders tugging it upward; see the albatross floating day after day on its three-jointed wings. Each from sets a tone, enables a destiny, strikes a note in the universe unlike any other. How can we ever stop looking? How can we ever turn away?"
Upstream, Mary Oliver

ACKNOWLEDGMENTS
With sincere gratitude, I would like to acknowledge my advisor, Dr. Winrich Freiwald. His willingness to think broadly and graciousness to engage with every scientific idea I've had have been tremendous gifts over the past years. Thank you providing a level of opportunity I could have never imagined. It has been beyond a privilege being in your lab.

To my Faculty Advisory Committee members, Drs. Cori Bargmann, Vanessa Ruta, and Conor Liston. Thank you for always taking the time to guide my science and ensure that year-by-year, I grew as a scientist and as a person. You noted every hurdle before they arrived and motivated me to meet them with diligence and perseverance – always putting the science at the forefront and bringing life to meet it. Thank you to my external committee member, Dr. Afonso Silva, for sharing your immense knowledge of marmosets, imaging, and development.

To Dr. Olaf Andersen, Director of the MD-PhD Program, for crafting a community in which we all become better people and scientists for being a part of it. Thank you for taking a chance on me as an applicant to the program all those years ago. It has transformed every aspect of my life for the better. You provide countless words and actions to live by but two notable phrases include, "Compassion without knowledge is fraud. The rotisserie chickens do not just come flying to you."

Thank you to all the current and past individuals in the MD-PhD office who ensure from day one through n we are constantly supported and strengthened. Dr. Catharine Boothroyd, Renee Horton, Hanna Silvast, Dr. Benjamin Levitt, Dr. Ruth Gotian, and Joseph Washington.

To the Dean's Office at Rockefeller for supporting all of the students through graduate school in kindness, care, and steadiness. Dr. Sid Strickland, Dr. Emily Harms, Dr. Andrea Morris, Kristen Cullen, Marta Delgado, Stephanie Fernandez, and Cristian Rosario.

To the entire congregation of the Freiwald lab, past and present. The last six years have been transformed and enriched by each and every one of you.
†Willa Kerkhoff and †Dakota Blackman in particular for your tireless work TRAP project and your support during the tiring hours of the acute experiments.
‡Rohan Soman, the bridge between the Brivanlou and Freiwald labs, for opening the door to development.
To all the members of the lab with whom I worked closely throughout this thesis: Stephen Serene (Opzzy), Devany West (CaImAn), David Hildebrand (acute preparations), Farid Aboharb (batch analyses), Christina Pressl (tissue harvesting), Peter Schade (ultrasound annotation), Michael McPhee (ultrasound annotation), Julia Deere (primate clearing protocols).
To all additional current members in the lab who have created a diverse environment of inspiration: Minggui Chen, Ben Deen, Amir Farzmahdi, Sara Gannon, Geena Ianni, Monica Jimenz, Sarina Karmacharya, Sofia Landi, Karolina Marciniak, Ilaria Sani, Tomoki Suzuki, Lucas Tian, Yuriria Vazquez, Pooja Viswanathan, Elena Waidmann, Zetian Yang.

To all previous members of the lab who established creative and playful measures of the mind: Naphtali Abudarham, Philip Brandner, Monica Cano-Vinas, Akinori Ebihara, Clark Fisher, Max Friedrich, Violeta Gonzalez, Pablo Polosecki, Yifat Prut, Vatsun Sadagopan, Stefan Schaffelhofer, Caspar Schwiedrzik, Stephen Shepherd, Julia Swila, Bram van Vugt, Ilker Yildirim, Wilbert Zarco.

Alejandra Gonzalez, for providing support every single step of the way for each member in the lab, human and non-human alike. I will be forever grateful for your long nights staying with me during the acute experiments and your constant acts of selflessness.
Lihong Yin, for providing consistent structure in a chaotic world, always knowing exactly the right person to speak to, and ensuring we always had cake.

I owe an extraordinary amount to the generosity of collaborators who took time to teach me, work with me, and create life out of ideas.
Dr. Eric Schmidt – for motivating and mentoring every step of the TRAP project.
Dr. Ali Brivanlou, Zeeshan Ozair – for supporting the developmental project and highlighting its implications.
*Drs. Zhuhao Wu, Wei Wang, and Anna Kolstad – for the irreplaceable work you have done on the clearing protocols and antibody screening. You are titans. You once said, "Keep going." You'll never know how much that meant.
Drs. Hongbo Jia, Xingyi Li, and Arthur Konnerth – for helping build the two-photon microscope and supporting the transition of an electrophysiologist into the world of microscopy.
Drs. Kenichi Ohki and Masato Uemura at University of Tokyo – for viral plasmids for the tandem GCaMP6s construct.
Drs. Thomas Carroll and Matthew Paul at the Bioinformatics Research Core – for all of the bioinformatics analyses and humor.
Jim Petrillo, Peer Strogies, and Dan Gross in Precision Instrumentation Technologies – for training me and helping me to build whatever we could imagine together… and for the wedding rings.
Stephanie Marcus – for bringing MarmoCap to life and your steadfast kindness in coming to provide support at the end of each experiment.
Drs. Alison North, Christina Pyrgaki and the Rockefeller Bioimaging Resource Center – for their education, patience, and ingenuity with finding imaging solutions for the entire campus.
Drs. Jude Mitchell, Cory Miller, Antonio Souto, Nicola Schiel – for bringing me into the world of marmosets both in the lab and in the wild.
Drs. Alexendra Benevante and Ana Kour – for the generosity in starting our colony
Drs. David Leopold and Soo Huyn Park – for the discussions regarding face patches and providing the coordinates to target the occipital face patch.
Drs. Xiaoqin Wang and Xindong Song – for supporting multiple visits to learn from your incredible set-ups.
Dr. Takashi Nishida – for being our EEG consultant and introducing me to neurology.
Dr. Fernando Nottembohm, for all the lunch conversations and insight into nature.
Drs. Bijan Pesaran, Tony Movshon, Yan Wong, Maureen Hagen, Luke Hallum – for forming the NYU community that brought me to and first trained me in neuroscience. You have always held me to the highest levels of rigor in all aspects of life.

To the additional network of individuals who have provided conversation and feedback throughout these past six years.
Drs., Timo van Kerkoerle, Stephan Meyer, Emre Aksay, Alipasha Vaziri, Brandan Chen and Frank Tejera.
Veterinary Services and the entire Comparative Bioscience Center: Leslie Diaz, Stephanie Phillips, Catalina Echeverri, Sean Kelly, Skye Rasmussen, Ravi Tolwani, Jennifer Connor, Danielle Hall, Daniella Gonzalez, Eric Soto-Lemus, Chaya Goodman, David Powell, Mark Knight, Jorge Fajardo and the Husbandry team. Your dedication, care, and resourcefulness ensured that every experiment was held to exacting standards for to the benefit of all involved. It was a joy working with you all.
Billy Kitt and the CBC Custodial team. Thank you for your kindness and compassion. You would check in at 4:30 each morning to make sure we were doing well and still on our feet. It's the small things that mean so much.
Jeff Prout and Jim Sheridan in Plant Operations and Carpentry. Anna Heghes in Planning and Construction. Never a loose screw, or a wobbly shelf in sight. You turned a sketch and some hope into a lab full of potential.

Transylvanian Experimental Neuroscience Summer School. This graduate project would not have been possible without this tremendous summer course and the spark of creativity and humor it promoted in every experiment.

Summer students and rotation students: Eva Soto, Julia Deere, Jacob Weiss, Rob Fetcho, Yilun Ma, Samantha Phillips, Stephanie Marcus, and Devany West. Thank you for training me to be better, more generous, more understanding.

To steadfast friends all over the world – Baila Hall, Phil Nussenzweig, Kate Nothem, Laura Gainer, Casey Farin, Abe Katz, Ed Houston, Evan Hasbrook, Esther Kang, Jesse Amato-Grill, Josephine Cool, Gen Chartrand, Greg Cogan, and Adam Weiss. The Entering MD-PhD Class of 2012, the climbing crew (may we still get to the climbing grade equal to length of our graduate training), and to the Future of Care Community. Life really is all about the people.

To anyone I've missed, I thank you twice.

Funding sources: NRSA 1F30MH112351 NIMH, MSTP T32GM007739, Kavli NSI Project Grant, Simons Foundation SCCGB365002, Rockefeller Study Abroad Program, and the Karolinska Institute Nicholson Exchange

To all the wild ones. Sophistry, Tittup, Eclipse, Winston, Stanley, Electra, Hippo, Misty, Phosphorus, Quinine, Argentus, Captain Jack, Odin, Guggenheim, Chi-Chi, Einstein, Yitrium, Bob, Ross, Forest, Birdie, Uxorious, Zany, Yahoo, Mickey, Princess, Internazionale, Frank, Fleura, Fiorentina, Biscuit, Rex, Almond Joy, Lollipop, Marshmallow, Ness, Obelix, Derby, Swansea, Toulouse, Udinese, Valur, Cindy Lou-Who, Ebenezer Scrooge, Raptor, Trike, Coconut, Cashew, Crumpet, Dali, Goya, Duke, Duchess, Hershey, Cadbury, Bambi, Casper, Alvin, Ziti, Xacuti, Yogurt, Tookie, MM, Archie, and Calvin. You are the foundation of the research. I am forever indebted.

Most importantly, to my family. Our family brings us forward with us into the world, but how lucky am I that you have been with me every step of the way. Thank you,

Mom and Dad, for nurturing every dream, supporting every wild idea, and having boundless generosity. You serve as an inspiration to all of us. To my brother, who taught me the meaning of passion. Thank you for being unbendingly resolute in your convictions, and for always allowing me to tag along. To my grandparents, aunts, uncles, and cousins, thank you for building this legacy of our lives wound together. To the Chois, for bringing me into your family.

Most of all, to my husband, James. I am grateful for every absolute moment we have together. Thank you for creating a relationship where we constantly build each other stronger, allow ourselves the space to grow, and create unending support. You celebrated every experiment – the good, the bad, and the confusing. It made it all an adventure. This would not be possible without you. Thank you.

Lastly, let us not forget our dog, Sumo, who reminds us daily that we're just animals after all, and perhaps we should go outside just one more time today.

TABLE OF CONTENTS

LIST OF FIGURES

LIST OF TABLES

CHAPTER 1. Introduction

The emergence of complex social environments and the increasing behavioral demands on visual cues are thought to form two critical drivers of the dramatic expansion of the neocortex in primates (Belmonte et al. 2015; Hofman 2014; Solomon and Rosa 2014). In evolutionary comparison studies, the neocortex grew disproportionately more than other brain structures in primates when compared to prosimians or insectivores (Barton and Harvey 2000; Finlay and Darlington 1995). The results of this expansion can be studied from the multiple vantage points amongst them, the neural basis of sociality (Adolphs 2009; Dunbar and Shultz 2007; Platt, Seyfarth, and Cheney 2016; Sliwa and Freiwald 2017), behavioral implications (Altmann 1962; Brosnan, Schiff, and de Waal 2005; Burkart and Finkenwirth 2014; Koski et al. 2017), and molecular contributions (Robinson, Fernald, and Clayton 2008; Ross 2001).

These studies are often best set in models in which sociality bears impact on the natural ethology of the animal. Here, we will detail three such approaches in the common marmoset. The common marmoset (*Callithrix jacchus*) is a small, New World primate that diverged from the evolutionary lineage that produced apes and humans approximately 35 million years ago. Its prosociality, natural gaze behavior, and tractability with molecular techniques (Bezerra and Souto 2008; Burkart and Finkenwirth 2014; Mitchell and Leopold 2015; Mitchell, Reynolds, and Miller 2014; Sasaki 2015; Schiel and Souto 2017; Watakabe et al. 2014) prime the common marmoset as a new, and uniquely powerful model for the experimental exploration of multiple levels of the social brain.

The first approach detailed herein explored face processing as a model bridging social and visual perception. The second approach identified conserved neural circuits vulnerable in social disorders as a model for understanding the underlying role of these circuits in typically functioning structures. Finally, the third approach revealed developmental insights in the common marmoset toward the aim of being able to causally manipulate systems, often by utility of transgenic means. Although this is a standard approach in species such as the mouse, there remain barriers to adapting these methods in the marmoset largely due to an incomplete understanding of their development.

Each chapter details the establishment of using the common marmoset as a model for investigating the social brain across these systems of study from elucidating the functional architecture of a face patch, identifying genetic signatures of a conserved neural projection, and detailing embryonic development. Together, these create the foundation from which these levels of interrogation can be combined to form a holistic, tractable, and causal understanding of the social brain.

1.1 Face processing as an introduction to the social brain

The face processing system offers an intersection between social and visual perception. When a visual scene is presented to a primate and a face is perceived, the process of facial perception provides a rich set of related social information (Allison, Puce, and McCarthy 2000). When a face is seen, it is not only a process

of recognizing that, in general, two eyes, a nose, and a mouth comprise a face, but it is also a process of realizing that the angle of the head may indicate the direction of the individual's attention or that the teeth being bared may indicate displeasure. This entire process provides an insight into social cognition (Brothers 2002) wherein facial perception results in a complex and socially specific response.

The fact that face processing networks have been found in multiple species suggests that the neural architecture for face processing may be evolutionarily conserved. In the human, at least four specific areas have been found including the fusiform face area (FFA), anterior inferotemporal area (aIT), the occipital face area (OFA), and the superior temporal sulcus face area (STS-FA). These four areas encode different face properties including face identity, more specific identification, physical face parts, and gaze direction (Kanwisher, McDermott, and Chun 1997; Kanwisher and Yovel 2006; Kriegeskorte 2007; Rossion, Hanseeuw, and Dricot 2012). Face perception in the rhesus macaque (*Macaca mulatta*) is similarly parcellated into discrete areas of cortex that exhibit a specific response preference for face stimuli. These areas are termed patches and have been found in both the temporal and frontal lobes. Although there was a precedent for experiments using single neurons recordings to report neurons specific to faces (Desimone and Gross 1979; Perrett, Rolls, and Caan 1982), it was not until the advent of using functional magnetic resonance imaging (fMRI) that it was revealed that macaques have discrete patches in both the temporal and frontal lobes (D. Tsao et al. 2008; D. Tsao and Freiwald 2003). Combining fMRI with electrophysiological methods, it was determined that 97% of the cells recorded within these patches exhibit face selectivity often with latencies of less than 100 ms (D. Tsao et al. 2006). Face patches in the temporal lobe furthermore show a hierarchical connectivity pattern (Moeller, Freiwald, and Tsao 2008) and encode different face properties. Neurons in the middle patches have tuning curves for specific head orientations, neurons in a more anterior patch show mirror symmetry for a particular orientation, and neurons in the most anterior patch show identity specific responses (Freiwald and Tsao 2010; Freiwald, Tsao, and Livingstone 2009). This structure of organization into discrete cortical that represent different functional areas properties has been shown to exist in human face perception areas (D. Y. Tsao, Moeller, and Freiwald 2008), suggesting that not only is the presence of a dedicated cortical network for face processing evolutionarily conserved, but also that there may be a particular computational mechanism distributed between these patches and throughout the temporal lobe as a whole (Bao et al. 2020; Chang and Tsao 2017).

Experiments exploring the neural basis of an animal's ability to recognize faces have been shown in numerous additional species including sheep and canines (Dilks et al. 2015; Kendrick 1991; Leopold and Rhodes 2010). Furthermore, recent work has been done in the common marmoset (Hung et al. 2015) showing the presence of face patches in the temporal lobe along a posterior to anterior axis in a similar manner to the face patches found in humans and macaques (Fig 1.1).

In order to elucidate the mechanism by which face perception occurs in the marmoset, we can build on the robust history of research in the visual system

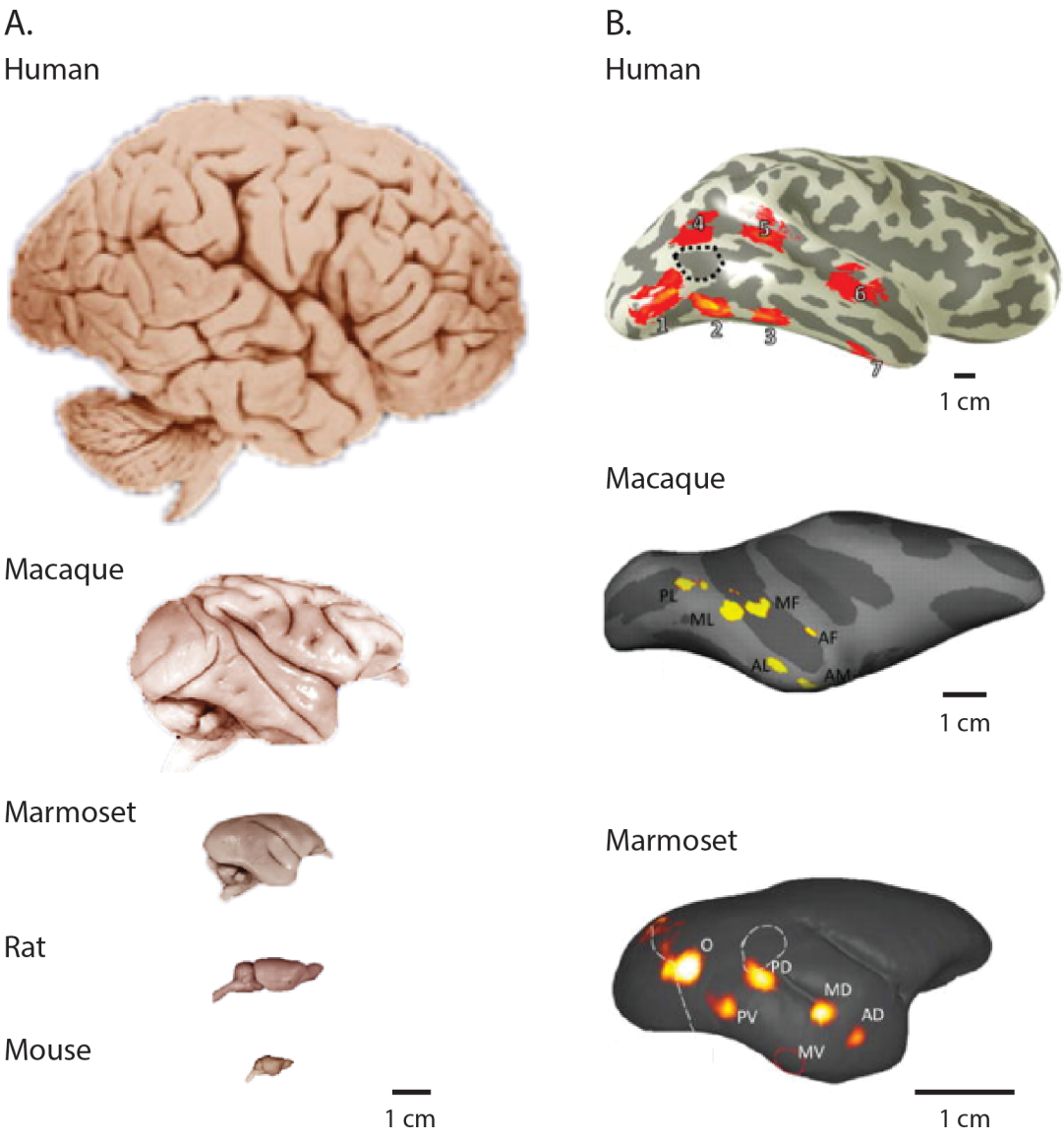

Figure 1.1 Comparison of selected mammalian brains.
A. Gross dissection images of lateral view of right hemisphere to same scale. Images taken from University of Wisconsin Walker Collection (neurosciencelibrary.org). B. Face patch networks identified in human, macaque, and marmoset brains. Human and macaque brains are inflated surfaces where the dark gray color represents cortical surface in sulci. Heat maps demonstrate localized face patches. Image adapted from Weiner and Grill-Spector, 2015.

and key principles that have been found to hold not only across different cortical areas but also across species. Just as early vision is understood in large part by how visual features are mapped onto the surface of primary visual cortex (D. H. Hubel and Wiesel 1968), this must be established for the face processing areas. Further, the dynamics of a local population impact both the development and the maintenance of these maps. These mechanisms have been studied most extensively in primary visual cortex (Angelucci and Bressloff 2006; Ringach, Shapley, and Hawken 2002) and depend both on the excitatory and inhibitory contributions to the network (Isaacson and Scanziani 2011; Shapley, Hawken, and Ringach 2003). Projections within and between areas contribute to shaping the receptive fields and modulating the properties of each of the overlying maps (Angelucci et al. 2002; Bosking et al. 1997; Gilbert and Wiesel 1989; Lund 2003; Shmuel et al. 2005). Furthermore, and perhaps most profoundly, there remains active debate regarding how cell selectivity emerges amongst inhibitory and excitatory neurons (Bonin et al. 2011; X. Chen et al. 2011; Hofer et al. 2011; Kerlin et al. 2010; Lee et al. 2012; Rochefort et al. 2011; Tan et al. 2011). It is an open question whether or not these cell type selectivity and mapping mechanisms exist in a face patch.

1.2 Selection of a tractable neural projection to interrogate conserved signatures of the social brain

In terms of detailing the genetic signatures of neural circuits critical to social behavior, there have been recent advancements in investigating these circuits across molecular, genetic, functional, and behavioral modalities (Bakken et al. 2020; Gunaydin et al. 2014; Heiman et al. 2008; Shah et al. 2016; D. A. Stanley and Adolphs 2013; Tervo, Hwang, Viswanathan, Gaj, Lavzin, Callaway, et al. 2016). However, the limitations of current technological approaches have thus far prevented an integrated view of social circuits, instead relying on disparate techniques to probe different levels of organization across species. Investigating the common circuits that drive observable behaviors across species can reveal both species-specific and shared characteristics of social circuitry that have emerged along the evolutionary trajectory. To achieve this insight, there exist the dual necessities of adapting genetic techniques to be compatible across species and the implementation of this novel, adapted technique in a tractable neural circuit conserved across all species studied. One such social circuit is the corticoaccumbal projection from the medial prefrontal cortex to the nucleus accubens (Bicks et al. 2015; Riga et al. 2014; Xu et al. 2019), which has been shown to be conserved in mice, rats, marmosets, and macaques (Z. Liu et al. 2016; Roberts et al. 2007; Wise 2008). Given the identification of this conserved projection, it is then possible to combine an engineered retrograde virus to anatomically isolate the targeted corticoaccumbal projection population (Tervo, Hwang, Viswanathan, Gaj, Lavzin, Callaway, et al. 2016) with a molecular tool designed to characterize the genetic signature of a projection known to be relevant to the social brain across species (Heiman et al. 2014).

1.3 Developmental insights facilitate the foundation of enabling causal manipulations of the social brain

Ultimately, the insights from probing functional organization and genetic identification of relevant neural networks will require causal testing through inducing molecular and genetic changes to both manipulate and monitor the neural activity. This level of manipulation is frequently conducted through the utility of transgenic animals in classic animal models such as mice, flies, and worms (Berkowitz et al. 2008; T. R. Kumar et al. 2009; Venken and Bellen 2007). Although it is possible to create transgenic marmosets, the high degree of difficulty limit its utility (Sasaki 2015). A more comprehensive knowledge of early stages of marmoset development is necessary to both monitor potential transgenic success and reveal any opportunity of intervention to facilitate causal manipulation of the neural activity.

Throughout this thesis, we first demonstrated the functional architecture of an overlapping area of secondary visual area, V2, and the occipital face patch, "O," through the combined application of widefield imaging and two-photon microscopy. We have created and established coregistered, volumemtric immunohistochemistry to provide further evidence into the functional architecture of this area. We then utilized the marmoset in conjunction with three other species to establish a single tool for dissecting genetic signatures of a conserved neural circuits across wildtype species. Lastly, in efforts to further establish the common marmoset as a tractable model for investigations linking together findings from humans to mice, we establishd an atlas of embryonic and fetal marmoset development that revealed a period of embryonic developmental delay providing a window of opportunity to induce somatic genetic manipulations in an otherwise wildtype animal. Together these experiments aim to further establish the common marmoset as a model by which it is possible to dissect the social brain across genetic and functional approaches.

CHAPTER 2. Functional architecture of natural stimuli representations in early visual areas in the common marmoset

*Portions of the volumetric immunohistochemistry work in this chapter were accomplished with collaborators in the Wu Lab, Zhuhao Wu and Anna Kolstad. MF performed all two-photon related surgeries, experiments, and analyses. ZW created MarmoClear. AK and MF performed antibody screen. AK optimized sequential staining protocol. MF created coregistration pipeline, conducted analyses, created figures.

2.1 Cortical organization for feature representation

Elegant experiments established the column as the fundamental unit of neocortex (Mountcastle 1957, 1997). Columns can then be grouped together in a recursive fashion such that multiple variables can be mapped onto the cortical surface. A key example of this multifunctionality can be found in the primary visual cortex where ocular dominance, contrast, and orientation of stimuli are individually mapped onto the same area of cortex in such a manner that they can be deconvolved to their original representations (D. Hubel and Wiesel 1974; Wiesel, Hubel, and Lam 1974). The extent to which these maps exist in early visual cortex of the marmoset suggests that ocular dominance columns have a more idiosyncratic presence but that orientation columns are highly preserved (Chaplin, Yu, and Rosa 2013; Solomon and Rosa 2014). Given that the face patches are found in the ventral stream of the visual pathway (Kravitz et al. 2013) it may be a preserved feature that representations of the visual world have their different properties mapped in a systematic pattern. Work in the macaque suggests that particular face properties, including orientation and identity, are represented in specific groupings. These groupings may be the dimension along which cells within face patches are mapped into cortical columns that have been shown to encode complex objects (Tanaka 2003).

That the face patch network extends more posteriorly in the marmoset (Hung et al. 2015) offers the opportunity to investigate the architecture of a face patch that overlies a more well parcellated area of visual cortex, V2 whose color blobs, orientation columns, angel representations, and disparity tuning have all been explored (Ito and Komatsu 2004; McLoughlin and Schiessl 2006; Roe, Fritsches, and Pettigrew 2005; Ts'O, Roe, and Gilbert 2001; M. F. Valverde Salzmann et al. 2012). Building on this known architecture in V2, it is then possible to better tease apart what the specific signal might be that underlies the representation of faces in this area. Indeed, other studies have shown V2 to be specific to natural textures and respond to naturalistic scenes in macaque studies (Freeman et al. 2013; Willmore, Prenger, and Gallant 2010), but the specific architecture of these intercalated neurons has not been revealed.

Furthermore there remains active debate regarding how cell selectivity emerges amongst inhibitory and excitatory neurons (Bonin et al. 2011; X. Chen et al. 2011; Hofer et al. 2011; Kerlin et al. 2010; Lee et al. 2012; Rochefort et al. 2011; Tan et al. 2011). In macaque V2, it is even suggested that a signature of neurons preferring naturalistic scenes is their stronger suppressive tuning as measured with extracellular electrophysiology (Willmore, Prenger, and Gallant 2010). It is an open question whether or not these selectivity and mapping mechanisms exist in

a face patch. Putative, occipital face patch "O" is ideally situated to probe this intersection between isolated visual components and social representations.

In establishing this approach, it is critical to be able to test these low-level visual stimuli and parameterized high-level stimuli in an equitable manner in which the impact of one does not overwhelm the other. Social cognition is a complex phenomenon that spans numerous brain regions through the brain's interconnected feedback and feedforward pathways, and may provide recurrent information into each processing area. Thus, it is conceivable that the neural activity in a face processing area will be heavily modulated and altered by brain-wide responses to the face. To reduce these difficulties, we will take advantage of the fact that the face processing areas are responsive to visual stimuli in both awake and anesthetized states (Ku et al. 2011). The anaesthetized state offers the advantage to better isolate the perceptual component, as there can be no behavioral response, and additionally, maximizes the amount of data that can be collected. This is not without significant drawbacks, as it is known that anesthesia disrupts neural vascular coupling, network communication, and alters perception of the environment in dose-dependent, localized manners (Bonhomme et al. 2019; Junjie V. Liu et al. 2013) and can greatly impact the signals recorded in each area. Nevertheless, it allows the opportunity to better control the activity baseline and measure perturbations directly related to exogenous stimulation (Bourne and Rosa 2003).

We conducted acute experiments in which the marmoset was anesthetized and placed on ventilation for the duration of the experiment. These experiments generally lasted 3 – 5 days with an average recording time of 48 hours.

Upon finishing functional data collection, it was critical to determine the cell type identity of the component ensembles of active cells to reveal the interplay between molecular identity and functional specificity. As a result, recorded brain areas were segmented and processed through novel volumetric immunohistochemistry techniques utilizing aqueous clearing techniques such that the tissue can be re-stained and processed iteratively. Volumetric immunohistochemistry facilitates the complete reconstruction and coregistration to the functional volumes without morphological deformation or tissue loss common to other techniques.

2.2 Experimental approach to investigating socially relevant stimuli in the common marmoset

We targeted a field of view that covered face patch "O" and V2, due to the unique overlap of low-level and high-level visual processing in this area as well as its accessibility as the most dorsally located face patch. We injected a genetically encoded calcium indicator that had been designed specifically for use in marmosets (Uemura et al. 2018). Specific to this construct, the introduction of a second GCaMP6s transgene in tandem with the first separated by a p2A linker (Fig 2.1.A, left) appears to provide a robust calcium imaging signal without resorting to driving expression to an extent so highly that it damages the cells and forms nuclear inclusions. The underlying mechanism for this is not fully understood, but from personal communication with the Ohki lab, it appears that

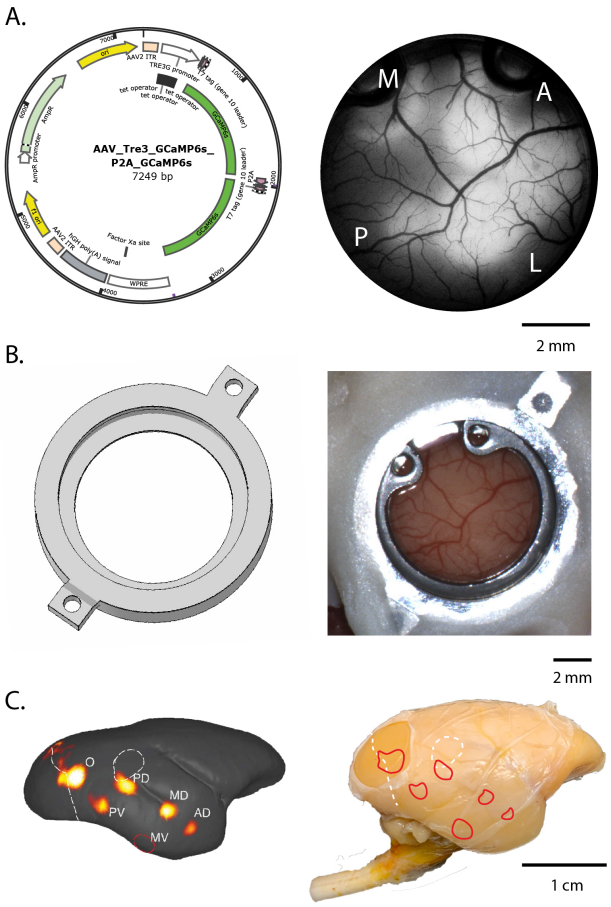

Figure 2.1 Experimental preparation for imaging V2 and face patch O
A. Custom tandem GCaMP6s vector provided to us courtesy of the Ohki lab (left). The transgene casset is under a tet-off driver such that it must be co-injected with a tTA virus. If desired, administering doxycycline can inhibit production of the GCaMP6s transgene. Vector map is made using SnapGene. Imaging field illuminated with 470 nm LED light illustrating expression of the GCaMP6s construct (right). Anterior, Posterior, Medial, and Lateral are indicated with initials in white. B. 3D rendering of custom made imaging windows based off of a design provided to us by the Fitzpatrick lab (left). Implanted window is an assembly of an external housing milled from aluminum, 10 mm #1.5 glass coverslip, and a removable retaining ring to adjust depth of window (right). There is a sheet of artificial dura between the assembly and the brain to further protect the tissue and prevent any immune reaction to the assembly components. C. Adapted from (Hung et al. 2015), here we show the face patch network highlighted in orange on the inflated marmoset brain (left). We superimpose the outlines of the face patch network onto one of our fixed experimental brains with the dura still intact (right). The most posterior face patch O fits within our window of view. White dotted lines indicate the border between V1 and V2 as well as area MT.

non-human primate neurons are more vulnerable to this than compared to mice. As such, we made six unilateral injections in each experimental animal to cover V2 and face patch "O" (Fig 2.1.A, right). Details of virus and injection methods can be found in the Methods section. Upon waiting 3-4 weeks for transduction of the virus, we then implanted a custom designed imaging chamber assembly (Fig 2.1.B) that flexibly allowed for depth to be adjusted over a 0.5 mm range and easily enabled the window and accompanying artificial dura to be removed and replaced within the chamber in case of edema, bleeding, or foreign body contaminants. We targeted this chamber to area V2 and face patch "O" using stereotaxic coordinates (AP -10 mm, ML +6 mm) provided to us in communication with the Leopold Lab (Hung et al. 2015) and confirmed location by *ex vivo* gross dissection and examination (Fig 2.1.C).

We established a rich stimulus set to be able to adequately drive neurons in this area based on previous reports (Roe, Fritsches, and Pettigrew 2005; Solomon and Rosa 2014) and also test our hypotheses regarding the arrangement of segregated responses to social stimuli. Details on stimuli creation are found in the Methods section. Briefly, we constructed low-level visual stimuli of periodic gratings and retinotopic mapping (Fig 2.2.A, B). In order to probe the basis of face representation, we created a localizer consisting of set categories of stimuli similar to those used in macaque studies (Fisher and Freiwald 2015; D. Tsao et al. 2006). We created sets of faces, bodies, objects, and face features (Fig 2.2.C), normalizing for high-level content such as gender, familiarity (Landi and Freiwald 2017), and object rotation (Freiwald and Tsao 2010), as well as low-level features such as contrast, luminance, and spatial frequency (Willenbockel et al. 2010). We then established three additional control sets of stimuli. The first was a set that distorted the internal statics of our localizer stimuli through the production of diffeomorphs and metamers (Fig 2.2.D). Diffeomorphs are images that retain the basic low-level visual content of the original form while removing its meaning. A maximally permuted diffeomorph should no long be able to be distinguished as its original form, but will have the same local feature structure as the original form (Stojanoski and Cusack 2014). Alternatively, we also created metamers of these images. Metamers are images that retain the meaning or percept of the original form, but are actually different images (Freeman and Simoncelli 2011). We created sets of diffeomorphs and metamers each with different degrees of permutation away from the original localizer set to determine if there was something unique to the perceptual meaning of an image or its underlying scene statistics that could possibly drive responses in a dedicated region. Lastly, we created a set of marmoset face blocks constructed from bars and gratings in order to control for whether or not a response in this area specific to a face percept or if the response was instead to linear structures of faces approximated by optimally suited V1 and V2 stimuli of oriented bars (Fig 2.2.E). These block faces also served as a control for determining if responses to faces could be elicited without the low-level curvilinear features known to drive visual cortex (Yue et al. 2014). The block faces were rotated to match the rotations existent in the localizer set and were also oriented to match the different orientations of the periodic gratings. There was a companion control set of blocks in which the component features of the block faces were rearranged to retain the same visual content but remove any perceptual meaning.

Figure 2.2 Stimuli sets
A. Orientations of drifting gratings. Each stimulus is an orientation step of 45° from any other orientation. Each orientation stimulus can drift in either direction such that taken together there are 8 possible options of stimuli presentation. These stimuli are shown at full visual field. B. Retinotopy consists of smaller 20° drifting gratings that tile the entire visual field. C. Faces, bodies, objects, and features form a localizer for these sets. All are normalized. D. Diffeomorphs and metamers are arranged along an axis where the center is minimum permutation, and therefore statistically and meaningfully most similar to the original forms. Any movement along this line is a change in local statistics, but both algorithms maintain a closer statistical commonality to the original form near the center and have greater differences at maximal permutations. Whereas, moving left, toward maximal permutation of diffeomorphs, the images lose their perceptual meaning, and moving right, toward metamers, images retain their perceptual meaning. E. Block faces and their controls are comprised of short, oriented bars and arranged to either create the percept of a face or only a collection of meaningless bars. They have rotations and orientations to match localizer images (B) and orientations (A), respectively.

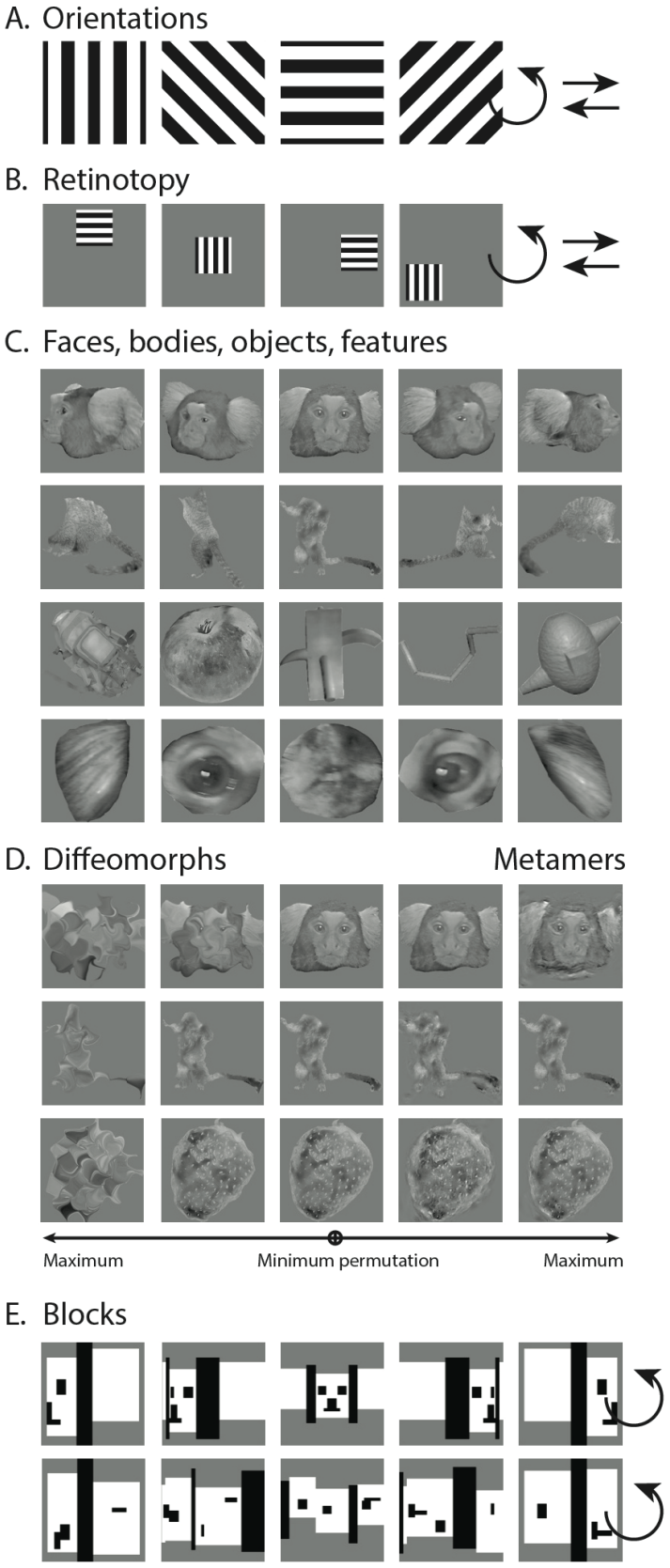
A. Orientations
B. Retinotopy
C. Faces, bodies, objects, features
D. Diffeomorphs
Metamers
Maximum
Minimum permutation
Maximum
E. Blocks

After creating the stimuli and technical approach, it was then feasible to determine how a class of socially relevant stimuli was encoded in a neural population in a cell-type dependent manner. We focused exclusively on area V2 and face patch "O", to determine whether there was an underlying functional architecture of spatial organization and cell-type specificity supporting responses to social stimuli.

2.3 Functional specificity within a targeted area

We first asked whether it was possible to establish a global map of the area's functional specificity and replicate what had been shown in other studies in our work. We proposed that with GCaMP6s expression present across the entire window (Fig. 2.3.A), it would be possible to run a wide field imaging (Fig. 2.3.B) contrast experiment in which we measured the change in fluorescence in response to each stimulus and then subtracted out a baseline cocktail of all other stimulus responses (Wang, Tanaka, and Tanifuji 1996). Stimuli were all presented binocularly to the animal and were located as close to the fovea as possible. Animals were refracted both prior to the experiments and during the experiments to provide starting values for the lenses provided to refract their eyes upon the screen. Throughout the experiment, we monitored the eyes to ensure no anesthetic induced shift or corneal damage occurred. We hypothesized that we would be able to locate the V1/V2 border from noting the point at which the orientation columns increase in size (Roe, Fritsches, and Pettigrew 2005) during a contrast with orientations. This was shown to be effective as we established the orientation tuning map for this area (Fig 2.3.C) and revealed a clear distinction of the V1/V2 border.

Knowing from previous literature that the occipital face patch "O" overlapped with V2, we next ran a contrast in which the responses to faces, objects, and bodies were each contrasted with the mean response to the other stimulus categories. The colorized map indeed showed a predominant activity profile for faces and bodies more so than objects (Fig 2.3.D.i.). Further, when we compared each individual map, it was apparent that there were both overlapping and non-overlapping areas that responded to faces and bodies. The more medial, anterior section of the field was more selective to faces and the lateral portion of the field responded more to bodies (Fig 2.3.D.ii.). At this wide scale, however, it was not possible to appreciate whether any of these orientation responses or responses to faces, objects, and bodies were the aggregate responses of collective activity or if single neurons responded selectively in the same manner.

2.4 Reponses of components demonstrate category clustered, graded responses

To record at the single cell scale, we performed two-photon calcium imaging while presenting the full battery of stimuli to the animal's eyes. We targeted layer 2/3 of the cortex and selected a plane of imaging approximately 200-300 um deep from the surface. Using two stacked goniometers in opposite axes in conjunction with the rotatable nosepiece, we ensured that the plane of imaging was normal to the objective.

Figure 2.3 Wide field imaging reveals orientation tuning map and preference for faces, bodies
A. Field overview within an imaging window illuminated with 470 nm light to reveal expression area the virally induced GCaMP6s. Anterior, Posterior, Medial, Lateral are indicated by their respective letters. B. Wide field imaging schematic in which there are four illumination options. Only one illumination option can be utilized at a time in the current configuration. C. i. Color coded, merged response map for four orientations. The color wheel indicates each orientation. White dotted line is the V1/V2 border. ii. Individual change in fluorescence maps for each orientation as indicated by the color of their outer ring. D. i. Color coded, merged response map for faces, objects, and bodies. The color wheel indicates each category with blue, faces; green, objects; and pink; bodies. White dotted line is the V1/V2 border drawn over from C. ii. Individual change in fluorescence maps for each stimulus group as indicated by the color of their outer ring. All color maps have been clipped so that their most intense pixel is clipped at the saturation of their assigned color scheme. As a result, these maps indicate only location of relative responses, but not intensities of relative responses.

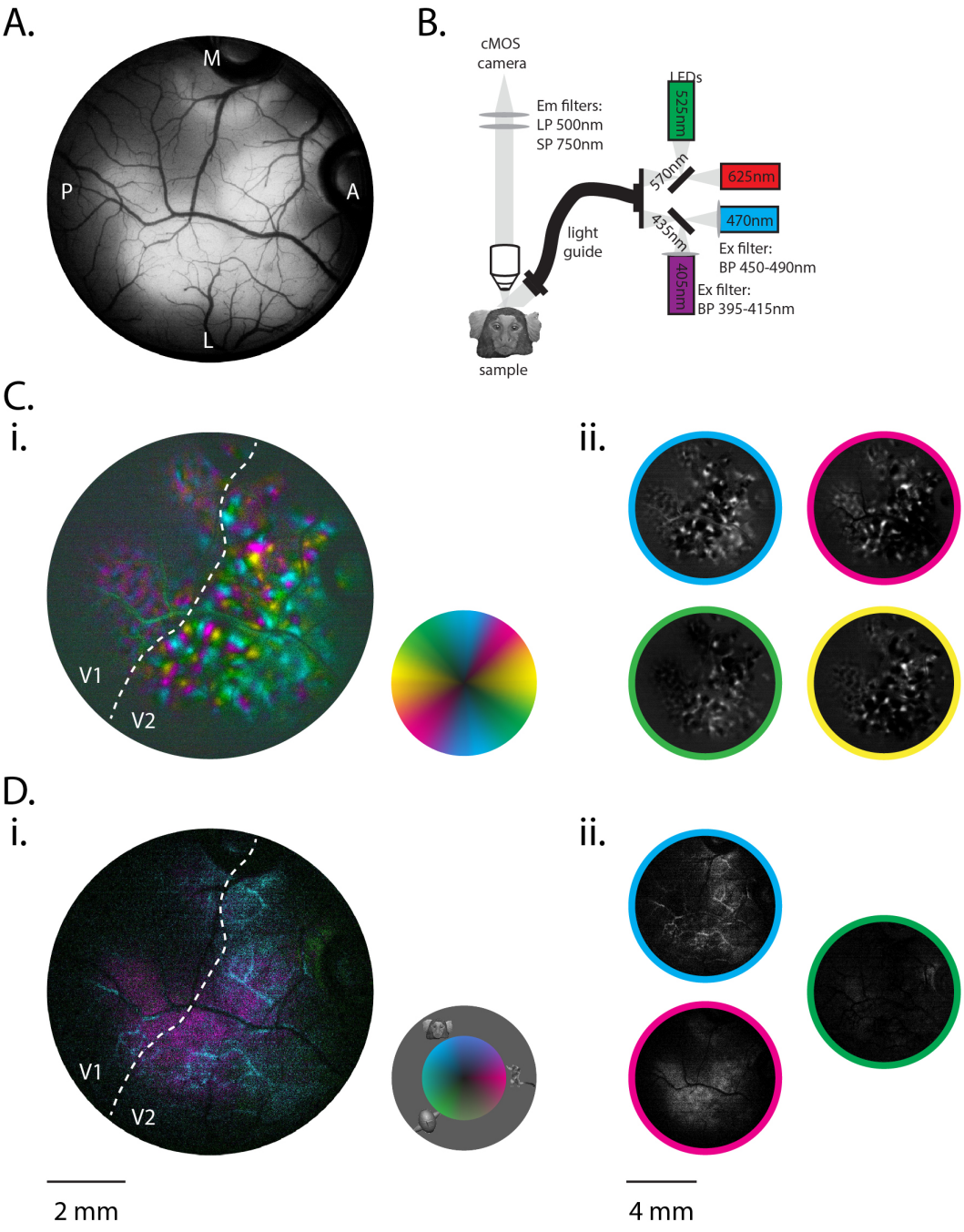
A.
M
P
A
L
B.
cMOS
camera
Em filters:
LP 500nm
SP 750nm
LEDs
525nm
570nm
625nm
470nm
435nm
light
guide
Ex filter:
BP 450-490nm
405nm
Ex filter:
BP 395-415nm
sample
C.
i.
V1
V2
ii.
D.
i.
V1
V2
ii.
2 mm
4 mm

For each imaging site, we recorded 1,616 successful trials, which had 4-8 repeats per stimulus depending on the stimulus type. Trials in which there was any movement in the imaging field or delay in one of the control computers were discarded. We successfully performed this full battery of experiments 9 times across 2 animals, S and T. Fields were labeled with the indicator of the animal and injection site. The health of the fields in animal S were marginally better as there had been some bleeding and edema in T. Nevertheless, we were able to evoke visual responses across both animals and extract 4,671 total components, or putative neurons, across all 9 fields (Fig. 2.4) using the CaImAn preprocessing pipeline (Giovannucci et al. 2019). Details related to fluorescence extraction are found in the Methods section. We accepted all 4,671 components into our analyses, but noted that the components found on a grid structure were most likely unfiltered neuropil contributions.

Upon extracting all components, we then calculated individual tuning curves per component (Fig 2.5.A). Given that the orientation stimuli rotated around 360°, a single orientation was always presented twice, but the drifting grating moved in opposite directions. As a result, in the tuning curves, we often saw two peaks that corresponded to two orientations separated by 180° indicating the component's preferred orientation and preferred direction. Each component's identifier was assigned based on spatial proximity. We garnered some indication of local clustering by examining batches of tuning curves with closely related identifiers (Fig. 2.4.A, right).

To better visualize a single component's response to many stimuli, we plotted the averaged change in fluorescence across time for every stimulus presented per cell (Fig 2.5.B) and created a peri-stimulus time histogram (PSTH) of change in fluorescence. As was readily apparent from the five representative components in Fig 2.5.B., different components responded preferentially to some stimuli more than to others. For example, c295 responded only to specific orientations, as indicated by the red stripes at the top of the column. c29 and c354 were much noisier than the other components but still displaed some grouping of consistent red indications of activity to retinotopic stimuli and diffeomorphs, metamers, respectively. Likewise, c296 showed selectivity for specific stimuli in the diffeomorphs, metamers set and finally, c291 showed predominant activity mostly during the set of faces, objects, bodies, and features. Interestingly, the only stimuli that were on for a full 2 s were the orientation stimuli. All other stimuli were on for only 0.5 s, but displayed much longer time courses, specifically in the grouping of faces, objects, bodies, and features. To better illustrate a component's stimulus preference, we collapsed these PSTH values into an average per component and plotted their mean, rank-ordered change in fluorescence (Fig 2.6).

Here, we better appreciated that components' responses are clustered with stimuli or categories driving similar levels of activity in the components. Interestingly, these components demonstrated a graded response to most stimuli, but with clusters of preferred stimuli at the highest cluster the rank-order and clusters of anti-preferred stimuli the bottom of the rank-ordered list of stimuli. The gradation of the change in fluorescence may be statistical by product of a

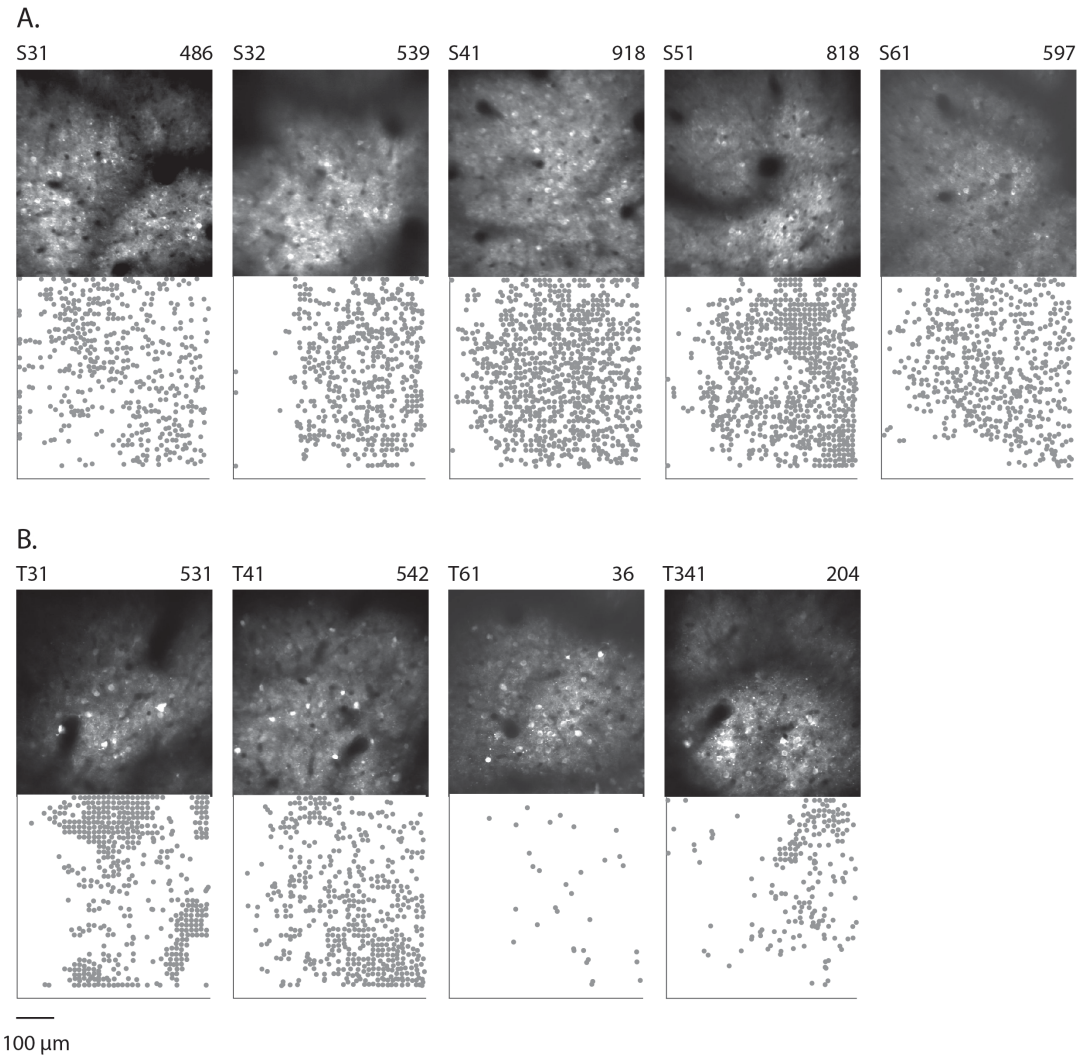

Figure 2.4 Field maps and extracted components locations
A. Five field maps for animal S. Each map is labeled with the name of the field, which is a combination of the animal indictor and the injection information (for example, S31). Indicated in the upper right corner of each map is the total number of components extracted from the field. The field images are average intensity projections of 60 seconds of recording in reach region and then brightness adjusted to scale the brightness of each image between the peak and minimum values. In the bottom row, there is the centroid of each detected component plotted in the same spatial scale as the field map. B. Same as A, but for animal T.

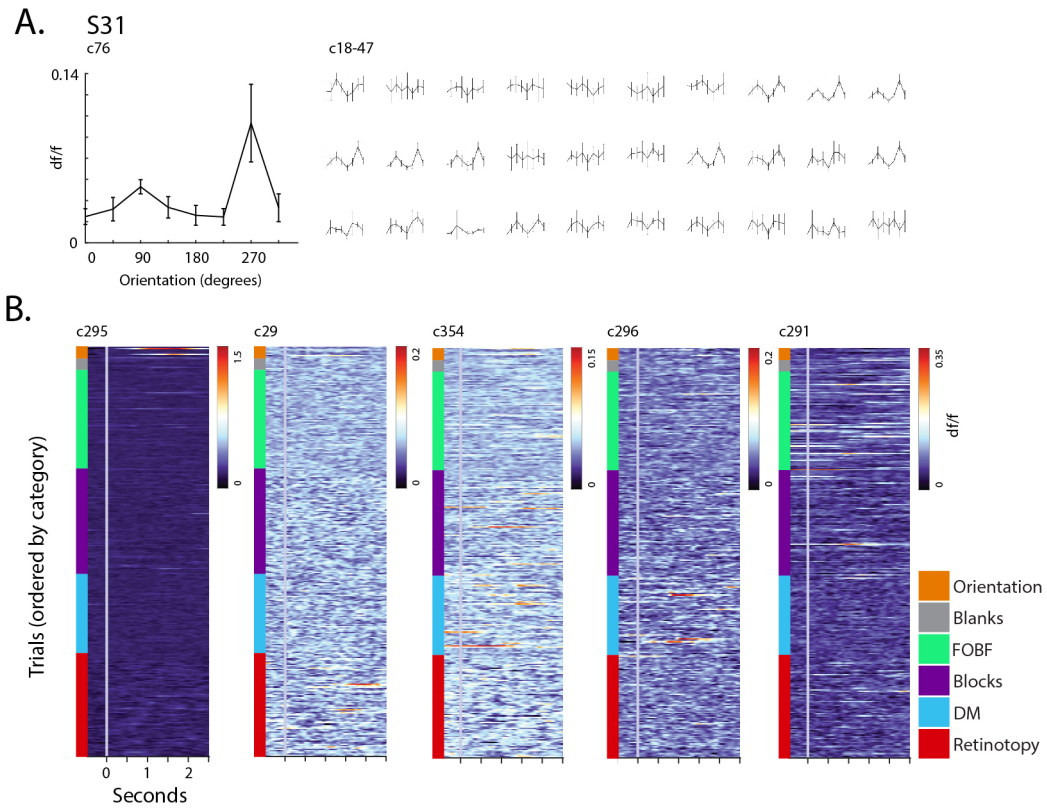

Figure 2.5 Orientation tuning curves and representative PSTHs
All data in this graph are from field S31. The individual components from which these data are taken are indicated by a "cNumber." A. A representative tuning curve for a single component. Change in fluorescence is measured against each stimulus' orientation. Each tuning curve is averaged over 8 trials. Error bars are SEM. The inset on the right demonstrates tuning curves for a larger population of components. B. Peri-stimulus time histograms of change in fluorescence. Plotted from -0.5 s stimulus onset to 2.5 s, all trials are aligned to 0 s as indicated by the vertical gray bar. Each row is a single stimulus type. The color of the row indicates its change in fluorescence, scaled to the heatmap color bar max and minimum per component. Every row is the average of 4-8 trials. Rows are clustered into categories from top to bottom. The colored blocks to the left of each row indicate the categories to which the stimuli belong. FOBF: Faces, objects, bodies, features; DM, Diffeomorph, metamer.

noisy signal; however, the stimulus category clustering suggested that these components had meaningful responses. Further, given that the trend held in both rank-order lists of individual stimuli and stimulus categories, for subsequent analyses we collapsed all stimuli into grouped categories.

Note that this categorization scheme allowed for there to be more than one category per color, just as in the case of stimuli of orientation 0° and orientation 180° being combined to form just one of four categories in the orientation group. However, no single stimulus was allowed to belong to more than one category so that there was no duplication or double counting of stimulus contributions.

These two figures demonstrated that individual components responded selectively to particular stimuli. When the stimuli were collapsed into categories, the components maintained the same overall trend in the data. Thus far, we only examined individual component responses, but insight into organization likely required looking at the population level.

2.5 Functional mapping reveals dedicated areas to naturalistic stimuli

Given that we were in area V2, a basis by which other organizational structures could be measured was the presence of orientation tuning columns. To reveal this structure, we took the peak of the tuning curves shown in Fig 2.5.A. and assigned each component a color corresponding to its peak orientation. We then plotted the spatial locations of all components with their assigned colors (Fig 2.7). Plotting these components together, we were able to recreate orientation columns. These orientation columns were strongly segregated across all fields in animal S whereas animal T displayed weaker clustering. This rose the question of whether or not these components indeed responded more preferentially to a stimulus category not captured here. We then asked if we could better determine the principles of organization in this area by looking more broadly across categories.

To answer this, we performed a Kruskall-Wallis test with a Dunn's post-test for multicomparison correction for subsets of categories of interest across all components. Given the delayed time courses for some stimuli responses in Fig 2.5.B, we elected to do this more strict, non-parametric test to allow for non-gaussian populations of responses. We set a threshold at $p = 0.05$ for identifying components with significant responses to one category over the other. We then performed a step down test to identify which significant category, if any, had the highest mean response. All tests were run on subsets of categories in which there were no overlapping items between categories (Fig 2.8).

We first tested whether or not there were any components that significantly preferred orientation stimuli, faces, objects, or bodies (Fig 2.8.A). Interestingly, we found that even though all of the maps in animal S displayed strong orientation tuning maps, that some of the cells indeed were more selective to faces, objects, or bodies. However, at the population level, significantly more cells responded preferentially to orientations than to the other three categories.

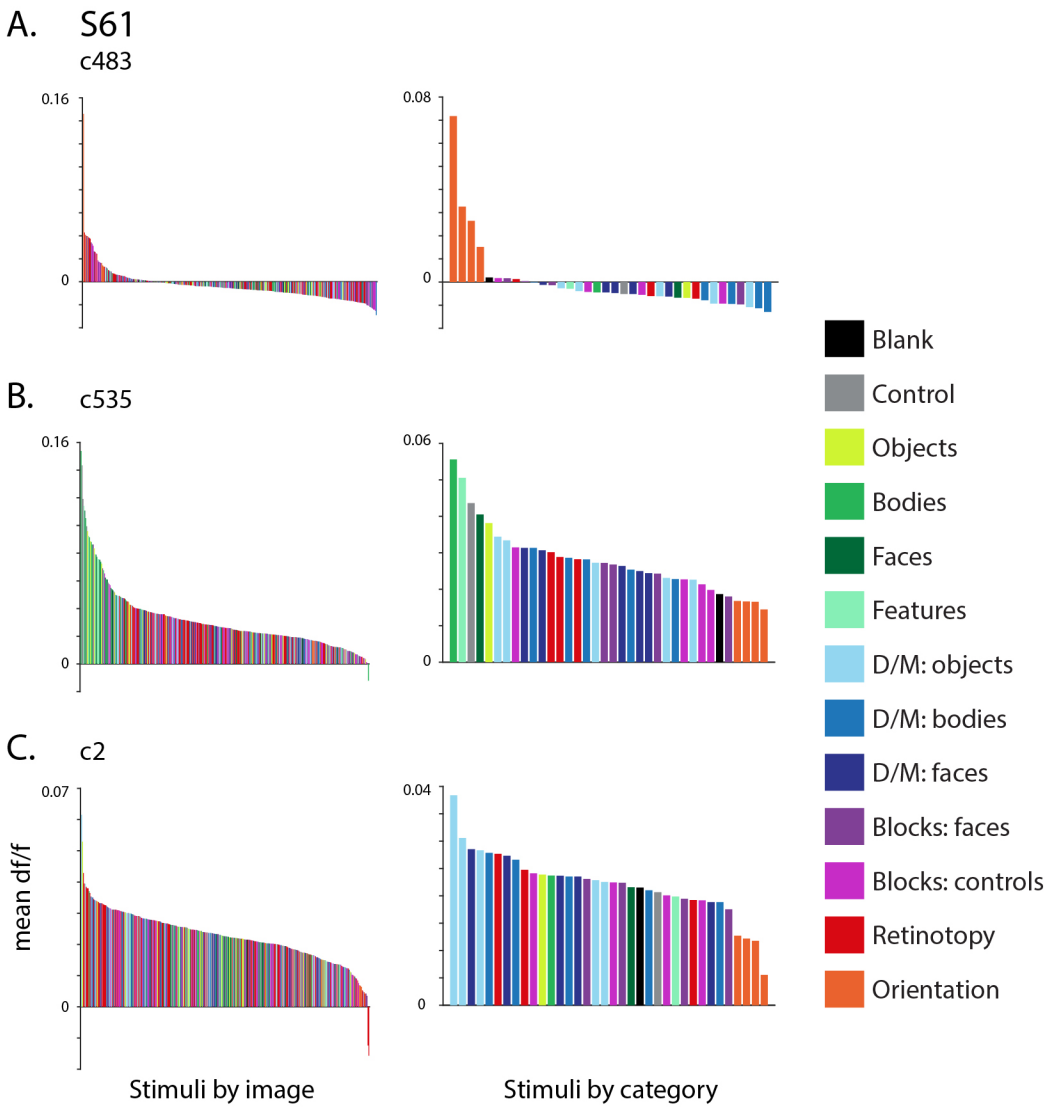

Figure 2.6 Rank ordering of mean component responses to stimuli
All data in this graph are from field S61. The individual components from which these data are taken are indicated by a "cNumber." A. Mean response to each individual stimulus presentation, ranked by mean (right). Individual stimuli can be assigned to categories. Mean response to each individual category, ranked by mean (left). B, C, are the same as A for additional components. D/M, Diffeomorph, metamer.

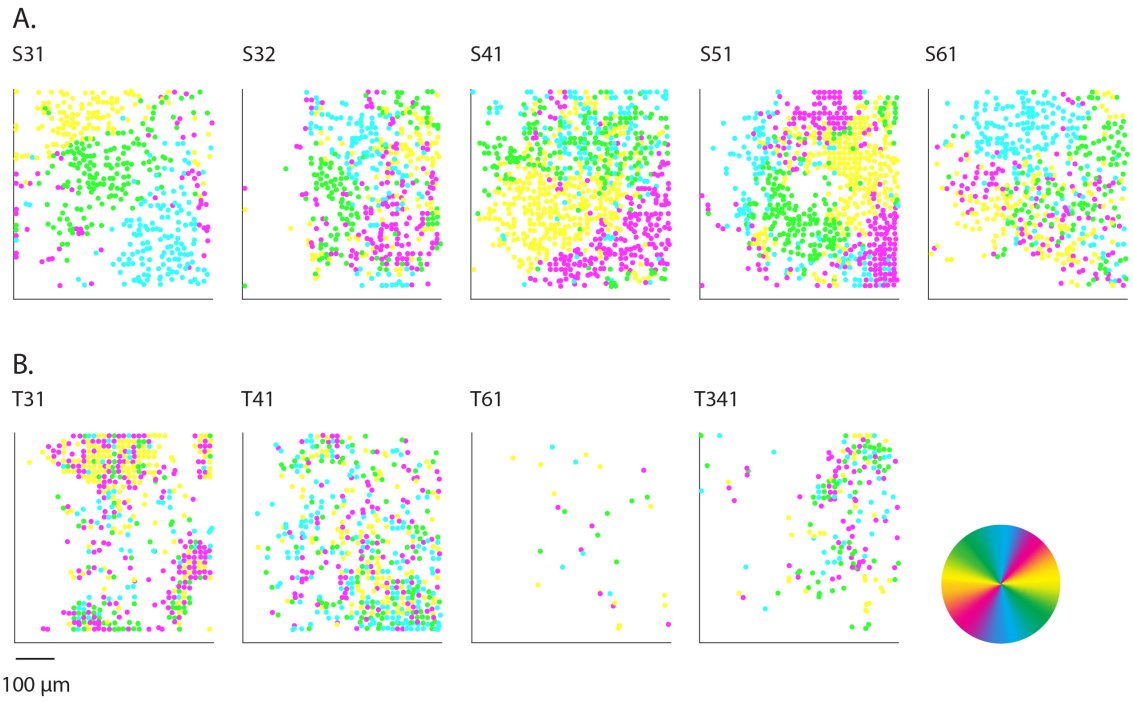

Figure 2.7 Orientation tuning maps across fields
A. Orientation tuning within all 5 fields in animal S. The center of each point is the centroid of a component found in the field B. Same as A, but for animal T. All orientations are indicated by the color wheel.

Examining the spatial structure of the field maps, it appeared that the components that preferred orientations clustered together in a way that did not directly overlap with any particular orientation when compared to Fig 2.7. Additionally, there was no significant difference between the proportion of components that were significantly responsive to faces, objects, or bodies. Rather than this area being specific to one particular type of stimulus category, such as faces, we subsequently asked whether the underlying organization was structured by a whether or not the stimuli were naturalistic images or not. We thus grouped together all faces, objects, bodies, and features into a single group, FOBF.

We ran another comparison in which the categories were structured to include a range of content from unnatural stimuli (Orientation, Retinotopy, Blocks) to naturalistic stimuli (Diffeomorphs, Metamers, FOBF). In this comparison, interestingly, there was a clear clustering in the spatial maps in which orientation components still clustered separately from components that preferred naturalistic stimuli (Fig 2.8.B). Surprisingly, when we examined the field maps of animal T, this comparison revealed a field wide significant preference for naturalistic stimuli.

We then looked at the proportion of significant components per category across all of the fields. This revealed that there are two distinct groups that appear: components that preferred orientations and components that preferred naturalistic stimuli. As the level of naturalistic content decreased, so did the proportion of cells responsive to that category until reaching the orientation stimuli in which case the proportion again then increased. Further, if the two proportions of naturalistic stimuli preferring components and orientation stimuli preferring components existed in approximately equal proportions in a single field, they clustered in separate groups.

If this area indeed responded to naturalistic stimuli in a clustered fashion, we wanted to determine whether or not there were an underlying perceptual or statistical content features that drove activity in these components. If there was a significant, separable feature amongst naturalistic stimuli, then perhaps V2 and "O" would respond to that relevant subset of stimuli most strongly, rather than the naturalistic stimuli as a whole. To do this, we split the naturalistic stimuli into groups dependent on their perceptual content, statistical permutation content, or identity (Fig 2.9). Across all comparisons, we found no significant differences. This suggested that rather than a single feature of naturalistic stimuli driving the responses, it was the composite, naturalistic image.

Tables 2.1-2.5 contain the proportion of significant cells per category per field for all categories tested. The data from these tables allow a more granular view of what is happening in individual fields in addition to the overall proportion.

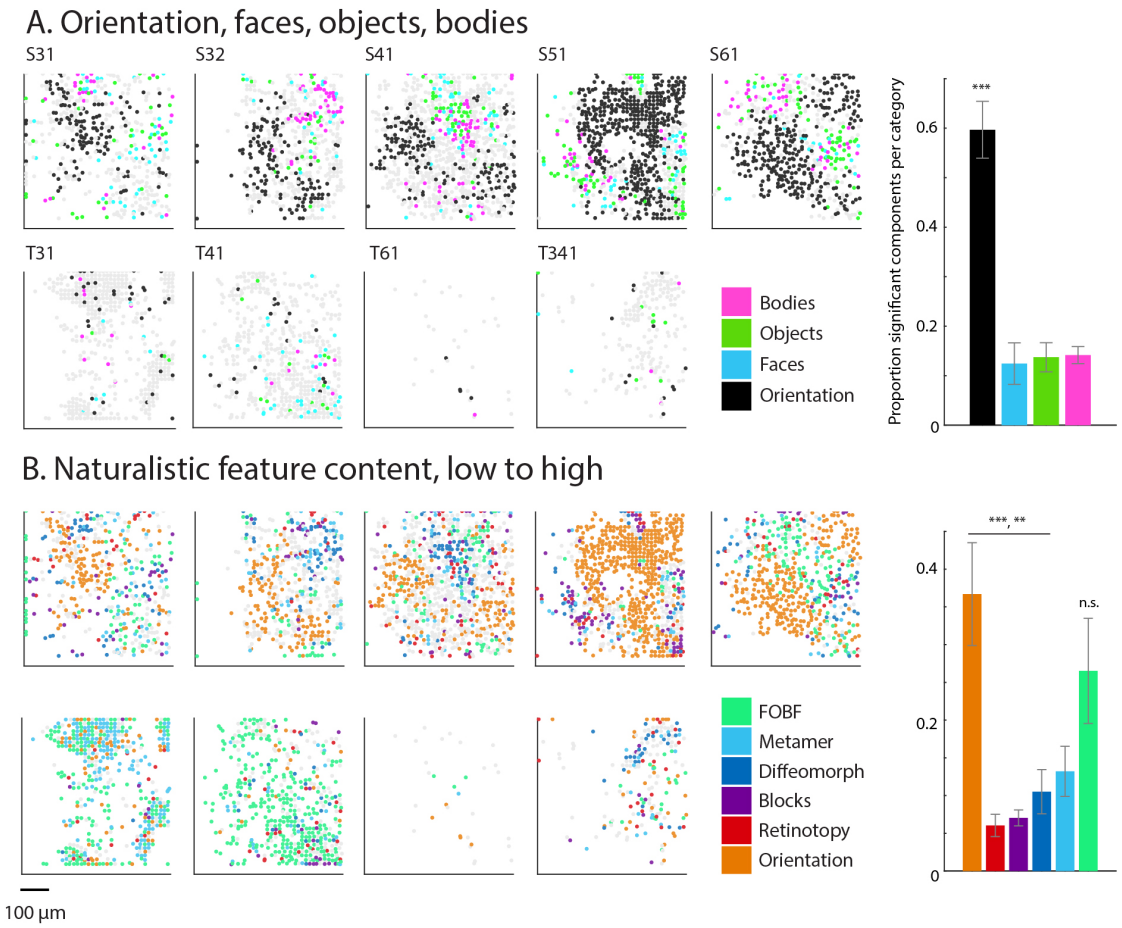

Figure 2.8 Spatial maps reveal components significant for naturalistic stimuli
A. Field maps color coded to reveal components that significantly respond to Orientation, Faces, Objects, or Bodies. The colored box provides the color key for the components as well as the bar graph on the right. The averaged proportions of significant cells per category across all fields are plotted. B. Same as A, however for Orientation, Retinotopy, Blocks, Diffeomorphs, Metamers, or FOBF (faces, objects, bodies, features).

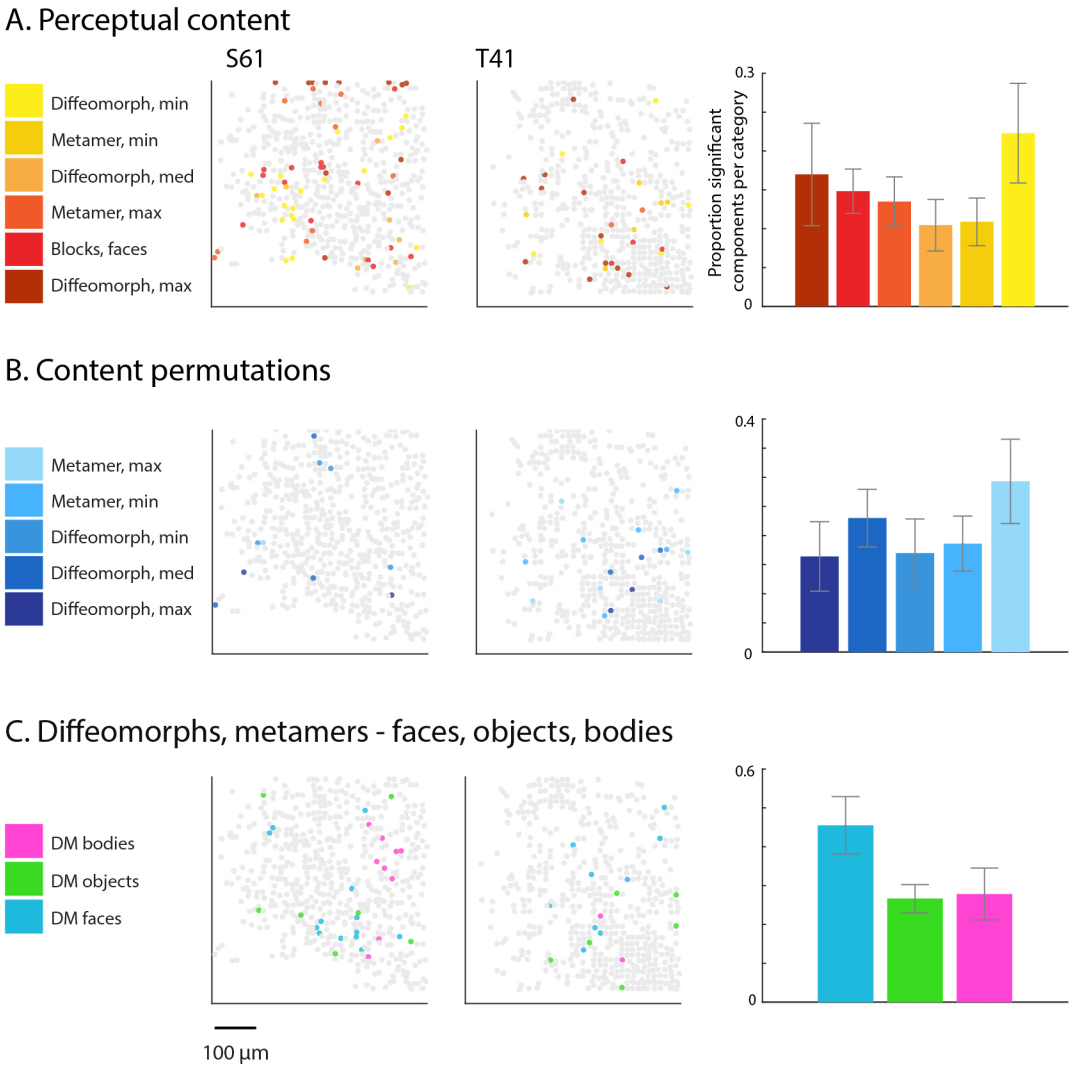

Figure 2.9 No separable features inherent to naturalistic stimuli drive response In this figure, only two exemplar fields are shown across all comparisons, S61 and T41. A. Field maps color coded to reveal components that significantly respond to different gradations of Perceptual Content. The colored box provides the color key for the components as well as the bar graph on the right. The averaged proportions of significant cells per category across all fields are plotted. B., C. Same as A, however for Content permutations and Diffeomorphs, Metamers categories, respectively. DM, Diffeomorph, metamer.

Table 2.1 Proportion significant components: Orientation, Faces, Objects, Bodies

Recording sites	Total cells	Nonsignificant	Significant	Orientation	Faces	Objects	Bodies
S31	486	243	243	125 (51.4%)	44 (18.1%)	44 (18.1%)	30 (12.3%)
S32	539	319	220	130 (59.1%)	21 (9.5%)	21 (9.5%)	48 (21.8%)
S41	918	569	349	203 (58.2%)	40 (11.5%)	47 (13.5%)	59 (16.9%)
S51	818	202	616	455 (73.9%)	40 (6.5%)	90 (14.6%)	31 (5.0%)
S61	597	167	430	311 (72.3%)	20 (4.7%)	58 (13.5%)	41 (9.5%)
T31	531	466	65	45 (69.2%)	7 (10.8%)	3 (4.6%)	10 (15.4%)
T41	542	468	74	17 (23.0%)	32 (43.2%)	14 (18.9%)	11 (14.9%)
T61	36	31	5	4 (80.0%)	0 (0.0%)	0 (0.0%)	1 (20.0%)
T341	204	178	26	13 (50.0%)	2 (7.7%)	8 (30.8%)	3 (11.5%)
TOTAL	4671	2643	2028	1303 (64.3%)	206 (10.2%)	285 (14.1%)	234 (11.5%)
Orientation, faces, objects, bodies							

In each category comparison, components are tested for significance with the Kruskal-Wallis one-way analysis of variance (ANOVA) with a Dunn's post test for multicomparison correction with a significance cut-off of $p = 0.05$. The total number of cells or components are broken into nonsignificant and significant groups. Then, the number of components that meet significance within each category are denoted in each column both as a total number and as a percentage of the number of significant components found in that field.

Table 2.2 Proportion significant components: Naturalistic feature content

Recording sites	Total cells	Nonsignificant	Significant	Orientation	Retinotopy	Blocks	Diffeomorph	Metamer	Faces, objects, bodies, and features
S31	486	146	340	120 (35.3%)	26 (7.6%)	29 (8.5%)	55 (16.2%)	44 (12.9%)	66 (19.4%)
S32	539	235	304	117 (38.5%)	9 (3.0%)	21 (6.9%)	68 (22.4%)	47 (15.5%)	42 (13.8%)
S41	918	457	461	198 (43.0%)	47 (10.2%)	38 (8.2%)	61 (13.2%)	48 (10.4%)	69 (15.0%)
S51	818	154	664	459 (69.1%)	30 (4.5%)	81 (12.2%)	39 (5.9%)	34 (5.1%)	21 (3.2%)
S61	597	68	529	284 (53.7%)	28 (5.3%)	22 (4.2%)	44 (8.3%)	28 (5.3%)	123 (23.3%)
T31	531	88	443	65 (14.7%)	13 (2.9%)	7 (1.6%)	2 (0.5%)	167 (37.7%)	189 (42.7%)
T41	542	125	417	15 (3.6%)	24 (5.8%)	21 (5.0%)	20 (4.8%)	29 (7.0%)	308 (73.9%)
T61	36	26	10	5 (50.0%)	0 (0.0%)	1 (10.0%)	0 (0.0%)	1 (10.0%)	3 (30.0%)
T341	204	84	120	27 (22.5%)	18 (15.0%)	8 (6.7%)	28 (23.3%)	18 (15.0%)	21 (17.5%)
TOTAL	4671	1383	3288	1290 (39.2%)	195 (5.9%)	228 (6.9%)	317 (9.6%)	416 (12.7%)	842 (25.6%)
Naturalistic feature content low level to high level									

Table 2.3 Proportion significant components: Perceptual content

Recording sites	Total cells	Nonsignificant	Significant	Diffeomorph, maximum permutation	Blocks, faces	Metamer, maximum permutation	Diffeomorph, medium permutation	Metamer, minimum permutation	Diffeomorph, minimum permutation
S31	486	453	33	6 (18.2%)	5 (15.2%)	6 (18.2%)	4 (12.1%)	4 (12.1%)	8 (24.2%)
S32	539	497	42	1 (2.4%)	7 (16.7%)	9 (21.4%)	13 (31.0%)	8 (19.0%)	4 (9.5%)
S41	918	880	38	0 (0.0%)	9 (23.7%)	5 (13.2%)	7 (18.4%)	9 (23.7%)	8 (21.1%)
S51	818	768	50	26 (52.0%)	8 (16.0%)	6 (12.0%)	2 (4.0%)	0 (0.0%)	8 (16.0%)
S61	597	527	70	12 (17.1%)	14 (20.0%)	12 (17.1%)	8 (11.4%)	2 (2.9%)	22 (31.4%)
T31	531	432	99	3 (3.0%)	4 (4.0%)	3 (3.0%)	4 (4.0%)	18 (18.2%)	67 (67.7%)
T41	542	508	34	16 (47.1%)	4 (11.8%)	2 (5.9%)	0 (0.0%)	6 (17.6%)	6 (17.6%)
T61	36	36	0	0 (0.0%)	0 (0.0%)	0 (0.0%)	0 (0.0%)	0 (0.0%)	0 (0.0%)
T341	204	181	23	3 (13.0%)	6 (26.1%)	7 (30.4%)	3 (13.0%)	1 (4.3%)	3 (13.0%)
TOTAL	4671	4282	389	67 (17.2%)	57 (14.7%)	50 (12.9%)	41 (10.5%)	48 (12.3%)	126 (32.4%)
	Perceptual content								
	not perceptable to readily perceptible								

Table 2.4 Proportion significant components: Content permutations

Recording sites	Total cells	Nonsignificant	Significant	Diffeomorph, maximum permutation	Diffeomorph, medium permutation	Diffeomorph, minimum permutation	Metamer, minimum permutation	Metamer, maximum permutation
S31	486	468	18	2 (11.1%)	7 (38.9%)	1 (5.6%)	4 (22.2%)	4 (22.2%)
S32	539	518	21	3 (14.3%)	4 (19.0%)	4 (19.0%)	4 (19.0%)	6 (28.6%)
S41	918	877	41	10 (24.4%)	8 (19.5%)	5 (12.2%)	10 (24.4%)	8 (19.5%)
S51	818	805	13	1 (7.7%)	1 (7.7%)	3 (23.1%)	1 (7.7%)	7 (53.8%)
S61	597	584	13	2 (15.4%)	4 (30.8%)	5 (38.5%)	5 (38.5%)	2 (15.4%)
T31	531	487	44	1 (2.3%)	1 (2.3%)	2 (4.5%)	8 (18.2%)	32 (72.7%)
T41	542	526	16	2 (12.5%)	3 (18.8%)	0 (0.0%)	6 (37.5%)	5 (31.3%)
T61	36	34	2	0 (0.0%)	1 (50.0%)	1 (50.0%)	0 (0.0%)	0 (0.0%)
T341	204	199	5	3 (60.0%)	1 (20.0%)	0 (0.0%)	0 (0.0%)	1 (20.0%)
TOTAL	4671	4498	173	24 (13.9%)	30 (17.3%)	21 (12.1%)	38 (22.0%)	65 (37.6%)
Content permutations diffeomorphs, metamers								

Table 2.5 Proportion significant components: Diffeomorphs, metamers – faces, objects, bodies

Recording sites	Total cells	Nonsignificant	Significant	Diffeomorph & metamer, faces	Diffeomorph & metamer, objects	Diffeomorph & metamer, bodies
S31	486	464	22	14 (63.6%)	5 (22.7%)	3 (13.6%)
S32	539	506	33	7 (21.2%)	15 (45.5%)	11 (33.3%)
S41	918	874	44	21 (47.7%)	4 (9.1%)	19 (43.2%)
S51	818	775	43	21 (48.8%)	7 (16.3%)	15 (34.9%)
S61	597	568	29	13 (44.8%)	7 (24.1%)	9 (31.0%)
T31	531	522	9	6 (66.7%)	2 (22.2%)	1 (11.1%)
T41	542	524	18	9 (50.0%)	6 (33.3%)	3 (16.7%)
T61	36	33	3	2 (66.7%)	1 (33.3%)	0 (0.0%)
T341	204	201	3	0 (0.0%)	1 (33.3%)	2 (66.7%)
TOTAL	4671	4467	204	93 (45.6%)	48 (23.5%)	63 (30.9%)
Diffeomorphs, metamers of faces, objects, bodies						

2.6 Establishing a method for identifying cell-type specific organization

*Due to temporary university closures, this portion of the project has yet to come to completion. Upon reopening of the university, the brains are ready to undergo the first round of imaging as described in Fig 2.13.

We next wanted to determine whether or not there were cell-type specific contributions to these maps. Perhaps specific cell types confer category selectivity or mediate responses within a region. This may exist both at the single cell level or at the population level wherein the distribution of different cell types creates the boundaries between different areas within the functional maps. In order to test these hypotheses, we created a novel volumetric immunohistochemistry and coregistration pipeline.

Although there is a long history of clearing tissues with numerous different approaches including solvent based, immersion, hyper-hydration, and hydrogel embedding, among others, (Richardson and Lichtman 2015) there continue to be optimization points in order to be able to fully apply the great potential of clearing to functional studies. Here, we elected to forego traditional histological as it would be impossible to capture all of our fields in slices or flat maps. Each field was recorded at a slightly different angle and as such, we would sacrifice neighboring planes of imaging to be able to functionally register even one. Further, given our interest in determining the cell-type identities underlying the reports of increased suppressive tuning, we aimed to be able to conduct iterative staining sequences in order to capture as many inhibitory cell types as possible. Working with the Wu Laboratory at Mount Sinai, we adapted protocols of theirs based on organic solvents (Chi et al. 2018; Renier et al. 2014) to instead be compatible with all aqueous reagents. This transition to aqueous reagents allowed us to be able to delipidate the tissue, perform antibody staining, match the refractive index for imaging, and then wash back to being able to further stain the tissue. When working with organic solvent clearing protocols, once the tissue has undergone refractive index matching, it is not possible to return the tissue to a state that allows for further antigen retrieval. This aqueous clearing method is currently in preparation as its own work from the Wu lab, but here, we use a variant termed MarmoClear (Fig 2.10). As can be seen from the comparison of iDisco, an organic solvent method, to MarmoClear, the aqueous solvent method, in mouse brains (Fig 2.10.A), both clearing methods achieved approximately the same level of transparency in terms of approximate amount of light transmitted; however, the MarmoClear protocol was the only treatment that significantly reduced the amount of scattered light. This is likely due to a Refractive Index mismatch between DBE, the clearing solution for iDisco, and the remaining proteins in the tissue sample or incomplete delipidation. The latter is of particular concern when working with denser tissue samples such as non-human primate cortical regions.

Figure 2.10 Transmittance and scattering properties of MarmoClear
A. Initial comparisons were done on mouse samples. ii, Mouse brains imaged with bright field illumination. Untreated (left, black), iDisco cleared (middle, dark gray), MarmoClear cleared (right, light gray). ii. Transmittance approximation values as a proportion of sample/background. iii. Mouse brains imaged with dark field illumination. Untreated (left, black), iDisco cleared (middle, dark gray), MarmoClear cleared (right, light gray). iv. Scattered light approximation as a difference in (sample – background)/background. B. Comparision of untreated marmoset sample to MarmoCleared brain sample. i. Marmoset brain areas imaged with bright field illumination. Untreated (left, black), MarmoClear cleared (right, light gray). ii. Transmittance approximation values as a proportion of sample/background. iii. Marmoset brain areas imaged with dark field illumination. iv. Scattered light approximation as a difference in (sample – background)/background. C. Rat (left) and macaque (right) brains cleared with MarmoClear.

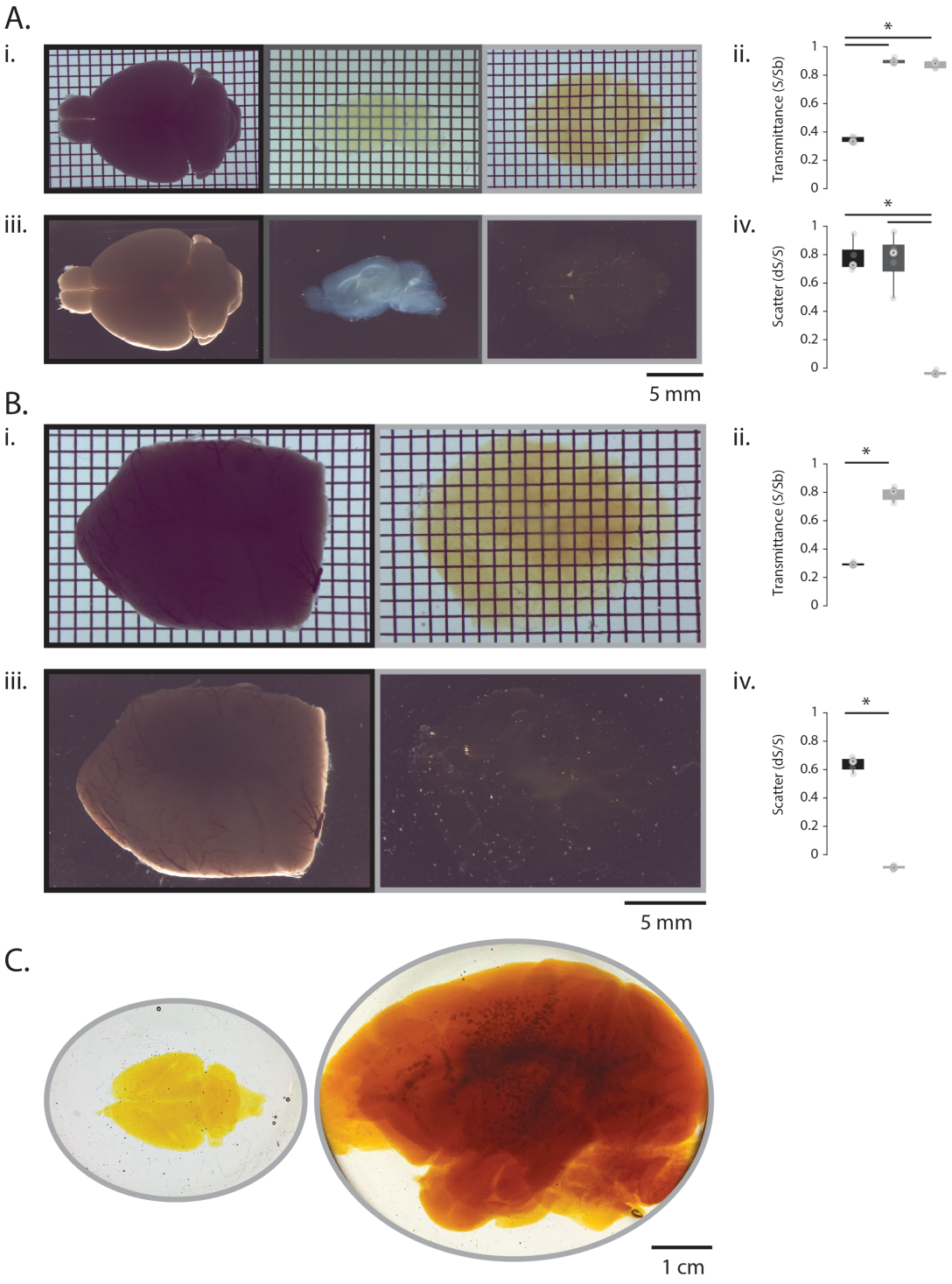
A.
i.
ii.
Transmittance (S/Sb)
iii.
iv.
Scatter (dS/S)
5 mm
B.
i.
ii.
Transmittance (S/Sb)
iii.
iv.
Scatter (dS/S)
5 mm
C.
1 cm

We then confirmed that MarmoClear was compatible with marmoset tissue. It attained the same levels of transparency and reduction in scattered light as the mouse samples (Fig 2.10.B). We further showed that the approach was neither size nor diffusion limited since it was possible to clear whole rat brains and macaque brains (Fig 2.10.C).

We then proceeded to screen a large battery of antibodies to find those compatible with both the clearing process and the marmoset tissue (the full list can be found in Table 2.6 in Section 2.8.6). From this screen, we selected those that specifically targeted markers of interest and rank-ordered them in terms of strength of signal (Fig 2.11). We ensured to probe a wide variety of antibody hosts such that it would be most easily possible to multiplex staining options amongst the channels.

Following the selection of the eight best antibodies, we arranged them into a sequence such that it required three rounds of staining across three imaging channels to reveal the staining patterns of all 8 markers (Fig 2.12). We termed each set of antibodies in an imaging channel a single lane. We ordered the antibodies in lanes and rounds so that there was minimal known overlap between any of the targets, the weaker antibodies were stained first, and targets of highest priority were stained in the first two rounds. For this test, we only had access to 488, 568, and 647 imaging channels; however, due to the presence of the vascular cast in the 488 channel, this lane will be shifted to 790 for the final experiment. Finally, in the last round, one lane also had YOSeta-1, a pan nuclear marker to serve as anatomical reference. Within this arrangement, we were able to distinguish the following inhibitory cell types: Calretinin, Calbindin, nNOS, NPY, and Parvalbumin. Additional markers gave us indications of the presence of astrocytes, and the approximate identity of excitatory neurons through the process of elimination by identifying those neurons labeled with NeuN but not labeled with any additional inhibitory markers. Fig 2.12 reveals that each round captured a unique population of identified cells as shown in each column.

This staining in triplicate forms the order in which the cleared marmoset brains that have been functionally imaged will undergo staining and imaging. Upon each round of imaging, the data set is coregistered to the functional two-photon microscopy datasets in Fig 2.4.

Figure 2.11 Successful antibody hits utilizing MarmoClear and marmoset tissue

All images are taken at the same exposure with no brightness correction so that direct comparisons between slides can be made. The left column is the negative control and only the appropriate secondary. The columns on the right are antibodies in order of increasing signal. Each row contains antibodies from a different host. The antibody target is written in the lower left corner of each panel. A. Wide view that shows the laminar distribution of the labeled cell bodies. B. Zoomed in view by an additional 3X showing cellular resolution of antibody markers.

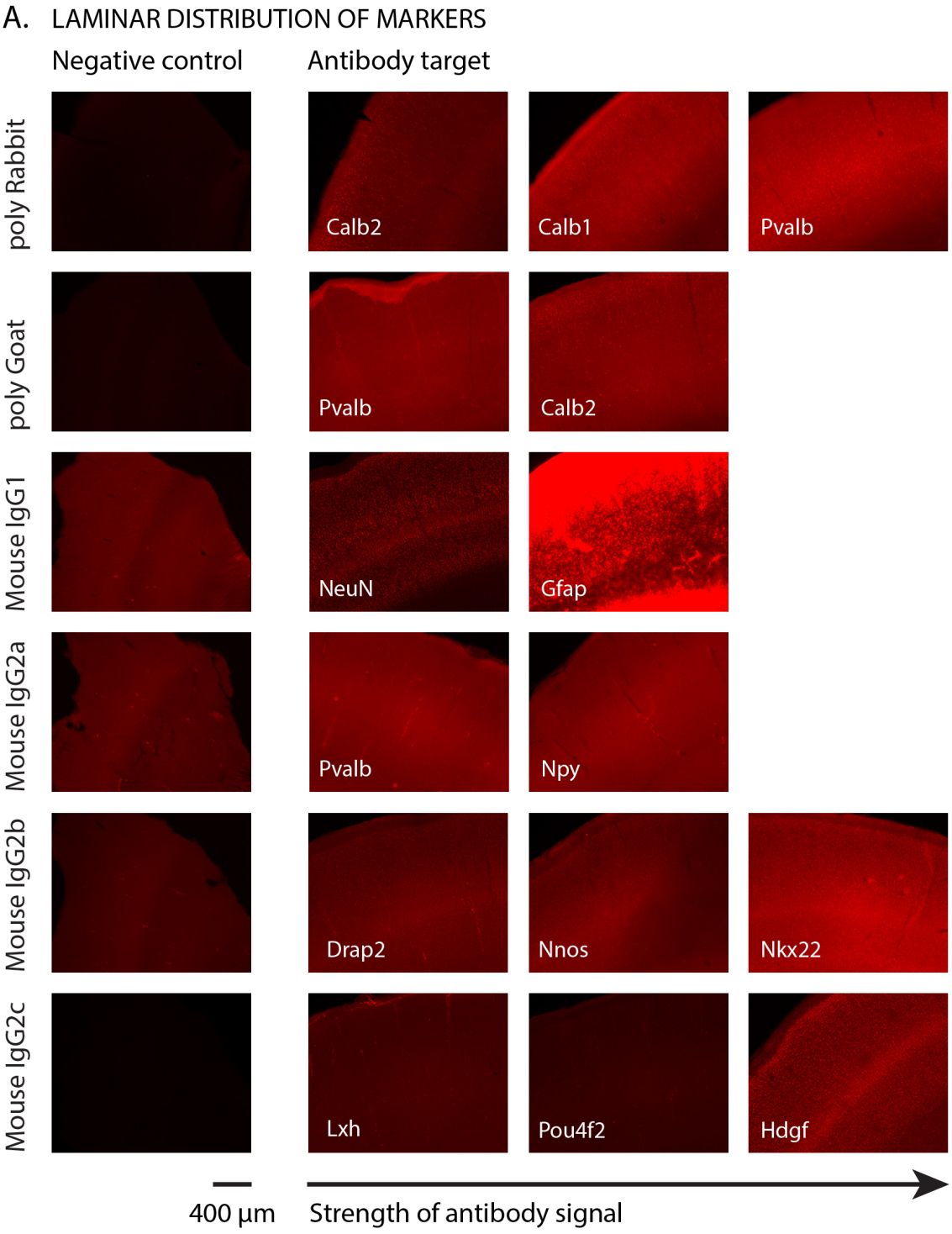
A. LAMINAR DISTRIBUTION OF MARKERS
Negative control
Antibody target
poly Rabbit
Calb2
Calb1
Pvalb
poly Goat
Pvalb
Calb2
Mouse IgG1
NeuN
Gfap
Mouse IgG2a
Pvalb
Npy
Mouse IgG2b
Drap2
Nnos
Nkx22
Mouse IgG2c
Lxh
Pou4f2
Hdgf
400 µm
Strength of antibody signal

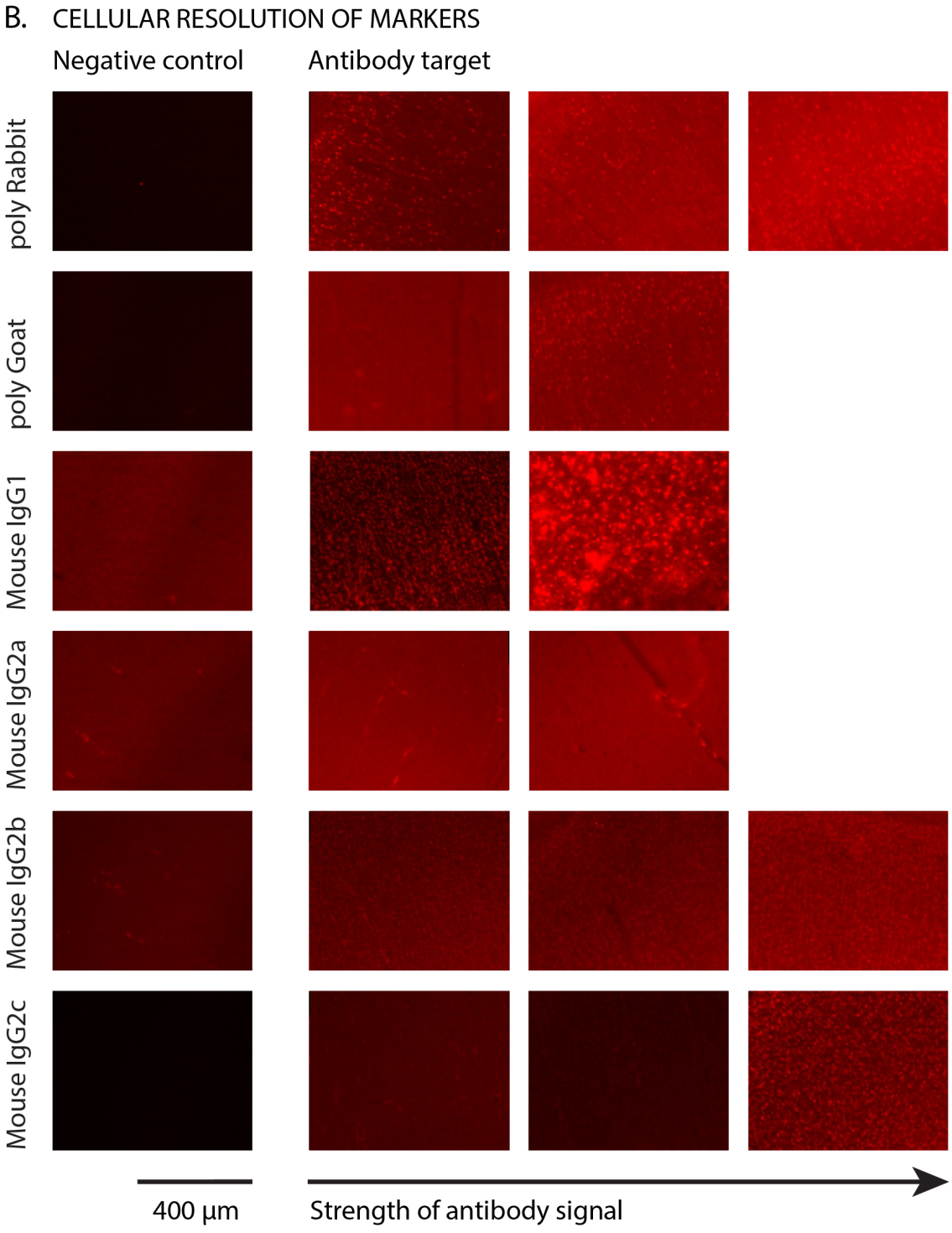
B.
CELLULAR RESOLUTION OF MARKERS
Negative control
Antibody target
poly Rabbit
poly Goat
Mouse IgG1
Mouse IgG2a
Mouse IgG2b
Mouse IgG2c
400 µm
Strength of antibody signal

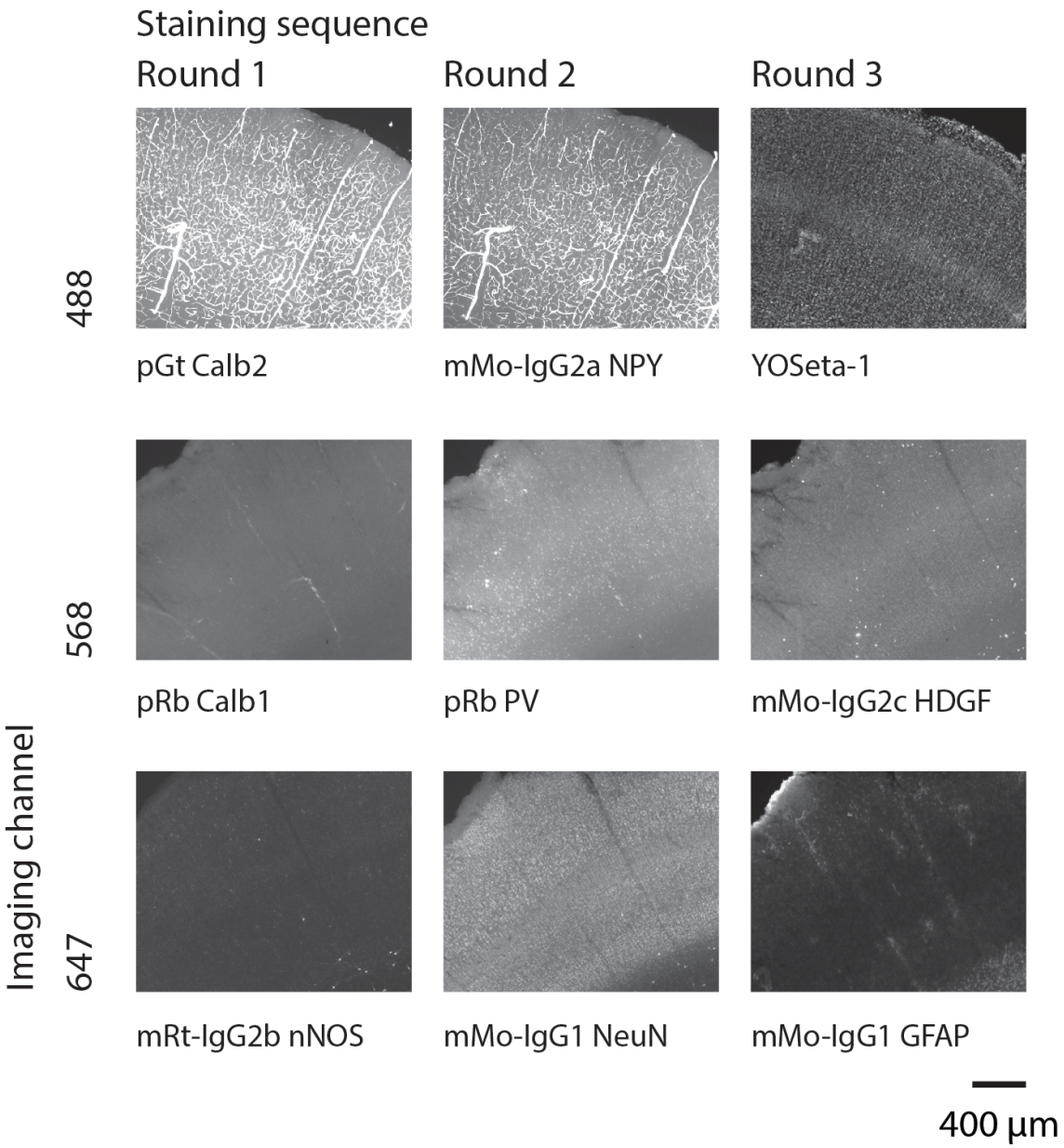

Figure 2.12 Iterative rounds of staining
All images are taken at the same exposure with no brightness correction so that direct comparisons between slides can be made. Each row contains a lane of antibody targets and was imaged in its respective channel (488, top; 568, middle; 647, bottom). Iterative rounds of staining with Rounds 1, 2, and 3.

The process of coregistration depends on the interaction of three vascular maps (Fig 2.13). During the session of two-photon functional imaging, the animal was injected with an IV solution of high molecular weight Texas Red conjugated to a dextran (0.1mL, 8 mg/mL in isotonic saline IV, ThermoFisher, MA, USA, D1830). Immediately upon injecting, an anatomical scan was acquired to reveal the vasculature through the field of interest. It was then possible to match this to a wide field image of the entire window taken with green illumination through the use of reference markers placed at the intersections of the vessels (Fig 2.13.A). This established a global positioning of each field within the larger window. Upon finishing all functional experiments, we created an FITC-albumin conjugated vascular cast by transcardially perfusing the animal with a gelatin solution as described in the Methods section (Fig 2.13.B). The brain was then sectioned into 1cm^3 chunks and cleared using MarmoClear (Fig 2.13.C). The vascular cast remains intact throughout the clearing process as is shown in the left panel of Fig 2.13.D This then allows the identification of the key markers of registration established in Fig 2.13.A to be discovered again and matched back to the two-photon data.

Upon acquiring the volumetric immunohistochemical data, we will have a complete representation of the functional architecture of this area from the level of wide field imaging down to the component cell types providing a holistic view of an area, that while it may not be a face patch, is at a critical juncture of transforming sensory input into social perception.

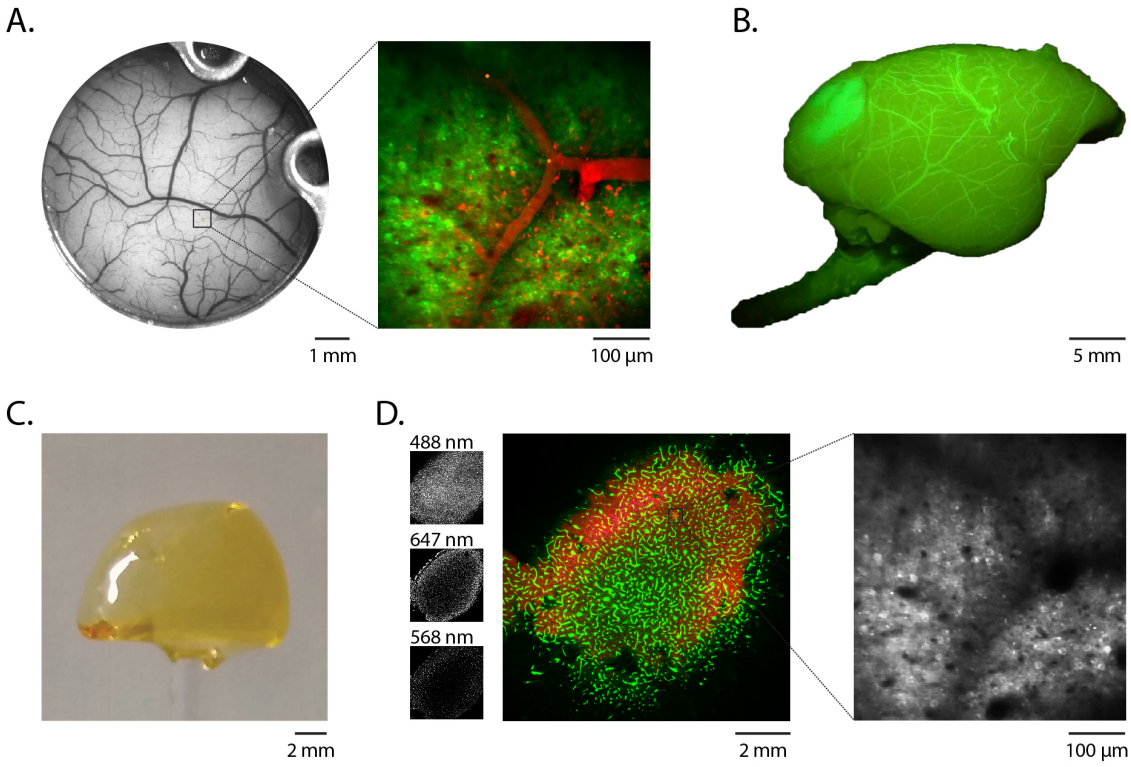

Figure 2.13 Schema for coregistration of functionally imaged tissue to volumetric immunohistochemistry
A. Wide field image of entire imaging window taken with green illumination. Inset, two-photon imaging field of view with Texas-Red Dextran vascular fill. B. *ex vivo* brain with vascular cast illuminated with blue illumination. C. Cleared occipital cortex from sample in B. D. Example data of the process of coregistering the light sheet imaging data to the two-photon imaging data through the use of the vascular cast.

2.7 Methods

2.7.1 Animals

All animals were in normal health and were group housed with other conspecifics at the facility. All procedures were approved by The Rockefeller University Animal Care and Use Committee and were performed in accordance with the National Institute of Health guidelines for care and use of laboratory animals. There are four animals included in this study with two for imaging and two for histology. There were 2 females and 2 males all adults between the ages of 2.5 – 6 years old.

2.7.2 Wide field analysis

Wide field imaging maps shown in Fig 2.3 were calculated as the widefield normalized change in florescence (df/f) by finding the mean fluorescence for 2 s after the stimulus turned on, subtracting 0.5 s averaged fluorescence pre-stimulus and then dividing this resultant value by the mean pre-stimulus fluorescence. This df/f map is calculated per stimulus presentation. For the orientation maps, they are displayed as the orientation map with a background cocktail subtracted. The orientation map is the average of all maps corresponding to a particular orientation and the cocktail is the average of the response to all stimuli. The final maps are overlaid on the left of the figure and the individual maps are displayed on the right of the figure. For the face, object, body maps, they are displayed as the contrast of the category stimulus minus the average of the two other stimuli. The category map is created by averaging all maps for that particular category of stimuli. From this we subtract the average map from the other stimulus categories. Again, the final maps are overlaid on the left of the figure and the individual maps are displayed on the right of the figure.

2.7.3 Two photon analysis, preprocessing

All two photon data were acquired at 40Hz and saved as TMDS indexed LabView (National Instruments, TX, USA) files that were subsequently converted to 16 bit tiff-stacks using a software package, LotosScan (ABORO-tech, Beijing, China). These images were then uniformly cropped to remove the edge protection lacing and lash back section of the images. All data were synchronized with a TTL collected from the presentation screen collected at a sampling rate of 12kHz. This was subsequently transformed into a step function wherein high indicated stimulus on and low, stimulus off. This step function was downsampled to 40Hz with each bin being assigned to a single frame of the two-photon data. Initially, we concatenated about 100 trials of 6 seconds each together to be preprocessed. However, due to the design of the experiment with over 300 individual stimuli, there were many neurons that would not respond in a set block of 100 trials greatly complicating registering the neurons over multiple blocks of data. As a result, we concatenated all 1616 trials per experiment together to make a single data set for preprocessing. All motion correction and fluorescence extraction from the data was done with CaImAn (Giovannucci et al. 2019) in Python (Python Software Foundation, DE, USA). The following parameters were customized for input into the batch processing pipeline in CaImAn and are dependent on the quality of the data and the experimental parameters. They include decay_time = 1.5: typical transient for GCaMP6s; max_shift_um = 12,12: maximum shift in um; min_SNR = 2: signal to

noise ratio for components, rval_thr = 0.85: space correlation threshold, quantileMin = 8: quantile used to estimate the baseline of fluorescence; and frames_window = 250: number of frames for computing running quantile.

The full stack of 1616 trials is approximately 250 Gb, which expands to 500 Gb mapping to memory structures in Python, and finally must be loaded into memory twice throughout the preprocessing pipeline. A minimum of 1 Tb RAM is needed to preprocess the data in this manner. All preprocessing was conducted on the Rockefeller University High Performance Computing cluster, bigmem, with 3 Tb RAM. Motion correction was conducted with piecewise rigid motion correction with a patch size of 500. Components were then identified using a constrained non-negative matrix factorization framework (CNMF) allowing the extraction of overlapping components. Input parameters were selected to bias the components toward cell bodies. We detrend the data to remove any drifting baseline from the photobleaching, calculate change in fluorescence over baseline for each component (df/f) and finally deconvolve the data to its underlying spike rates. The df/f is determined by taking the baseline as calculated as the minimum octile over a period of 250 frames (6.25 s) and subtracting it from the fluorescence at each point in time. This is then divided by the baseline.

In this chapter, we only analyze the df/f signal. All discovered components are then subject to a second filter in which they must meet appropriate size constraints and decay constraints as empirically determined from the data. The centroids of all accepted components are plotted as individual dots in Fig 2.4 for all fields recorded across the two animals.

2.7.4 Two photon analysis, postprocessing

Data are then exported to MATLAB (MathWorks, MA, USA) in which they are preprocessed into data structures compatible with the core lab code base, Phyzzy (https://github.com/freiwaldlab/phyzzy). A branch of this code base has been created for optical imaging data, Opzzy. All code is pushed to GitHub and is available upon request at any time. All analyses use a p-value of 0.05. Error bars are standard error of the mean.

Time based analyses such as the PSTH plots in Fig 2.5 are displayed as the mean activity of the component to all presentations of that particular stimulus. There are between 4-8 repetitions per stimulus which are then grouped together in larger categories as demonstrated by the colored boxes in Fig 2.5.B.

This data is then compressed for further analyses by averaging the mean fluorescence for 0.05 – 2 s after the stimulus turns on and plotting the rank-ordered means as in Fig 2.6. Each row is a representative component. The column on the left is each component's rank-ordered responses to each individual stimulus. The column on the right is each component's rank-ordered responses to categories of stimuli in which all individual stimulus responses are assigned to categories and these responses are then averaged together. These average category responses form the input for the subsequent category analyses.

For the orientation tuning curves in Fig 2.5.A each orientation is plotted as its mean activity with its standard error of the mean. For creating orientation field maps in Fig 2.7, each component is color coded to the peak of its respective tuning curve. In comparing only 8 individual stimuli, this is sufficient to assign peaks in this manner. However, for other categories such as those found in Fig 2.6, due to the many stimuli being averaged per category and calcium imaging providing an inherently noisy signal, wanted to perform statistical analyses between categories based not on their extremely noisy mean activity instead by comparing their rank-order across stimuli categories of interest. These category comparisons are tested for significance with the Kruskal-Wallis one-way analysis of variance (ANOVA) with a Dunn's post test for multicomparison correction also with a significance cut-off of 0.05. Given that we are not certain if each stimulus category has a Gaussian distribution of responses, we elected to use the nonparametric Kruskal-Wallis version of the ANOVA. Each component in Fig 2.8 and 2.9 is color coded to the category for which there is a significantly higher rank-order for its activity compared to other stimuli. If there is no significant difference, the component is shown in light gray.

Bar plots in Fig 2.8 and 2.9 show the proportion of significant components per category. Significance testing between these proportions was done with a two-way t-test and a p value of 0.05. These bar plots show the summary of components across all fields. The individual field proportions are captured for each experiment in Tables 2.1 – 2.6.

2.7.5 Stimuli

For the periodic drifting gratings and retinotopy, we used parameters taken from the literature that were optimized for marmoset vision. Gratings were shown at 1.2 cycles/degree with a frequency of 4 degrees/second (Solomon and Rosa 2014) and displayed at approximately 100% contrast. For the initial orientation tests, gratings were rotated in 45° steps and shown at full field for 2 s with a minimum of a 4 s interstimulus interval (ISI). Often, we increased the ISI to prevent photobleaching and achieved a duty cycle of approximately 66%. For retinotopy experiments, we used orientations only at 90° steps and reduced the stimulus to occupy only 20° of the visual field. We tiled the entire visual field with presentations of these stimuli to confirm placement of the stimuli in retinotopic space. Retinotopy stimuli were also shown for 2 s.

For the objects stimuli set, the fruits and objects were taken from BOSS stimuli packages as well as the Tarr Labs Novel Objects page. These stimulus images were courtesy of Michael J. Tarr, Center for the Neural Basis of Cognition and Department of Psychology, Carnegie Mellon University. All marmoset images were taken of the marmosets in the colony at The Rockefeller University under institutional approval. Images were taken with a Pentax dSLR (6 MP) and a GoPro Hero4 Session (1080p/30fps) that manually tracked the animals inside of the transfer box. Images and frames were extracted and manually cropped for the animal's face, feature, or body in Adobe Illustrator CS6 (Adobe, CA, USA). For all images of marmosets in this stimulus set, we balance gender, familiarity, and display 5 rotational views of both the body and the head.

All images of faces, features, objects, and bodies, were converted to grayscale and normalized both for histogram distribution and rotational average frequency amplitude using the SHINE Toolbox (Willenbockel et al. 2010). This rendered all images matched in contrast, luminosity, and approximately equal spatial frequency content as well. This was conducted to control for the low-level features of the stimuli that are known to have specific functional architectures throughout early visual processing areas. By controlling for these features across all stimulus sets, we can be certain that we do not confound our search for functional architecture with one that is related to orientation or color, for example. This is a common technique used in studies of early primate vision, but to our knowledge, this is the first time stimuli of this variety are being studied in the marmoset. All images were placed on a gray background that matched the rest of the stimulus screen.

The normalized images also formed the input images for creating the metamers and diffeomorph images, but these resultant images themselves were then not further normalized so as to not disrupt the image statistics. Metamers of faces, objects, and bodies were created with open source code for creating these images (Freeman and Simoncelli 2011). Values for V2 receptive field size were taken from previously published literature (Rosa, Fritsches, and Elston 1997). We created two metamers per input image – the "maximally permuted" from input image and the "minimally permuted" from input image. From human report, who share approximately a similar value for V2 receptive field size, a metamer of 50 iterations creates an image that when looking at the fixation point, is indistinguishable from the original image (Freeman and Simoncelli 2011). Therefore, we used this as the bar for the minimally permuted image. In creating the metamer sets, we noted that iteration 3 was the threshold between being ambiguous in content and being the correct identity, but distorted. We therefore used iteration 3 as the bar for creating the maximally permuted images.

Diffeomorphs of images were generated from open source code (Stojanoski and Cusack 2014). The paper includes data gathered from a psychophysics experiment done with Amazon's mechanical turk to determine the degree of warping done on each class of stimuli at which perception of the stimulus is categorized into four groups with perceptual recognizability rated from 1-4: 1 (no, not at all), 2 (I'm not sure, but I can take a guess), 3 (I can see it fairly well), and 4 (I know exactly what it is). They do this for separate categories of images to account for the persistence phenomenon of faces, such as seeing a face in a piece of toast. We then take the degree of warping to achieve each level of recognizability and apply these warps to each of our faces, objects, and bodies. We use the warping necessary to achieve an unrecognizable image as our set of "maximal permutation," the warping necessary to achieve a fairly well seen image as our set of "medium permutation," and finally, the level of warping to achieve an exactly known image as our set of "minimal permutation." The warps necessary to achieve these levels for each category are as follows: faces (35, 10, 1), bodies (17, 5, 1), and fruits/objects (15, 3, 1).

Marmoset face blocks were constructed by manually fitting black and white rectangles in an orientation that best matches the color inversion elements of

a marmoset face from 5 different rotations (L90, L45, Center0, R45, L90). Each image then has its component rectangles rearranged such that any percept of a face is abolished while maintaining the original orientation of each component rectangle. This is to serve as a control for face vs nonface stimuli. Finally, during the experiment, each constructed image is then orientated about the image's center in 45° steps such that it is presented in 8 distinct orientations. These orientations match the orientation angles of the periodic gratings shown in other experiments.

All faces, features, objects, bodies, and controls for image statistics and perception are shown for 0.5 s with again at least a 4 second ISI.

All experiments are conducted in a block style experiment in the following order: orientation, FOBF (faces, objects, bodies, features), blocks, DM (diffeomorphs, metamers), and retinotopy. Within each experiment the order of each individual stimulus presentation is randomized and repeated between 4 – 8 times.

2.7.6 Two-photon microscopy recording

We custom designed and built a microscope (Fig 2.14) with the help of collaborators Dr. Arthur Konnerth at the Technical University of Munich and Dr. Hongbo Jia at Suzhou Institute of Biomedical Engineering and Technology. We opted to use a Mai Tai Deep See tunable laser, tunable from 690 nm – 1040 nm, with an average power of 2.4W (Spectra-Physics, CA, USA). We coupled this with resonant-galvanometer scanning mirrors with a fixed x-scan rate of 12 kHz enabling imaging of 40 Hz at 600 lines and up to 500 Hz at 48 lines. In designing the microscope body, we integrated our system with a microscope body with a rotating nosepiece (Scientifica, United Kingdom). Every aspect of the system is designed to maximize imaging flexibility with the marmoset. Finally, we added two wide field-of-view GaAsP photon multiplier tubes (Hamamatsu, Japan) so that we could image two wavelengths simultaneously. We conduct all two-photon imaging utilizing the 16X Nikon objective (N16XLWD-PF, 0.80 NA, 3.0 mm working distance) and wide field with a 2X ThorLabs objective (TL2x-SAP, 0.10 NA, 56.3 mm working distance). Simply by changing the objective and removing the dichroic mirror, the system is seamlessly interchanged to an wide field and intrinsic optical imaging set up using dual wavelength imaging detected by a 2.3 MP, cMOS camera (FLIR Systems, OR, USA, #BFLY-PGE-23S6M-C). Also integrated into the system are an electroporation amplifier (NPI, Germany) and a patch-clamping amplifier (Heka, Germany). All components are controlled by LotosScan, custom software written in LabView (National Instruments, USA).

We synchronized three system computers such that a there was a single master computer issuing triggers to initiate both stimuli presentation and two-photon microscopy data acquisition. Everything was locked to a single clock on the LotosScan data acquisition computer complete with a photodiode converted TTL trigger to synchronize the exact presentation times of stimuli to the animal. Stimuli presentation was controlled through custom written code adapted from the Calloway Laboratory at the Salk Institute (Juavinett et al. 2017). Stimuli were presented on a gamma corrected ViewPixx LCD Monitor (VPixx Technologies,

QC, Canada). Each trial was 6 seconds with approximately a 66% duty cycle to avoid photobleaching of the tissue.

2.7.7 Surgical approaches

Injections

Marmoset surgeries were performed on adult animals (2.5 years old). Animals were induced with alfaxalone (5-12mg/kg IM) and midazolam (0.05 – 0.7mg/kg IM). They were subsequently intubated and ventilated with oxygen (30-100%). A surgical plane of anesthesia was maintained with a continuous rate infusion consisting of fentanyl (bolus: 5-10 ug/kg, CRI: 10-25 ug/kg/hour) and alfaxalone (bolus: 2-5 mg/kg, CRI: 0.1-0.2 mg/kg/min). Intravenous fluids were also provided at the discretion of veterinary services and the measured glucose level of the animal. Common intravenous fluids administered included isotonic saline, LRS, or normosol-R with 5% dextrose. Six unilateral stereotaxic injections of 500 uL of a 1:1 mixture AAV9-TRE3-GCaMP6s-p2A-GCaMP6s_WPRE (1.71x10^13 gc/ml) and AAV2/3-Thy1-tTA (2.23x10^13gc/mL) were injected at a rate of at 1 nl/s. The injections were made to cover all of V2 that would be accessible in the imaging window and were based on the provided coordinate of -10 mm AP, +6 mm ML, -0.5 mm DV from dura to cover putative face patch "O." These coordinates were provided from personal communication with Dr. Soo Hyun Park in Dr. David Leopold's laboratory and correspond to measures reported in their paper (Hung et al. 2015). Injections were performed with a pulled glass pipette pulled to a tip diameter of 15 um and a 30° bevel (WPI, 504949, 1.14mm, Nanoliter 2010, 504127). Following injection, the pipette was slowly retracted and the craniotomy was filled with Kwik-Sil (WPI, FL, USA) before the surgical site was closed with sutures. All animals received postoperative analgesia consisting of daily meloxicam (0.1-0.2mg/kg PO) and twice per day buprenorphine (0.005 to 0.03 mg/kg IM) for a minimum of 48 hours.

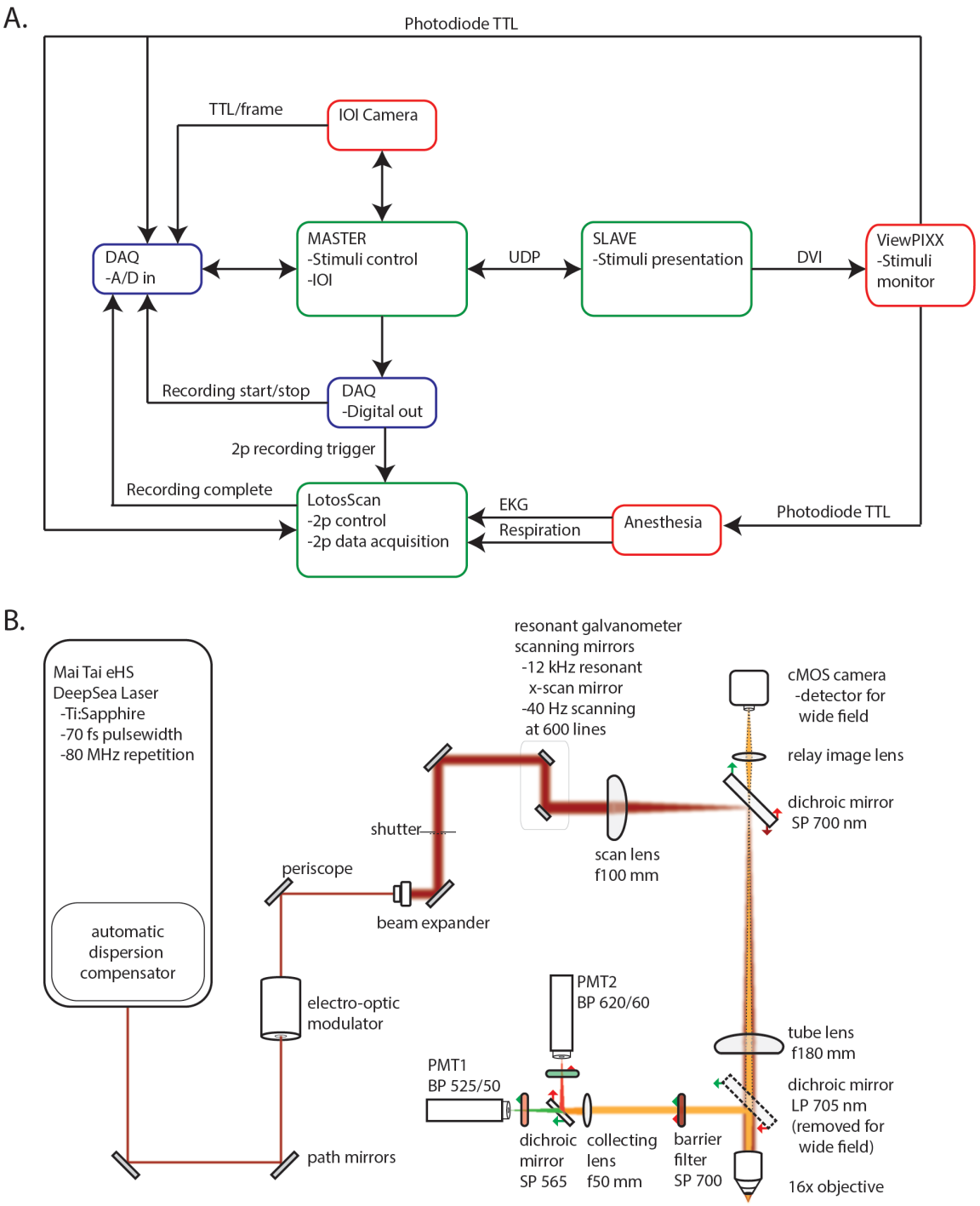

Figure 2.14 Schematic diagram of control system and microscope
A. Line diagram demonstrating the interaction between the control systems and ancillary equipment. All recordings are locked to the common clock on LotosScan, which directly acquires the two-photon imaging data. B. Schematic of the custom two-photon microscope.

Imaging experiments, perfusion, vascular casting

The same surgical approach and anesthetics described for Injection procedures were used in the imaging experiments. Once the skull was exposed, 8 screws with EEG leads were implanted surrounding the headpost implant in order to create a secure point of attachment and monitoring for depth of anesthesia. The temporalis muscles were detached from their origin points and covered with saturated, wet gauze. The craniotomy over the imaging site was made using a dental drill and the durotomy was made using blunted dural scissors and bent 25 G needles. The imaging chamber is implanted with a custom stereotax holder that allows the chamber to be slowly lowered into place as the capillary refill returns in the field of view. The chamber is surrounded by a thin layer of Kwik-Sil (WPI, FL, USA) to prevent communication with the dura and is fixed in place with dental cement. The animal is then paralyzed with cisatracurium (0.09-0.15 mg/kg IV, with a maintenance dose of 0.06-0.12 mg/kg/hour) and transitioned off of alfaxalone and onto nitros oxide:oxygen (70%:30%). Anesthesia depth is monitored by respiratory rate, heart rate, blood pressure, end tidal CO2 (ETCO2), blood oxygen level (Sp02), and core body temperature. EEG and ECG may also be measured if robust signals can be acquired. Heart rate and toe pinch response as well as respiratory rate and palpebral responses are used to assess the depth of anesthesia. Additional isoflurane (0.25-2% IH) or nitrous oxide (1:1 to 7:3) in O2 inhalation anesthesia is administered as needed to maintain a surgical plane of anesthesia. During surgery, the animal is observed continuously with a computer aided system (AD Instruments, Sydney, Australia) recording at a rate of 1kHz and manual records are maintained every 15 minutes. All animals are maintained on intravenous fluids throughout the duration of anesthetized surgical procedures. Additionally, animals receive cefazolin (20-22 mg/kg IV every 4 hours) and dexamethasone (0.5 mg/kg IM PID) intraoperatively.

The animal's eyes were dilated with 1% cyclopentolate, opened with custom 3D printed speculum, fitted with plano 3.8 /5.0 OAD gas permeable contact lenses (Visionary Optics, VA, USA) and then refracted onto a tangent screen utilizing retinoscopic measures. Trial lenses were affixed just in front of the animal's eyes using custom a 3D printed carriage.

Upon conclusion of the imaging experiments, animals were transitioned back to alfaxalone to ensure a deep plane of anesthesia and were humanely euthanized with an injection of sodium pentobarbital (15 mg/kg IV). Subsequent to euthanasia, a cardiac perfusion is performed first with 200 mL of 37° heparinized PBS (10 units/mL), 100 mL 4% 37° PFA, and finally 30 mL of a solution of 3% gelatin with 2.5 mg/ml FITC-albumin (Sigma-Aldrich, MO, USA, #A9771) to create a fluorescent vascular cast (Matthias F Valverde Salzmann et al. 2011). The animal is submerged in 4% cold PFA for 4-8 hours to completely harden the vascular cast at which point the brain is dissected and stored in 1X PBS with 0.02% sodium azide at 4°C.

2.7.8 Immunohistochemistry and clearing

Whole mount testing

Optimization of MarmoClear was conducted by comparing whole mount clearing technique adaptations to published versions of iDisco+ (Branch et al. 2019) in coordination with the Wu Lab at Mount Sinai. Briefly, the finalized version of MarmoClear consists of delipidating the brain with a tri-phasic solution of 4% SDS, 2-methyl-2-butanol, and 2-propanol, washing daily for two weeks with ratios titrated to match each individual brain. The brain can then be transitioned to an aqueous solution with Triton X-100, glycine, and a 1:4 mixture of 10N NaOH and 20% NaN3. The brain is then submerged in a high refractive index aqueous clearing media matching the pH and phobicity of the remaining tissue. Measurements of transmittance and scattering in the bright and dark field images, respectively, were made by first taking all images and converting into grayscale for a common reference frame for comparison and then, establishing a background measure of each imaging modality. To measure the proportion of light transmitted, we took a series of measurements across the center of the brain where there is the most absorption, and divided them by the background image representing 100% transmittance. Higher transmittance values are indicative of clearer tissue. To measure the amount of scattered light, we again took a series of measurements across the brain sample, notably, at the edges where there is the highest incident of scattering due to refraction. The amount of scattering is best determined by taking the measured difference in scattering of sample – baseline and dividing this by the original baseline to transform the values into proportions that can easily be compared to the transmittance data. Differences are measured with a two-tailed t-test with a p-value of 0.5.

Whole mount antibody testing shown in Fig 2.13 was carried out following clearing and utilizes the same procedure as stated in the antibody screen with the exception that each incubation period was two weeks.

The volumes are then imaged on a light-sheet microscope (Ultramicroscope II, LaVision, Biotex) equipped with a 1.3X objective lens and sCMOs camera (Andor Neo). Images will be acquired with the ImspectorPro software (LaVision, BioTec) and are scanned at 488, 561, 640, and 785 nm laser channels with a step size of 3 μm. Whole-tissue images from the scanned volumes will be generated using Imaris x64 software (Bitplane). 3D reconstruction and alignment of volumes will be done using the "volume rendering" function.

Antibody screen

Potential antibodies were collected across vendors, Johns Hopkins University, and UC Davis/NIH NeuroMab facility. Marmoset brains were cleared and mounted with 2% agarose and cut into 50 um free floating sections with vibratome. All brain sections were washed with permeabilization buffer with heparin followed by incubation with the primary antibody at a dilution of 1 ug/800uL solution over night at room temperature. The list of primaries tested can be found in Table 2.6. Following sequential washes with permeabilization buffer with heparain, the antibodies were incubated with the species specific 594-conjugated. Options included: pDk-anti-Gt-A488, Invitrogen, Catalog #A11055, Lot #1687906; pGt-anti-MsIgG2a-A488, Invitrogen, Catalog #A21131, Lot

#2045338; pDk-anti-Rb-A568, Invitrogen, Catalog #A10042, Lot #1235798; pGt-anti-MsIgG2c-A594, Jackson ImmunoResearch, Catalog #115-585-208, Lot #118467; mRt-anti-MsIgG2b-A647, Abcam, Catalog #ab172327, Lot #GR3256422-2; pGt-anti-MsIgG1-A647, Invitrogen, Catalog #A21240, Lot #2012512. Incubation with secondary was at a dilution of 1-2 uL/800 uL overnight at room temperature. The sections are again sequentially washed with permeabilization buffer, washed again with PBS, and mounted on a slide in clearing buffer. For the screen, all sections were imaged on a Nikon Eclipse 90i at exposures of 30 ms and 1000 ms.

Sequential staining

The same method was used for antibodies followed the same procedure as the antibody screen with the exception that the sections were cut to 100 um to allow for more issue integrity upon imaging every section in clearing buffer, it was subsequently carefully removed from the slide and washed back into permebilization buffer for the next round of staining. The primary antibodies included pGt-anti-CALB2, Swant, Catalog #CG1, Lot #1§.1, 1ug:800uL staining dilution; pRb-anti-CALB1, Chemicon, Catalog #AB1778, Lot #25040385, 1ug:800uL staining dilution; mRtIgG2b-anti-nNOS, NeuroMab, Clone L121/25, purified, Lot #4559J0100, 1ug:800uL staining dilution; mMsIgG2a-anti-NPY, NeuroMab, Clone L115/13, purified, Lot #4559J024, 1ug:800uL staining dilution; pRb-anti-PVALB, Abcam, Catalog #ab181086, Lot #GR164340-1, 1ug:800uL staining dilution; mMsIgG1-anti-NeuN, Chemicon, Clone A60, Catalog #MAB377, Lot #3189194, 1ug:800uL staining dilution; mMsIgG2c-anti-HDGF, JHU/CDI, CloneYP190.1.1F2, Lot #20180531, 1ug:800uL staining; mMsIgG1-anti-GFAP, NeuroMab, Clone N206A/8, supernatant, Lot #N206A/8.1 IM, 50uL:750uL staining dilution. The nuclear dye used was YOSeta-1, SETA BioMedicals, Catalog #K8-2100. The secondaries used were the same as those used in the antibody screen. Sections were imaged on a Nikon Eclipse 90i at exposures of 30 ms and 1000 ms for rounds 1 and 2. For Round 3, they were imaged on a Keyence BZ-X800 at exposures of 14 ms and 133 ms.

Table 2.6 Antibodies screened

Target	Host	Source	Clone ID	Catalog #	Lot #	Result
CALB1	mMs-IgG1	NeuroMab	L109/57		L109/57.1 IM	Positive
CALB1	mRb	Cell Signaling		2173S	1	Positive
CALB1	pRb	CHEMICON		AB1778	25040385	Positive
CALB1	mMs	From MBH				Positive
CALB1	pRb	Swant		CB38		Positive
CALB2	mMs-IgG1	JHU/CDI	CLRT-7F1		20181030	Positive
CALB2	mMs-IgG1	JHU/CDI	CAL-5F1		20181030	Positive
CALB2	pRb	Swant		CR7697		Positive
CALB2	pGt	Swant		CG1	1§.1	Positive
DRAP1	mMs-IgG2b	JHU/CDI	R1545.1.1A8		20170606.IJVR	Positive
DRAP1	mMs-IgG2b	JHU/CDI	R1545.1.1A12		20180531	Positive
EZH1	mMs	JHU/CDI	YP907.1.2B9		20160606.IJVR	Positive
FOXP4	mMs-IgG2b	JHU/CDI	R1108.1.1D1		20151210.KRR.GMR	Positive
GFAP	mMs-IgG1	NeuroMab	N206A/8		N206A/8.1 IM	Positive
HDGF	mMs-IgG2c	JHU/CDI	YP190.1.1F2		20180531	Positive
HMBOX1	mMs	JHU/CDI	YP298.1.1E10		20150930.IJVR	Positive
ISL1	mMs-IgG1	DSHB	40.3A4		10/17/19	Positive
KIAA1967	mMs-IgG2b	JHU/CDI	YP256.1.1B5		20160114.IJVR	Positive
KLF10	mMs-IgG2a	JHU/CDI	R846.1.1D3		20170525.IJVR	Positive
LHX2	mMs-IgG2c	JHU/CDI	R911.1.2E3		20181011	Positive
LHX2	mMs-IgG2a	JHU/CDI	R911.1.2C10		20170404.IJVR	Positive
LRRK1	mMs-IgG1	NeuroMab	N341/12		N341/12.5	Positive
MAFG	mMs-IgG2a	JHU/CDI	R1035.1.1H7		20170710.IJVR	Positive
MED1	mMs-IgG2b	JHU/CDI	YP253.1.1A11		20170710.IJVR	Positive
MEIS2	mMs-IgG2a	JHU/CDI	R1403.1.1A11		20170525.IJVR	Positive
MYSM1	mMs	JHU/CDI	YP790.1.1B11		20160414.IJVR	Positive
MYT1	mMs	JHU/CDI	YP687.1.2B6		20160706.IJVR	Positive
NEUN	mMs-IgG1	Millipore	A60	MAB377		Positive
NEUN	mMs-IgG2b	BioLengend	1B7	834502	B305726	Positive
NEUN	mRb	Abcam	EPR12763	ab177487	GR3250076-4	Positive
NFIA	mMs	JHU/CDI	R1356.1.2A8		20150318.LAS	Positive
NKX2-2	mMs-IgG2b	DSHB	74.5A5		0	Positive
NNOS	mMs-IgG2b	NeuroMab	L121/25		L121/25.1.3 IM	Positive
NOS1	mMs-IgG2b	NeuroMab	L121/42		L121/42.2 IM	Positive
NOTCH1	mRt	DSHB	bTAN 20		12/15/16	Positive
NPY	mMs-IgG2a	NeuroMab	L115/13		L115/13.3 IM	Positive
PBX2	mMs	JHU/CDI	YP235.1.1D3		20150909.IJVR	Positive
POU4F2	mMs-IgG2c	JHU/CDI	R1356.1.2C6		20180830	Positive
PV	pRb	Abcam		ab11427		Positive
PV	mRb	Abcam		ab181086		Positive
PV	pRb	Swant		PV27		Positive
SMAD2	mMs-IgG2c	DSHB	PCRP-SMAD2-1B10		5/2/19	Positive
SST	pRb	Abcam		ab64053		Positive
SUV420H1	mMs	JHU/CDI	YP216.1.1F11		20160706.IJVR	Positive
TFCP2	mMs-IgG2b	JHU/CDI	R1141.1.3B1		20141117.LRH	Positive
TP63	mMs-IgG2b	JHU/CDI	YP273.1.2A11		20150921.GMR.IJVR	Positive
USF2	mMs-IgG2c	JHU/CDI	R1156.1.1A7		20170608.IJVR	Positive
ZFP3	mMs	JHU/CDI	YP251.1.1B2		20150914.IJVR.GMR	Positive
ZNF438	mMs-IgG2c	JHU/CDI	R1007.1.1H5		20140905.LRH	Positive
ZNF764	mMs	JHU/CDI	YP934.1.2A1		20160606.IJVR	Positive
ABTB1	mMs	JHU/CDI	YP155.1.1B4		20150723.L.I.G.K	Negative
ASH1L	mMs	JHU/CDI	R898.1.1A1		20160712.I.G.K	Negative
ATOH1	mMs-IgG1	DSHB	Math1 (Atoh1)		2/9/17	Negative
BRD4	mMs	JHU/CDI	YP241.1.1C9		20150909.IJVR	Negative
CALB1	mMs-IgG2b	JHU/CDI	CBN-4F1		20181030	Negative
CALB1	mMs-IgG1	JHU/CDI	CBN-2F7		20181030	Negative
CALB1	mMs-IgG2b	JHU/CDI	CBN-3H6		20181030	Negative
CALB1	mMs-IgG2b	NeuroMab	L109/39		L109/39.2 IM	Negative
CALB1	mMs-IgG1	Swant		300	07(F)	Negative
CALB2	mMs-IgG1	JHU/CDI	CLRT-3B12		20181030	Negative
CALB2	mMs-IgG2b	NeuroMab	L122/6		L122/6.2 IM	Negative

Target	Host	Source	Clone ID	Catalog #	Lot #	Result
CALB2	pGp	Swant		CRgp7	na	Negative
CHEK2	mMs-IgG1	JHU/CDI	R1521.1.2A2		20160114.IJVR	Negative
CTBP1	mMs-IgG1	JHU/CDI	R1443.1.1A1		20160114.IJVR	Negative
CTNNB1	mMs-IgG1	DSHB	PY654-B-catenin (IgG)		4/19/18	Negative
DEK	mMs	JHU/CDI	YP231.1.1B8		20150909.IJVR	Negative
EED	mMs	JHU/CDI	YP1017.1.1D2		20160712.I.G.K	Negative
EIF4G3	mMs	JHU/CDI	YP762.1.1A12		20160414.IJVR	Negative
ESR1	mMs-IgG1	DSHB	Eralpha BZ1		6/15/17	Negative
ESR2	mMs-IgG2b	DSHB	CWK-F12		12/28/17	Negative
EVX1	mMs-IgG2a	DSHB	99.1-3A2		2/25/16	Negative
EZH2	mMs-IgG2a	JHU/CDI	R1102.1.1B3		20170201	Negative
FOS	mMs-IgG1	DSHB	CPTC-FOS-2		2/21/19	Negative
FOS	mMs-IgG2a	DSHB	CPTC-FOS-4		9/12/19	Negative
FOS	mMs-IgG2b	DSHB	CPTC-FOS-1		1/18/18	Negative
FOS	mMs-IgG2b	DSHB	CPTC-FOS-3		2/21/19	Negative
FOSB	mMs-IgG2b	JHU/CDI	R1023.1.1C9		20150504.LAS.IJVR	Negative
FOXA2	mMs-IgG1	DSHB	4C7		5/18/17	Negative
HDAC7	mMs	JHU/CDI	YP311.1.1B6		20151012.IJVR	Negative
HELLS	mMs-IgG2b	JHU/CDI	YP239.1.2A3		20180918	Negative
HSF2	mMs	JHU/CDI	YP79.1.1E4		20150615.LAS.IJVR	Negative
HSFY1	mMs	JHU/CDI	YP693.1.1E2		20160404.IJVR	Negative
ING2	mMs	JHU/CDI	R1621.1.1E8		20150831.IJVR	Negative
ISL1	mMs-IgG1	DSHB	40.2D6		12/21/17	Negative
ISL1 & ISL2	mMs-IgG2b	DSHB	39.4D5		2/21/19	Negative
JMJD6	mMs	JHU/CDI	YP157.1.1B4		20150723.L.I.G.K	Negative
KDM5C	mMs	JHU/CDI	YP972.1.1E2		20160628.GMR.KRR	Negative
KDM5C	mMs	JHU/CDI	YP972.1.2A10		20160628.GMR.KRR	Negative
L3MBTL4	mMs	JHU/CDI	R160.1.1C8.4D1		20150112.L2E	Negative
LIM-3	mMs-IgG1	DSHB	67.4E12		3/17/16	Negative
LMX1B	mMs-IgG1	DSHB	50.5A5		9/13/18	Negative
MAPK1	mMs	JHU/CDI	YP195.1.1D5		20150819.LAS.KRR	Negative
MBD1	mMs	JHU/CDI	YP70.1.1G8		20150617.LAS.IJVR	Negative
MEIS2	mMs-IgG2a	JHU/CDI	R1403.1.2B4		20170606.IJVR	Negative
MNR2	mMs-IgG1	DSHB	81.5C10		6/28/18	Negative
MORF4L1	mMs	JHU/CDI	R1600.1.1D10		20150727.LAS.IJVR	Negative
MORF4L1	mMs	JHU/CDI	R1600.1.1F2		20150727.LAS.IJVR	Negative
MSX1,MSX2	mMs-IgG1	DSHB	4G1		2/7/19	Negative
MXI1	mMs	JHU/CDI	YP347.1.1H11		20151019.IJVR	Negative
MYOD1	mMs	JHU/CDI	YP629.1.1A7		20160404.IJVR	Negative
MYT1	mMs	JHU/CDI	YP687.1.2A8		20160706.IJVR	Negative
NFATC1	mMs-IgG1	DSHB	7A6		8/30/18	Negative
NFATC2	mMs-IgG2a	DSHB	G1-G9		3/19/15	Negative
NHLH1	mMs	JHU/CDI	YP832.1.2B10		20160518.IJVR	Negative
NKX2-2	mMs-IgG2b	DSHB	74.5A5		3/21/19	Negative
NKX6-1	mMs-IgG1	DSHB	F55A12		3/28/19	Negative
NPAS1	mMs	JHU/CDI	YP592.1.2D4		20160201.IJVR	Negative
NPY2R	mMs-IgG2a	NeuroMab	L119/106		L119/106.10.2	Negative
NR3C2	mMs-IgG1	DSHB	MRN3 3F10		4/5/18	Negative
NR3C2	mMs-IgG2a	DSHB	rMR365 4D6		12/6/18	Negative
NR3C2	mMs-IgG2b	DSHB	MRN2 2B7		4/5/18	Negative
NRF1	mMs-IgG2a	JHU/CDI	R157.1.3H3		20140422.DNF	Negative
NRF1	mMs-IgG2b	JHU/CDI	R157.1.3D4.4E7		20180904	Negative
NRF1	mMs-IgG2b	JHU/CDI	R157.1.3H1		20150611.LAS.IJVR	Negative
ORC2	mMs	JHU/CDI	YP779.1.1F3		20160414.IJVR	Negative
OVOL2	mMs-IgG1	JHU/CDI	YP263.1.1H12		20180531	Negative
PAX3	mMs-IgG2a	DSHB	Pax3		4/4/19	Negative
PAX7	mMs-IgG1	DSHB	PAX7		6/27/19	Negative
PDX1	mMs	JHU/CDI	YP931.1.2C9		20160606.00	Negative
PDX1	mMs-IgG1	DSHB	F109-D12		1/21/16	Negative
PECAM	mHm	DSHB	2H8		6/14/18	Negative
PIAS2	mMs	JHU/CDI	YP290.1.1C11		20151016.IJVR	Negative

Target	Host	Source	Clone ID	Catalog #	Lot #	Result
PRDM4	mMs-IgG1	JHU/CDI	YP463.1.2B3		20151116.I.G.K	Negative
PV	mMs-IgG2a	NeuroMab	L114/3		L114/3.3 IM	Negative
PV	mMs-IgG1	NeuroMab	L114/81		L114/81.7.1 Im	Negative
PVALB	pGt	Swant		PVG213	76	Negative
PVALB	pGp	Swant		GP72	na	Negative
Pyramidal	mMs-IgG2b	Swant		345	1.5	Negative
RFX3	mMs-IgG2b	JHU/CDI	YP63.1.1D11		20160114.IJVR	Negative
RLIM	mMs	JHU/CDI	YP617.1.1A2		20160201.IJVR	Negative
SCML4	mMs-IgG2c	JHU/CDI	YP491.1.1D6		20151214.IJVR	Negative
SMAD7	mMs-IgG2b	JHU/CDI	YP36.1.1D7		20160721.IJVR	Negative
SMNDC1	mMs	JHU/CDI	YP948.1.1A8		20160620.KRR.GMR	Negative
SRY	mMs	JHU/CDI	YP734.1.1B7		20160412.IJVR	Negative
SST	pRb	MyBioSource		MBS822270		Negative
STAT1	mMs-IgG2a	DSHB	AFFN-STAT1-20C2		4/2/15	Negative
STAT5A	mMs-IgG2a	DSHB	AFFN-STAT5A-7D8		4/16/15	Negative
TP63	mMs-IgG2b	JHU/CDI	YP273.1.2G3		20150921.GMR.IJVR	Negative
TSC22D4	mMs-IgG2a	JHU/CDI	R154.1.3E10		20150804.LAS.IJVR	Negative
VMAT2	mMs-IgG2b	NeuroMab	N449/73		N449/73.1	Negative
WDHD1	mMs-IgG1	JHU/CDI	R1251.1.1B10		20190710.00	Negative
ZBTB33	mMs	JHU/CDI	YP581.1.1D1		20160125.IJVR	Negative
ZBTB33	mMs	JHU/CDI	YP581.1.1D2		20160125.IJVR	Negative
ZHX3	mMs	JHU/CDI	YP350.1.1C5		20151019.IJVR	Negative
ZNF385A	mMs	JHU/CDI	YP976.1.1E9		20160712.I.G.K	Negative
ZNF691	mMs	JHU/CDI	YP307.1.2C8		20151019.IJVR	Negative
ZNF98	mMs-IgG1	JHU/CDI	R1259.1.1A11		20141229.LRH.LAS	Negative
ZSCAN2	mMs-IgG2c	JHU/CDI	R767.1.1F8		20170710.IJVR	Negative
CHAMP1	mMs	JHU/CDI	YP998.1.1G2		20160706.IJVR	Inconclusive
EN1	mMs-IgG1	DSHB	4G11		2/7/19	Inconclusive
HMGA1	mMs-IgG2b	JHU/CDI	R1299.1.1C3		20180531.00	Inconclusive
HOXC10	mMs-IgG1	DSHB	5G12-10		1/11/18	Inconclusive
HOXD8	mMs	JHU/CDI	YP723.1.1E9		20160412.IJVR	Inconclusive
ISL1	mMs-IgG2a	JHU/CDI	R1401.1.1D4		20150318.LAS	Inconclusive
ISL1	mMs-IgG1	DSHB	39.3F7		4/18/19	Inconclusive
JUN	mMs-IgG1	DSHB	CPTC-JUN-1		6/22/17	Inconclusive
JUN	mMs-IgG1	DSHB	CPTC-JUN-2		3/16/18	Inconclusive
JUN	mMs-IgG1	DSHB	CPTC-JUN-3		8/16/18	Inconclusive
LHX1	mMs-IgG1	DSHB	4F2		9/27/18	Inconclusive
MEIS2	mMs-IgG2a	JHU/CDI	R1403.1.2B3		20170705.IJVR	Inconclusive
MYOG	mMs-IgG1	DSHB	F5D		3/7/19	Inconclusive
NEUROG3	mMs-IgG1	DSHB	F25A1B3		5/31/18	Inconclusive
NFE2L2	mMs-IgG1	DSHB	PCRP-NFE2L2-1D12		7/11/19	Inconclusive
NKX6-1	mMs-IgG1	DSHB	F55A10		8/8/19	Inconclusive
NOTCH2	mRt	DSHB	C651.6DbHN		12/15/16	Inconclusive
NPAS1	mMs	JHU/CDI	YP592.1.1A11		20160201.IJVR	Inconclusive
NR3C2	mMs-IgG1	DSHB	rMR1-18 1D5		11/30/17	Inconclusive
PAX-6	mMs-IgG1	DSHB	PAX6		9/27/18	Inconclusive
PDX1	mMs-IgG1	DSHB	F6A11		12/17/15	Inconclusive
SIM1	mMs	JHU/CDI	YP869.1.2H7		20160530.IJVR	Inconclusive
STAT1	mMs-IgG2c	DSHB	AFFN-STAT1-1B1		4/19/18	Inconclusive
TFAP2A	mMs-IgG2b	DSHB	3B5		6/28/18	Inconclusive
VDR	mMs	JHU/CDI	YP634.1.1G12		20160328.IJVR	Inconclusive
ZNF691	mMs	JHU/CDI	YP307.1.3E9		20150930.IJVR	Inconclusive

CHAPTER 3. Cross species genetic comparisons to find a conserved signature related to the social brain

†Portions of the work in this chapter were accomplished with co-first authors, Willa Kerkhoff and Dakota Blackman, of the in-preparation manuscript resulting from this work. MF trained DB on rodent injections; WK and DB performed rodent injections and tissue harvesting. MF designed primate specific injection and extraction tools and procedures. MF, WK, and DB performed primate injections and tissue harvesting. WK and DB performed TRAP on extracted RNA. DB performed histology. WK conducted literature review and assembled retro-vTRAP methods. MF conducted analyses, created figures.

3.1 Dissecting the social brain through specific projections

Social interaction between members of a species is essential for species survival, and a deep complexity of social behavior has long been considered a unifying hallmark of human and non-human primate species. Both rodents and non-human primates have been widely explored as models of social behavior (Cacioppo 2002; Crawley et al. 2007; Insel and Fernald 2004; Silverman et al. 2010) Mice and rats have been used across multiple fields to model social behavior and its deterioration in transgenic models of psychological disorders (Ben-Ami Bartal et al. 2014; Kingsbury et al. 2019; Nestler and Hyman 2010; Silverman et al. 2010) Likewise, extensive work in marmoset (*Callithrix jacchus)* and macaque (*Macaca fascicularis*) monkeys has been essential in understanding the neural basis of behaviors beyond what can be effectively modeled in rodents (Machado and Bachevalier 2003; Miller et al. 2016b; Prins et al. 2017; de Waal 1989). Given the commonalities seen amongst the complexity and diversity of social behavior observed, it is not irresponsible to expect conserved neural substrates with phylogenetic continuity to operate across these four species (Skuse and Gallagher 2011). We hypothesize that projections related to these behaviors may be genetically specific to support complex cognition.

The prefrontal cortex (PFC) is known to facilitate social cognition across mammalian species (Adolphs 2009; Levy et al. 2019; Watson and Platt 2012). In particular, the human mPFC has been demonstrated to be a crucial subregion associated with social behavior and cognition, as demonstrated in both imaging studies (Dolan 2002; Grossmann 2013; Krueger, Barbey, and Grafman 2009; Y. Yang and Raine 2009) and lesion studies (S. W. Anderson et al. 1999; Eslinger, Flaherty-Craig, and Benton 2004; Forbes and Grafman 2010). Dysfunction of the mPFC has been shown in rodent models of depression and anxiety associated with social defeat and chronic mild stress (Belleau, Treadway, and Pizzagalli 2019; Seo et al. 2017; Vialou et al. 2014).

Although, there are ongoing questions within the field as to the existence of a homologous rodent mPFC (Dalley, Cardinal, and Robbins 2004; Wise 2008), recent reviews suggest that there is, in fact, functional as well as anatomical homology between the rodent and human mPFC (Schilman et al. 2008). The most significant interspecies difference is in the level of social cognition being supported by the conserved mPFC (Ko 2017).

Furthermore, comparisons between rodents and non-human primates have shown homologous corticostriatal projections from the mPFC to the shell of the nucleus accumbens (NAc), a large region within the ventral striatum. The NAc is a well-characterized and evolutionarily conserved region of the mammalian brain that is involved in similar social behaviors in both rodents and non-human primates. Specifically, the glutamatergic pyramidal neural projection running from layer V of the mPFC to the shell of the NAc has been identified in rats and macaques through both anterograde and retrograde tracing (Wise 2008). Low-frequency acute stimulation of the mPFC layer V has been shown to decrease immobility time in the forced swim test, as well as increasing time in the open arms of an elevated plus maze. This suggests a role for corticostriatal layer V projection neurons in anti-depressive deep brain stimulation treatments (S. Kumar et al. 2013). Previous studies of the corticoaccumbal projection in mice have shown an association with social interaction (Riga et al. 2014). Photoactivation of the mPFC to NAc projection in animals with a susceptibility to social stress has been shown to have a robust antidepressive effect, indicated by increased sucrose preference and social interaction following activation (Covington et al. 2010). Stimulation of this layer V corticoaccumbal projection was also shown to reverse cholecystokinin (CCK)-induced social avoidance and sucrose preference deficits (Vialou et al. 2014). Taken together, the anatomical, functional, and behavioral data suggest that the conserved excitatory projection between layer V of the mPFC and the NAc is a robust candidate through which to explore whether there are specifically conserved genetic signatures supporting the social brain across both rodents and non-human primates.

3.2 Molecular techniques to assess genetic signatures of neural projections

In order to separate a genetically-defined subpopulation of cells from the complex and heterogeneous tissue of the cortex, we chose to develop and implement a variant of the translating ribosome affinity purification (TRAP) technique. By expressing an EGFP-tagged ribosome protein L10a (*EGFPL10a*) in genetically-defined cell populations, TRAP enabled the isolation of cell type-specific polysome-bound mRNAs from heterogeneous tissue homogenates, avoiding potential adaptations and RNA degradation common in some other cellular isolation methods (Heiman et al. 2014). TRAP has been used previously to profile a variety of distinct cell types in the mouse CNS (Doyle et al. 2008; Mellén et al. 2012; Nakajima, Görlich, and Heintz 2014; Schmidt et al. 2012; Shrestha, Mousa, and Heintz 2015). Most previous applications of TRAP have been reliant on the strength and availability of mouse strains that have been engineered to express *EGFPL10a*. The generation of novel bacterial artificial chromosomes (BAC) transgenic mouse lines has enabled the success of the "bacTRAP" method (Doyle et al. 2008; Nakajima, Görlich, and Heintz 2014; Schmidt et al. 2012; Shrestha, Mousa, and Heintz 2015). Other studies have demonstrated a comparable technique using tetracycline (Drane et al. 2014) or Cre recombinase (Jing Liu et al. 2014; Sanz et al. 2009; S. Stanley et al. 2013; Zhou et al. 2013) dependent expression. Despite the great success of this transgenic-based approach, it has limited applications of TRAP predominantly to mouse models. However, in recent years it has been shown that Cre-dependent adeno-associated viruses (AAVs) expressing the TRAP *EGFPL10a* transgene can be used to target spatially and genetically defined cell types, producing results that fully

recapitulate the original bacTRAP method with a new method known as viral TRAP or vTRAP (Nectow et al. 2017; Schneeberger et al. 2018).

An additional development in recent years has been a new rAAV variant (rAAV2-retro) engineered through *in vivo* directed evolution and has been shown to be robustly internalized by axons, cell bodies, and presents comparable retrograde transport and efficacy to classical retrograde labeling agents (Tervo, Hwang, Viswanathan, Gaj, Lavzin, Ritola, et al. 2016).

With the available technologies, we have elected to combine a number of strengths of each in order to utilize TRAP in wild type animals of multiple species to specifically begin to dissect pathways of the social brain. We have combined rAAV2-retro with the *EGFPL10a* transgene under a pan-cellular promoter, Ef1a, such that there is no need for a Cre-driver line to define specificity, but instead, we isolated our neural projection population of choice through specific injection in its target.

Thus, virally targeting the terminals of our chosen projection neurons in the NAc induced *EGFPL10a* expression along the axon and in the cell bodies in the mPFC, allowing TRAP to be performed across species without transgenic constraints. We term this method as retrograde viral TRAP, or "retro-vTRAP."

3.3 Implementation of retro-vTRAP in four species

Here we describe a cross-species genetic comparison of corticoaccumbal layer V projection neurons in mice, rats, marmosets, and macaques. We demonstrated the incorporation of virally expressed *EGFPL10a* and validate the retro-vTRAP approach in wild type animals across all four species of interest. In order to ensure that the *EGFPL10a* transgene was successfully transduced by neurons in the mPFC in all four species subsequent to injection in the NAc, we performed qPCR on all four species (Fig 3.2) and conducted histological confirmation in mouse, rat, and marmoset samples (Fig 3.3). Due to the limited availability of the macaques, we dedicated our two subjects both to TRAP profiling. Upon injecting the retro-vTRAP into NAc coordinates, confirming the efficiency of the virus, the injection locations, and the successful retrograde transportation as evidenced by the enrichment of EGFP in mPFC samples measured through qPCR, we then were able to create cDNA libraries for each sample and perform RNA-seq on all mPFC samples to specifically probe the genetic signature of this projection population.

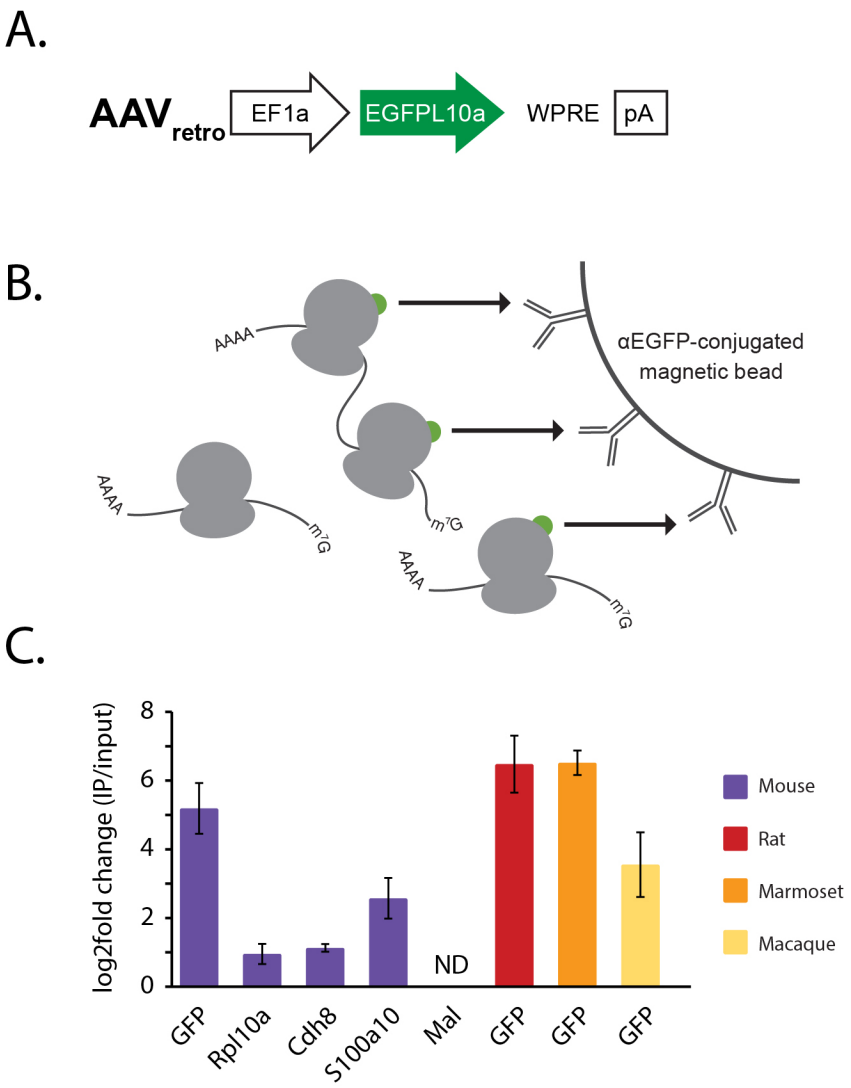

Figure 3.1 TRAP purification of *EGFPL10a* from projection neurons
A. Schematic diagram of retro-vTRAP viral vector showing the EF1a promoter, the *EGFPL10a* transgene, the WPRE cassette, and the polyadenylation stop cassette (pA). B. Schematic depicting the TRAP protocol in which EFGP-tagged ribosomes from tissue homogentaes are purified using magnetic beads coated with anti-EGFP antibodies. Bound mRNA is then extracted and analyzed by RNA-seq. C. qPCR (mean±SEM) of TRAP RNA for EFGP shows enrichment in the IP compared to input for all four species. Ribosomal subunit maker *Rpl10a* is enriched with cortico-striatal markers *Cdh8* and *S100a10* in the mouse samples and glial maker *Mal* was not detected.

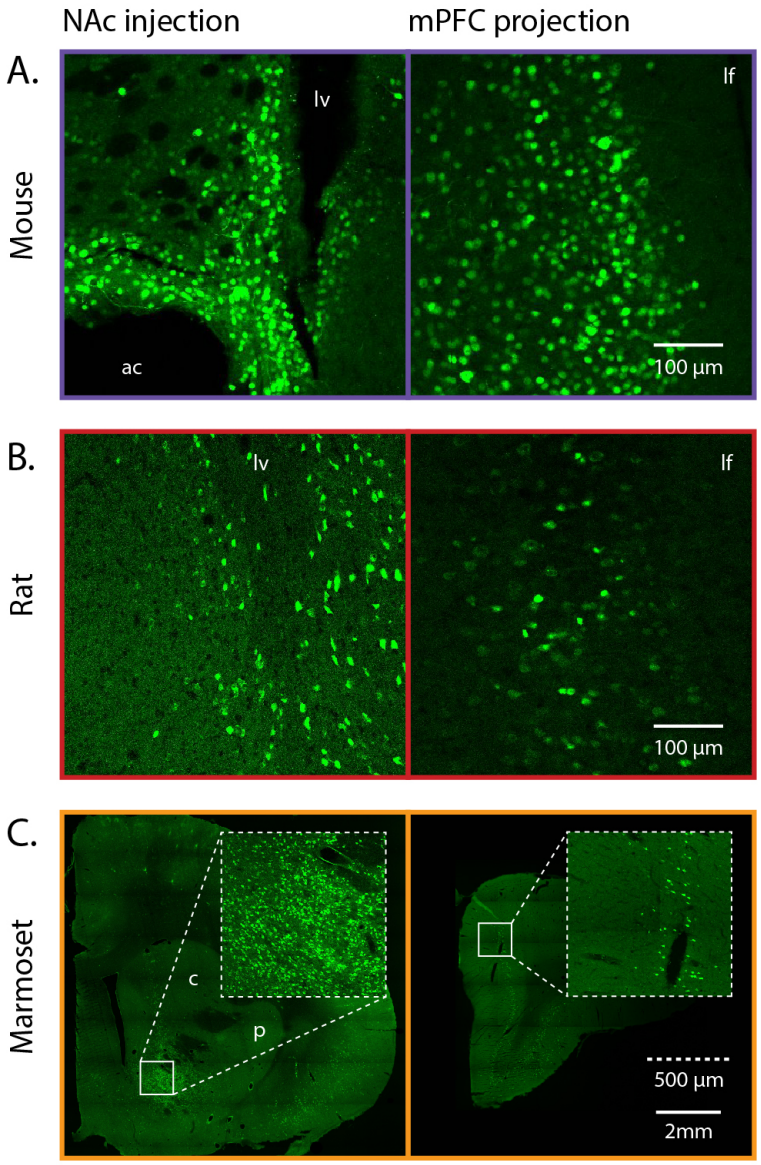

Figure 3.2 Retrograde labeling of projection neuron populations with retro-vTRAP

A. EGFP expression in a mouse brain following injections of retro-vTRAP into the NAc. Labeled cells can be seen at both the injection site (left) and in the cortex (right). B. EGFP expression in a rat brain following injections of retro-vTRAP into the NAc. Labeled cells can be seen at both the injection site (left) and in the cortex (right). C. EGFP expression in the marmoset brain following injections of retro-vTRAP at both the injection site (left) and in the cortex (right). Insets show the enlarged regions that correspond to the panels in A and B. Full slices are shown for spatial reference with annotated landmarks. ac, anterior commissure; c, caudate; caudate; lf, longitudinal fissure; lv, lateral ventricle; p, putamen.

Given the different preparations of tissue extraction detailed in the Methods section, we conducted basic RNA metrics analyses on each individual sample (Fig 3.3) to account for interspecies differences. The results of RNA-seq and the assignment of reads to genes are dependent on the quality of the sample and the reference genome. If there are large gaps, missing sections, or incomplete annotation records, reads will not be included in the total mRNA count. In Fig 3.3.A and Fig 3.3.B, we calculated the total proportion of read counts assigned to intergenic bases, intronic bases, untranslated region bases, and coding bases. The last two combine to represent the total amount of mRNA coding bases. Given the common utility of mice in TRAP studies, we can confirm that approximately 60% mRNA coding reads for both IP and input samples is a standard bar of sample quality. As such, the reduced proportion of these reads in our three remaining samples initially drew into question the quality of the samples. We then examined the quality metrics of the genomes as provided by NCBI. Two measures in particular capture the quality of the genome. The Contig N50 approximates the length of the sequence needed to cover 50% of the genome. A higher Contig N50 represents the fact that the genome is annotated with large contigs. Due to their large size, it necessitates fewer contigs to cover the entire genome. As a result, the number of contigs is lower in genomes with better coverage. Looking at these two measures in our sample plotted on a log scale (Fig 3.3.C), it was strikingly clear that the mouse genome is of much higher quality than any of the three other species. One relational observation is that the marmoset has the poorest genome by these measures and also has the smallest proportion of UTR bases in the reads. Accounting for the relationship between our IP and input sample metrics and the similar pattern found in the genome quality measures, we concluded that the quality of our samples is sufficient to proceed.

3.4 Common enrichment and depletion profiles within each species

We hypothesized that in comparing across four species, if we were able to demonstrate conserved gene expression profiles for sets of genes with known roles, it would establish a baseline from which we can explore the data set for novel targets with confidence. To do this, we took two approaches. The first approach was the mapping of individual genes against a reference genome in the Integrative Genomics Viewer (Broad Institute, MA, USA). We *a priori* identified a list of genes with expected enrichment or depletion profiles in IP and input samples. We then plotted the 15 genes across representative samples taken from all four species and scaled the maximum read count to be equal within each gene sample comparison (Fig 3.4). The gene groups included expected positively enriched genes including *Neurod6*, a neurogenic differentiation factor, *Scl17a7*, vesicular glutamate transport protein, *Tbr1*, indicator of glutamatergic projection neuron differentiation, *Cdh8*, a neuronal cadherin known to cortico-striatal networks (Friedman et al. 2015), and *Cplx2*, a synaptic vesicle membrane protein. Indeed, Fig 3.4.A shows relative enrichment in all IP samples compared to input. The second group of genes of interest included negative controls or genes that you would expect to find predominately in the input. These include *Gfap*, an

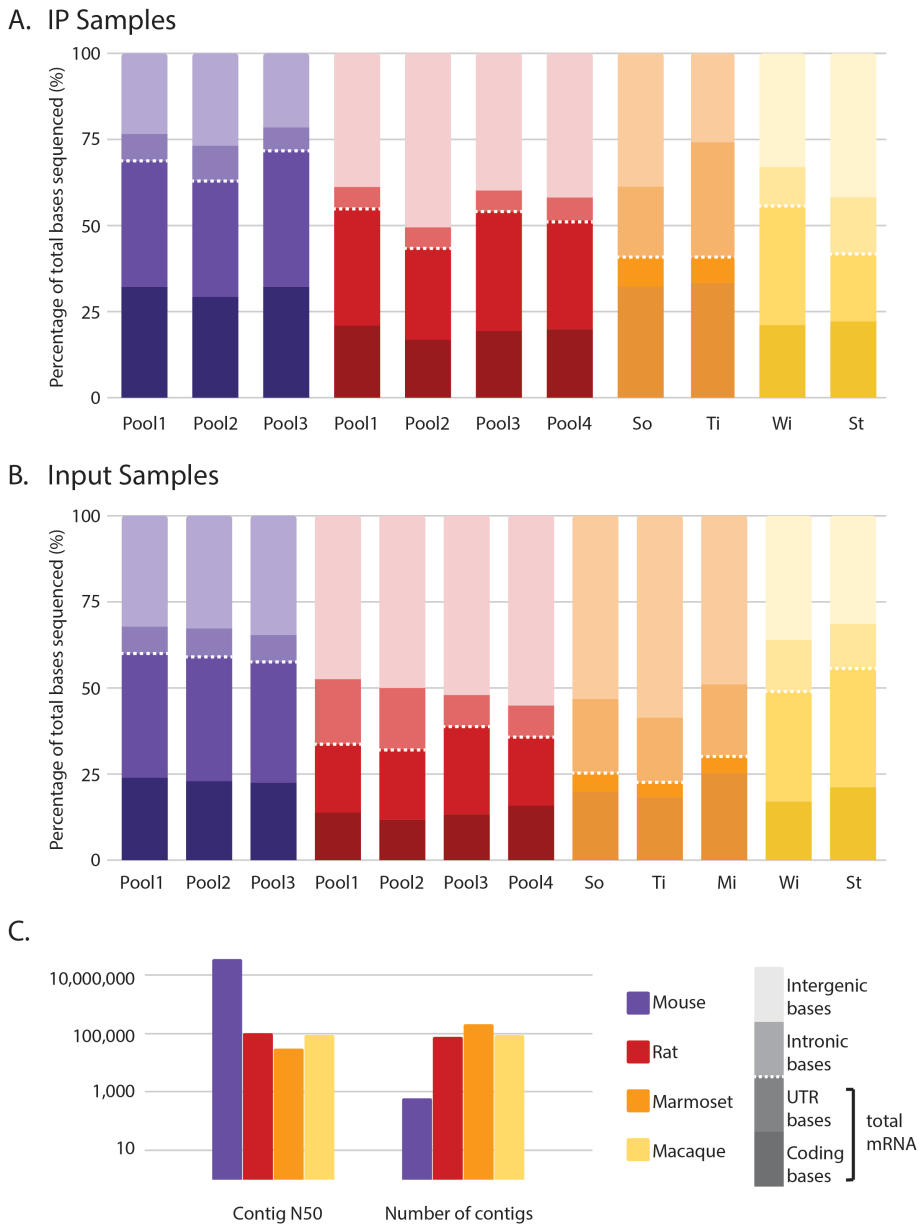

Figure 3.3 RNA metrics and genome comparisons
A. For each IP sample in our study, we plot the proportion of reads as they are classified into intergenic bases, intronic bases, untranslated region bases, or coding bases. The darker shades of each color corresponding to the two lower bars beneath the dotted white line, can be summed together to approximate total mRNA. The color of the bar denotes the species to which the sample belongs. Mouse, purple; rat, red; marmoset, orange; macaque, yellow. B. Follows the same structure as A, but for input samples. C. Two measures of genome quality across all four species.

astrocyte marker, *Cnp*, *Mal*, and *Olig2*, oligodendrocyte markers, and *Slc1a3*, which encodes a glutamate transport protein found mostly at axon terminals (Fig 3.4.B). These all showed expected respective enrichment in the input samples given the expected heterogeneity of the cell types in the input distinct from the purified IP projection neurons. Lastly, we had a second group of negative controls expressing that are all known interneuron markers including *Gad1*, *Vip*, *Sst*, *Pvalb*, and *Npy* (Fig 3.4.C). These likewise all showed enrichment only in the input samples. Due to the fact that these are single samples and not normalized read counts, little can be drawn about how the statistics of these gene groups compare against samples and species. Nevertheless, confirming this expected pattern of enrichment in control genes in IP and corresponding enrichment of negative control genes in the input suggested that we isolated the specific population of projection neurons targeted across all four species.

Next, we performed a quantitative differential analysis to determine which specific genes were enriched or depleted within each species (Fig. 3.5). We initially created a correlation matrix describing the sample distance between all of our samples per species. As indicated in Fig 3.5.A-D.i., the darker blue colors indicate more homogeneity in the resultant expression profile. It is expected that IPs and inputs would cluster together, as was shown for all of our species. The clusters are not dependent on the size factor of the absolute read count. We preformed this control to ensure that an overly represented and sequenced sample did not drive the statistics of the correlation. The correlation matrix in Fig 3.5.C.i did indicate that the marmoset IP samples were more correlated with each other than with the inputs, but sample So still shared a low sample distance with the inputs. This was the least well-segregated population of the four species.

This finding was then further confirmed by plotting all IP and inputs using principal component analysis (PCA) to reveal the major sources of variation in the data (Fig 3.5.A-D.ii.). For all samples, PC1 accounted for the most variance, but again, the marmosets revealed that although there was a clear separation of the IPs and inputs, there was a single sample that had reduced variance from the inputs in PC1. Nevertheless, the clear clustering of the data allowed us to test whether or not there were any genes in these data sets with significant enrichment or depletion profiles. PCA served as our only filter for including or excluding data samples from all those collected. If the input values all clustered with an IP as well, that particular IP was removed from subsequent analyses as it was an indication that the TRAP procedure failed to isolate the specific population of interest. The samples included in Fig 3.5 were the final samples used for the remainder of the analyses.

For this, we compared the log2 fold change expression of genes in IP samples minus those in the input samples using a DESeq2 normalization method (Love, Huber, and Anders 2014). We applied a Benjamini Hochberg multicomparison test and established a cut-off value of $p<0.05$. We collapsed all of our samples and genes into discrete, comparable data points. These data were plotted in two manners, as MA plots and volcano plots (Fig 3.5.A-D.iii. and Fig 3.5.A-D.iv., respectively). MA plots demonstrate the expression level as well as the direction

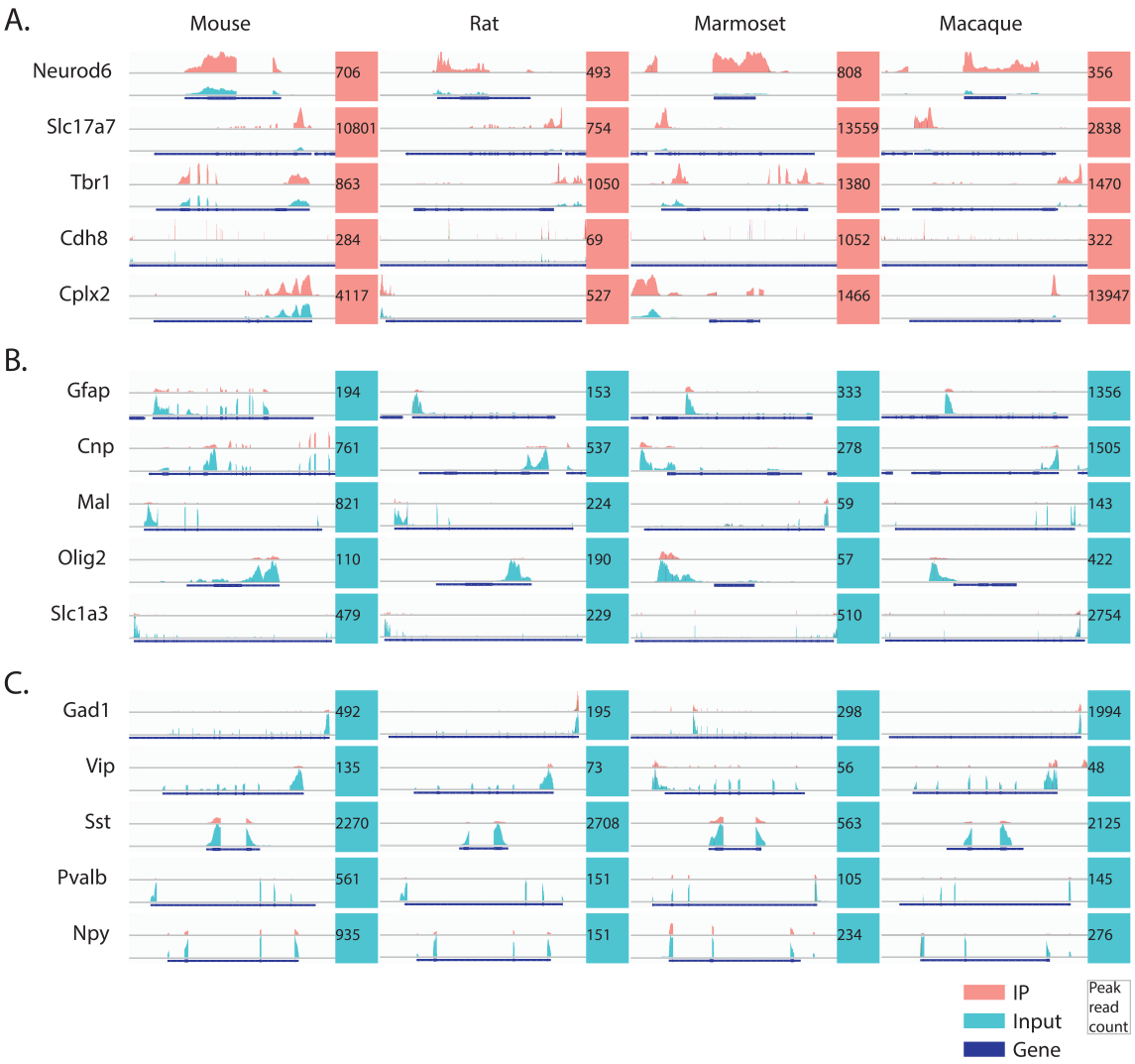

Figure 3.4 Visualization of key gene sets from TRAP data
All IP samples are shown in red with all input samples shown in teal. Each column is a different species. Each row is a different gene. Every gene is plotted against a reference sequence for each gene shown in blue. The thicker sections of each gene are the exons. The reference sequence is specific to each species. To the right of each gene is a box that indicates the peak read count of this gene to which both the IP and input are scaled. The color of the box indicates which sample has the higher peak, red for IP; teal for input. A. Positive control genes related to known excitatory and projection neuron markers. B. Negative control genes related to known input enriched cell types. C. Negative control genes related to interneuron classes of cells.

and degree of change by plotting the fold change expression difference against the normalized sequencing base counts. As expected, we saw a range of fold change across all sequencing sizes. Volcano plots reveal the significance of the change by plotting the statistical significance as measured by the absolute Wald statistic against the fold change of expression. All genes that passed the significance test in these two plots were indicated with a bold data point whereas those that failed were rendered transparent. Within each species we have genes that reached significance across all fold change comparisons.

We performed hierarchical clustering on the genes that reach significance within each sample to see how the enrichment and depletion profiles differed between samples (Fig 3.5.A-D.v.). As dictated by the hierarchical clustering algorithm, we saw expected clustering of enriched and depleted genes across all samples and species. Particularly of note, we found a small subset of genes in one marmoset sample, So-IP, whose enrichment profile was more closely matched to the corresponding input samples than the counterpart IP sample. This portion of genes likely accounted for the lower captured variance in the PCA plots for this sample. However, when taking the clustering of genes as a whole, the predominance of enriched and depleted genes between samples clearly clustered the IP samples together and the input samples together.

3.5 Identification of conserved gene ontology set across four species

With the confirmation that there were distinct sets of genes that were significantly enriched or depleted across all samples and species, we then asked whether or not there were any conserved genes across these four samples, and if so, were there any shared functional groupings that defined this population of projection neurons? To answer these questions, it was necessary to identify common orthologs across all four species (Fig 3.6). We restricted our data to orthologs rather than paralogs so that we were able to capture signals specific to speciation events. To define the orthologs across such differently annotated genomes, we employed curated phylogenitcs analysis in ENSEMBL and restricted genes to direct one-to-one matches (Vilella et al. 2009). In order to determine if any species had a disproportionate amount of conserved genes, we first measured the number of genes within each annotation (Fig 3.6.A, left). As expected from the annotation metrics in Fig 3.3, the mouse had far more genes annotated than any of the other species. In order to restrict our analyses only to genes that can be equivalently analyzed across species, we restricted the conserved genes found to those in the macaque annotation. Upon filtering based on the macaque, we plotted the proportion of overlapping genes per species (Fig. 3.6.A, right). We were left with 13,206 remaining conserved orthologs across the four species. Due to this strict criterion, we will be unable to make any claims regarding nonconserved genes or genes that are conserved but are not annotated. Nevertheless, our confidence was raised in our positive results. We then took the conserved gene list and created a hierarchically clustered heat map utilizing all conserved genes (Fig 3.6.B, left). Upon further restricting this list only to genes that are significantly enriched in one or more species, we revealed the pattern that the mouse and rat expression profiles were most similar to each other, followed by the marmoset. The macaque expression profile was starkly different

Figure 3.5 Differential analyses IP to Input within each species
Columns A, B, C, and D represent data for mouse, rat, marmoset, and macaque, respectively. Rows i, ii, iii, iv, and v maintain the same structure across all four species. i. Correlation matrix for sample distance with dark blue indicating low sample distance and light blue indicating high sample distance. Samples are indicated with their name at the bottom of each color and are color coded to indicate species. At the top of each column, the clusters are also color coded with pink, IP; teal, input; and the shades of green indicating the sample size of read count per sample. ii. PCA plots display the separation of samples along the major sources of variation in the data. All plots are PC2 against PC1. The numbers in each corner indicate the percentage of variance captured by that PC. Samples are color coded to indicate IP, pink and input; teal. iii. MA plots demonstrating the log2 fold change for IP minus input along the y-axis against the log2 base mean on the x-axis. iv. Volcano plots demonstrating the absolute Wald statistic indicating significance on the y-axis against the log2 fold change on the x-axis. For both iii. and iv., genes that pass the significance test are indicated with an opaque, bolded data point whereas those that fail to reach significance are rendered transparent. iv. Sample and gene heatmaps across all four species. Color bar indicates the z-score scaled expression values for significantly differential genes between IP and input. Samples are indicated with their name at the bottom of each color and are color coded to indicate species. At the top of each column, the clusters are also color coded with pink, IP; teal, input; and the shades of green indicating the sample size of read count per sample.

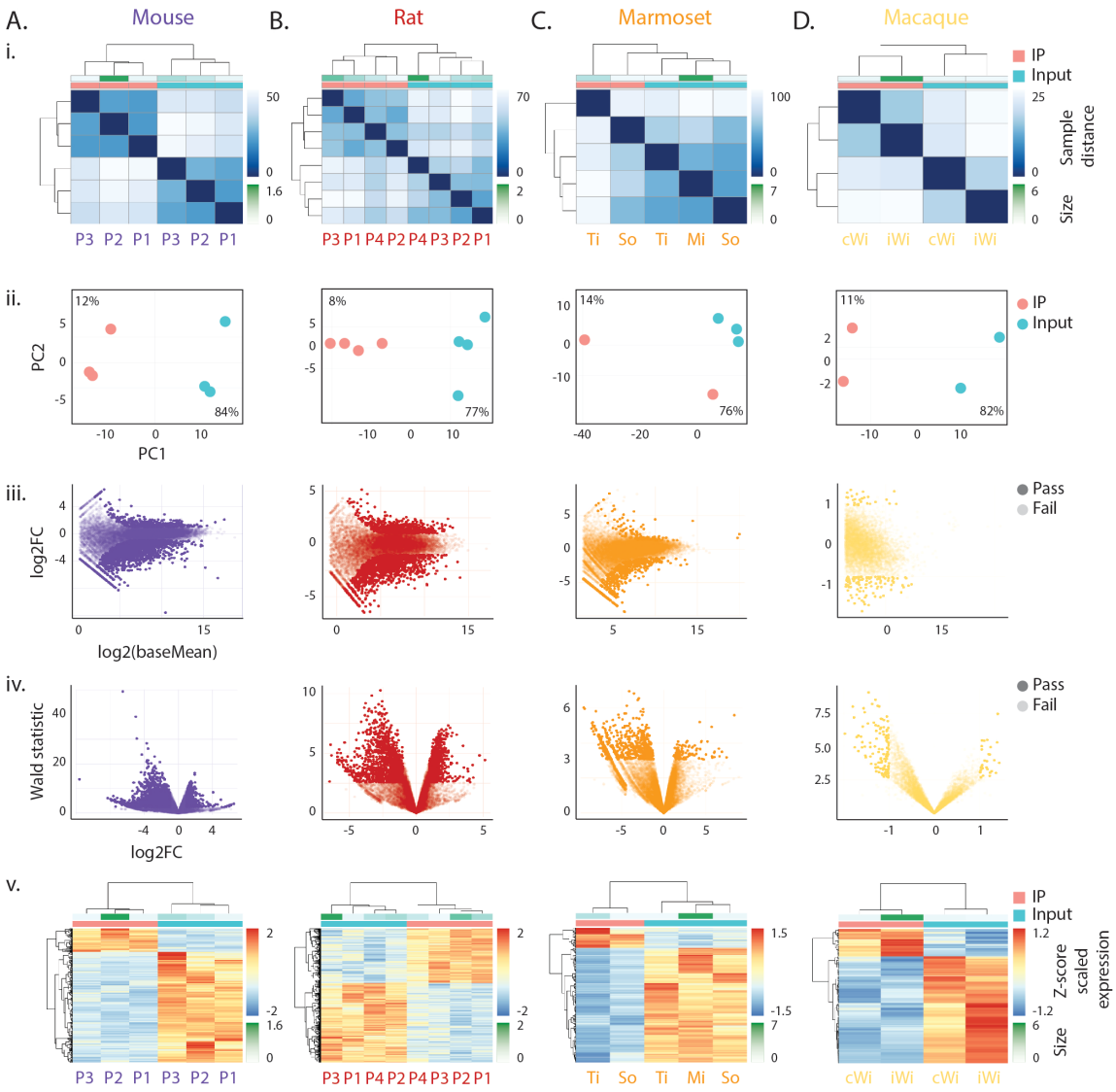
A.
Mouse
B.
Rat
C.
Marmoset
D.
Macaque
i.
IP
Input
Sample distance
Size
P3 P2 P1 P3 P2 P1
P3 P1 P4 P2 P4 P3 P2 P1
Ti So Ti Mi So
cWi iWi cWi iWi
ii.
PC2
PC1
12%
84%
8%
77%
14%
76%
11%
82%
iii.
log2FC
log2(baseMean)
Pass
Fail
iv.
Wald statistic
log2FC
v.
Z-score scaled expression

and showed little modulation in common with any of the three other species (Fig 3.6.B, right). In the marmoset, rat, and mouse, we found bands of strongly depleted genes and a weaker distribution of enriched genes.

To subsequently characterize these genes, we performed a fast gene set expression analysis (FGSEA) to find biologically relevant sets of genes as defined through gene ontologies (Sergushichev 2016). This enabled us to look at the gene expression data in terms of ranked statistics of gene sets with defined functional pathways. Our first pass of analysis revealed that the most significantly depleted gene sets across species were gene sets largely related to vascular support and angiogenesis. This provided a strong negative control as we know from our previous analyses that we successfully purified corticostriatial projection neurons. We then elected to screen only for enriched, conserved gene sets.

To do this, we filtered the FGSEA outputs per species and filtered them based only on the genes that were found to be orthologous across all four species. We used a strict criterion of eliminating any gene set that had any component leading gene that was not orthologous. We took the resulting gene ontologies and ranked their enrichment scores based on a relaxed p value of 0.01, multicomparison corrected. We then added the additional filter that we would only accept gene ontology sets that were significantly up or down regulated in at least two of our species and share an enrichment pattern (positive or negative) between the rodents to serve as an internal screening control while still allowing for the non-human primates to express similar or different patterns. After applying these filters, we were left with only a single gene ontology set that met all criteria. This gene ontology set was GO: 1902236 and was significantly enriched in both the marmoset and rat, showed a positive trend in the mouse, and demonstrated a non-significant depletion in the macaque (Fig. 3.6.C). Identified gene ontology set GO: 1902236 is associated with the negative regulation of endoplasmic reticulum (ER) stress-induced intrinsic apoptotic signaling (QuickGO::Term GO:1902236 n.d.). This single gene ontology set may serve as a unique genetic signature of this corticoaccumbal projection in mice, rat, and marmoset.

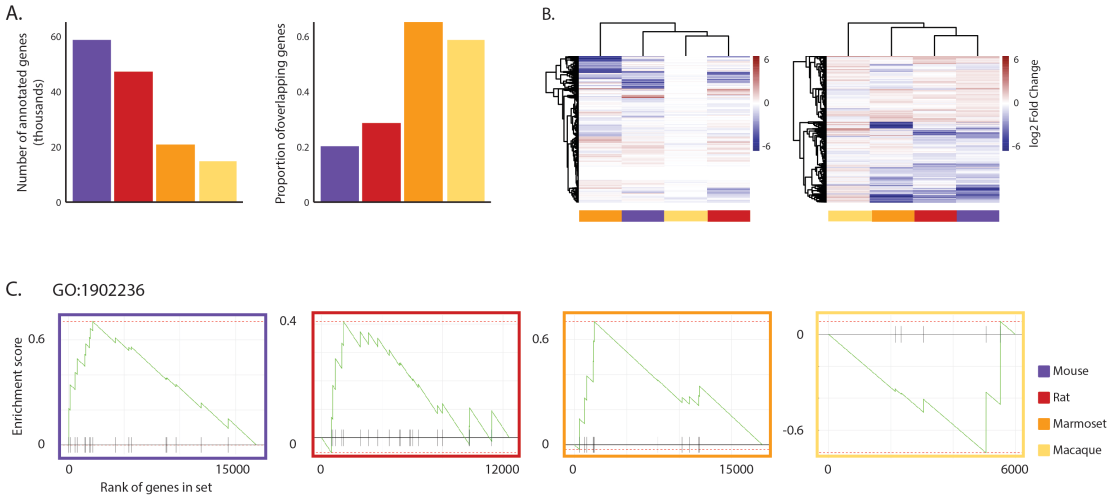

Figure 3.6 Conserved orthologs across species reveal a common gene ontology set of genes related to endoplasmic reticulum stress response
A. Two descriptive measures of the number of annotated genes per species (left) and the proportion of the annotated genes demonstrating overlap (right). B. Orthologs were identified across all samples using curated phylogenetics analysis is ENSEMBL. Resulting orthologs are organized using hierarchical clustering and shown in heatmaps showing log2FoldChange for each ortholog in IP vs input samples for all orthologous genes (left) and genes that pass a cut-off of showing significant log2FoldChange (right). C. Enrichment plots of gene ontology set GO: 1902236 in the four species. The enrichment score is plotted on the y-axis against the rank of the genes within the set. The green line tracks the running-sum statistic of enrichment score per gene in the gene set. Each vertical line on the x-axis indicates each gene in the gene set. Genes overrepresented at the top of the ranked list of genes receive a more positive enrichment score and then continue down the list of genes with a running-sum statistic when a gene is present and decreases when the gene is not present. Genes more highly ranked also feature a heavier weighting due to their correlation with the phenotype.

3.6 Methods

3.6.1 Animals

All procedures involving animal models were approved by The Rockefeller University Institutional Animal Care and Use committee and were in accordance with guidelines established by the National Institutes of Health. All mice were C57Bl/6J wild type purchased from Jackson Laboratories. Sprague-Dawley rats were purchased from Charles River. Rodent cohorts used in this study were a combination of male and female littermates and were maintained on a 12 hr light-dark cycle. Mice (n=11) were sacrificed at 10-12 weeks of age, while rats (n=8) were sacrificed between 3 and 15 months. All rodents were sacrificed within the same circadian period (12:00 - 16:00). Marmoset (n=6) and macaque monkeys (n=2) were in normal health and were group housed with other conspecifics on a 12 hr light-dark cycle. Marmosets used were a combination of male (n=3) and female (n=3), while both macaques used were male. Marmosets were between 2.5 and 6 years of age. All marmosets used in polysome immunoprecipitations were euthanized between 20:00 and 24:00, while the histology marmosets were euthanized between 12:00 and 16:00. Both macaques were euthanized at 10 years of age at the same point in their circadian cycle (10:00 - 12:00).

3.6.2 Injection surgeries

Mice

Surgeries were performed on adult mice (7-10 weeks old) under ketamine/xylazine (100/10 mg/kg) anesthesia. Single unilateral stereotaxic injections of 0.30 μl AAVretro-EGFPL10a (1.03x10^13 gc/ml) at 0.1 ul/sec were done using the following injection coordinates: Mouse NAc shell, +0.45 mm ML, +1.54 mm AP from lambda, -3.78 mm DV from dura, injected at a 90° angle. Following injections, the needle was slowly retracted and skin was closed with Vetbond.

Rats

Surgeries were performed on adult rats (2 to 5 months old) under 1-2% isoflurane anesthesia. Single unilateral stereotaxic injections of 0.30 ul AAVretro-EGFPL10a (1.03x10^13 gc/ml) at 0.1 ul/sec were done using the following injection coordinates: Rat NAc shell, +0.70 mm ML, +2.20 mm AP from lambda, -3.80 mm DV from dura, injected at a 90° angle. Following injections, the needle was slowly retracted and skin was closed with Vetbond.

Marmosets

Marmoset surgeries were performed on adult animals (2.5 to 6 years old). Animals were induced with alfaxalone (5-12mg/kg IM) and midazolam (0.05 – 0.7mg/kg IM). They were subsequently intubated and ventilated with oxygen (30-100%). A surgical plane of anesthesia was maintained with a continuous rate infusion consisting of fentanyl (bolus: 5-10 ug/kg, CRI: 10-25 ug/kg/hour) and alfaxalone (bolus: 2-5 mg/kg, CRI: 0.1-0.2 mg/kg/min). Intravenous fluids were also provided at the discretion of veterinary services and the measured glucose level of the animal. Common intravenous fluids administered included isotonic saline, LRS, or normosol-R with 5% dextrose. Single unilateral stereotaxic injections of 1.0 ul AAVretro-EGFPL10a (1.03x10^13 gc/ml) at 50 nl/min were

done using the following injection coordinates: Marmoset NAc shell, +2.00 mm ML, +11.5 mm AP IA, -9.00 mm DV from dura, injected at a 90° angle. Injections were performed with a glass pipette pulled to a 15 um tip diameter with a 30° bevel (Sutter: B100-75-10 (1mm x 0.75mm ID x10cm) or WPI, 504949, 1.14mm, Nanoliter 2010, 504127) using a 10uL syringe (Hamilton, 7653-01) and a UMP3 UltraMicroPump (WPI, UMP3-3). Following injection, the pipette was slowly retracted and the craniotomy was filled with Kwik-Sil (WPI, Sarasota, FL) before the surgical site was closed with sutures. All animals received postoperative analgesia consisting of daily meloxicam (0.1-0.2mg/kg PO) and twice per day buprenorphine (0.005 to 0.03 mg/kg IM) for a minimum of 48 hours.

Macaques

Macaque surgeries were performed on adult animals (10 years old) under deep, general anesthesia. Animals were induced with a combination of detamine (~3-10 mg/kg IM) and dexdomitor (~0.001-0.02 mg/kg IM). Anesthesia was maintained with an IV continuous rate infusion (CRI) of Dexdomitor (0.001-0.02 mg/kg) and fentanyl (5-42 mcg/kg/hr). A combination of the following metrics were utilized for ongoing anesthetic monitoring: End Tidal CO2, rhythm (ECG), body temperature (rectal probe), SpO2, blood pressure, respiratory rate and effort, as well as response to withdrawal reflex. Two surgeries were required per animal. The first was the implantation of custom made fiducial makers to allow the utility of MRI guided stereotaxic surgical software (cortExplore, Linz, Austria). Due to the larger macaque brains varying in size on the order of a centimeter or more, stereotaxic coordinates are best utilized for superficial targets wherein additional visual makers such as sulci or sutures can provide additional cues to location or large subcortical structures that are larger than the variation in size of the animals. Given that the NAc is only 3-6mm in size, traditional stereotaxic surgical approaches were insufficient. As a result, we elected to design and implant custom fiducial markers lucent on both CT and MRI (Fig 3.7). 3D MRI and CT scans were acquired, coregistered, and loaded into cortExplore. This software then is volumetrically coregistered with real-time tracking of surgical tools such that you can reliably target sub-millimeter structures without relying on stereotaxic coordinates.

In the second surgery, single unilateral stereotaxic injections were done of 2.0 ul AAVrestro-EGFPL10a (1.03x10^13 gc/ml) at 50 nl/min. The NAc was targeted cortExplore (Fig 3.7E). The coordinates used in cortExplore space for the viral injection were as follows: x = 120mm, y = 137mm, z = 100mm, Trajectory length = 27.5227 mm. Injection was performed using a 26 gauge, 2 inch #2 bevel small hub needle (Hamilton, 7758-04), a 10uL syringe (Hamilton, 7653-01), and a UMP3 UltraMicroPump (WPI, UMP3-3). Following injection, the pipette was slowly retracted and the craniotomy was allowed to heal unobstructed. Sutures were used to reattach the muscles and close the surgical site. Both animals received postoperative analgesia consisting of daily meloxicam (0.1-0.2mg/kg PO) and twice per day buprenorphine (0.001- 0.03 mg/kg IM) for a minimum of 48 hours.

Figure 3.7 Targeting macaque nucleus accumbens
To target the NAc with MRI guided approaches, chronically implantable fiducial markers were created to provide signal on both CT and MRI images. A. MRI positive lucent seed (C4 Imaging, TX, USA) and CT lucent brass bearing (top). Custom designed, PEEK triangulation implant to fix orientation of fiducial markers for coregistration between imaging modalities (bottom). The brass balls are affixed in the vertices of the triangle and the seeds to the edges. The entire assembly is affixed to the skull of the animal through using a superficial skull screw. B. Example test image of 3D reconstructed CT scan (left) and 3D colorized MRI scan (right). Yellow arrows fiducial marker positions. C. Animal implanted with 9 fiducial markers as demonstrated on CT (left) and MRI (right). Yellow arrows indicate fiducial marker positions. D. Yellow circle highlights the desired target of the NAc on MRI with atlas overlays confirming location. E. Targeting the NAc through MRI guided stereotaxic surgical software, cortExplore. Yellow circle indicated NAc. Yellow arrows indicate coregistered overlay of fiducial markers. Panels indicate coronal, sagittal, and horizontal planes of view (left, center, right, respectively).

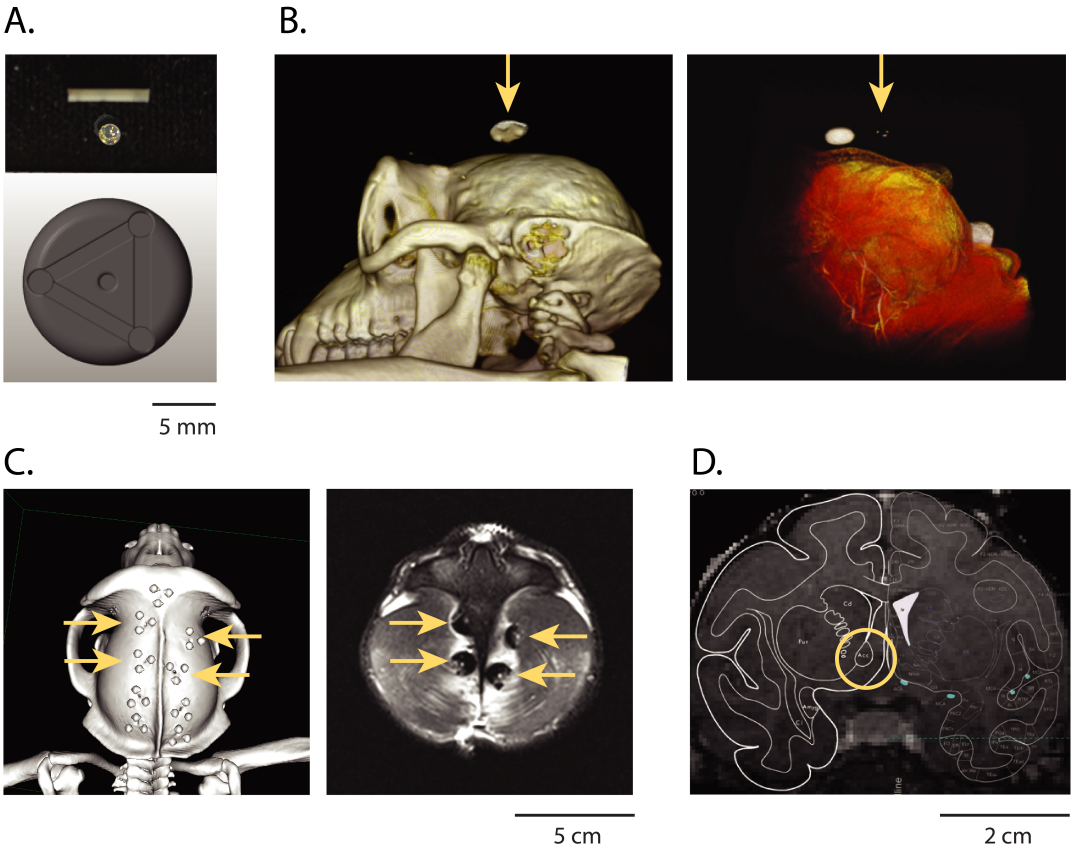
A.
B.
5 mm
C.
5 cm
D.
2 cm
E.

3.6.3 Tissue extraction

Rodents

3 to 4 weeks after surgery, mice and rats were deeply anesthetized with CO2 and sacrificed via live decapitation and tissue was collected for polysome immunoprecipitation or immunohistology. Manual dissection isolated the NAc and mPFC ipsilateral to the viral injection.

Marmosets

The anesthesia regimen for the marmoset dissection followed the same procedure as the injection surgery but was then transitioned onto a CRI of fentanyl (bolus: 5-10 ug/kg, CRI: 10-25 ug/kg/hour), cisatracurium (0.09-0.15 mg/kg IV, with a maintenance dose of 0.06-0.12 mg/kg/hour), and fluids in combination with nitrous oxide (1:1 to 7:3) in O2 (IH). This combination of anesthetics preserves neural function in a more natural state as measured electrophysiologically. Just before taking the biopsy, we reintroduced alfaxalone (bolus: 2-5 mg/kg, CRI: 0.1-0.2 mg/kg/min) to ensure a deep plane of anesthesia. A combination of the following metrics may be utilized for ongoing anesthetic monitoring: End Tidal CO2, rhythm (ECG), body temperature (rectal probe), SpO2, blood pressure, respiratory rate and effort, as well as response to withdrawal reflex. When administering cisatracurium EEG and train-of-four were also measured. A craniotomy and durotomy were made above the mPFC ipsilateral to the viral injection of the NAc. Intracranial tissue dissection for immunoprecipitation was performed via punch biopsy of the mPFC. During each procedure, two punch biopsies were taken. The medial biopsy was utilized for this project and the lateral biopsy was used in a parallel project. RNAse-free technique was maintained throughout the dissections in order to maximize the quality of the polysome immunoprecipitations. Marmosets used for polysome immunoprecipitations were euthanized after spending up to 72 hours under anesthesia as part of a parallel acute imaging experiment. Because of the limitations imposed by the surgical setup, the NAc was not collected in those animals for polysome immunoprecipitations; however, the subsequently fixed NAc was used for histology. To confirm localization of the biopsies, custom marmoset matrices were developed similar in design to those created by other groups (Dalgard et al. 2015; Guy et al. 2016). Here, we customized them to support the dorsal surface of the brain and hold the sample in the Frankfurt horizontal plane for direct of comparison to atlas sections (Fig 3.8.A).

Macaques

The anesthesia regimen for the macaque dissection followed the same procedure as the injection surgery. Once the animal had reached a deep plane of anesthesia, the head was fixed in a C-clamp arc (Rogue, Montreal, Canada, #6008201) which allowed the animal to be placed in a recumbent posture giving full dorsal access to the head. The skin and muscle were retracted to expose the fiducial markers, which were removed along with all other soft tissue on the surface of the skull. The dorsal cap of the skull was removed, exposing the brain surface. Sodium pentobarbital was administered (15-50 mg/kg IV) and was followed by a full cardiac perfusion with ice-cold heparinized PBS (10000 USP units per mL). The brain was then immediately removed from the skull and placed in a custom 3D

Figure 3.8 Custom non-human primate matrices
A. 3D design of custom made marmoset brain matrix with 2 mm slats for coronal sectioning and a single midline to bifurcate hemispheres (left). The brain is extracted (either after perfusion or fresh), placed ventral side up into the matrix cradle (right, top), surrounded with a molded agarose ring to provide lateral support to the tissue during slicing (right, middle), and then the individual slats can be released for additional processing of that specific slice (right, bottom, left). The resultant slices are compared against atlas references to confirm localization of tissue extracted (right, bottom, right). Atlas inset is taken from *Marmoset Gene Atlas* (Marmoset Gene Atlas n.d.). B. Same as A, but with notable design differences of 3 mm slats without bifurcation and the addition of joining rods with pin release to support the larger size of the brain. Atlas inset is taken from *A Combined MRI and Histology Atlas of the Rhesus Monkey Brain in Stereotaxic Coordinates* (Saleem and Logothetis 2012). Cd, caudate; dlPFC, dorsolateral prefrontal cortex; gr, gyrus rectus; mPFC, medial prefrontal cortex; OFC, orbitofrontal cortex; vlPFC, ventrolateral prefrontal cortex.

A. Marmoset

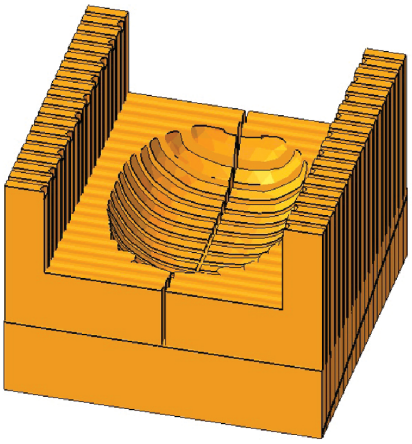

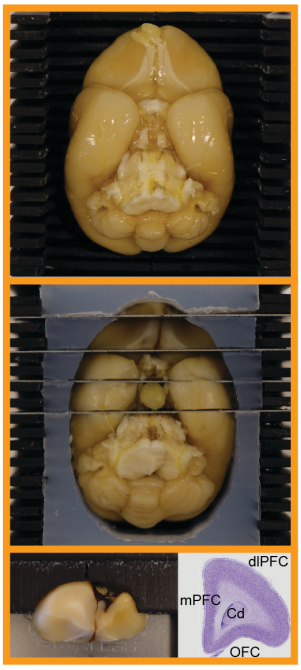

1 cm

B. Macaque

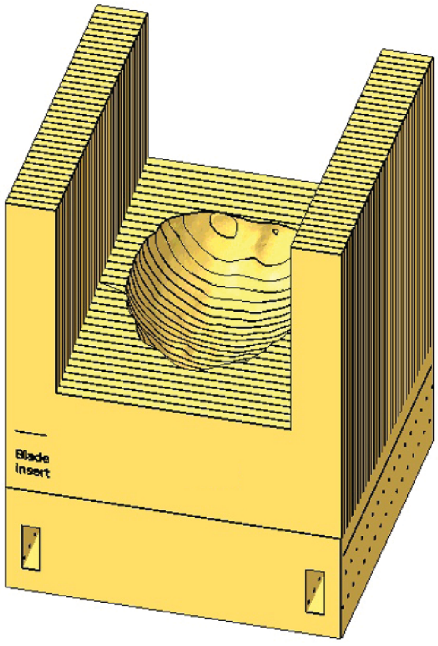

1 cm

printed brain matrix (Fig 3.8.B). A chilled 3% agarose support ring molded to the negative 3D reconstruction of the brain, was placed around the tissue to provide lateral support. Blades were then pushed down through the slits in the matrix, cutting the brain into coronal slices 3 mm thick. Due to the larger size of the matrix, the slats were assembled using rods traversing the entire matrix and released with individual pins. Upon finishing cutting each section of interest, the pins were released and each slice removed on the cutting blade. Manual dissection isolated the NAc and mPFC ipsilateral to the viral injection in subject St. Manual dissection isolated the NAc and mPFC ipsilateral and contralateral to the viral injection in subject Wi. In the dissection procedure of the second animal the contralateral NAc and mPFC were also dissected. All remaining tissue was flash-frozen using powdered dry ice and preserved for future experiments. RNAse-free technique was maintained throughout the dissections in order to maximize the quality of the polysome immunoprecipitations.

3.6.4 Immunohistochemistry

Mice, rats, and marmosets were deeply anesthetized and transcardially perfused with PBS followed by 4% paraformaldehyde in PBS. Brains were dissected and postfixed for 8-12 hours at 4°C, cryopreserved using a 30% sucrose solution, and sectioned on a freezing microtome (40 μm sections). Free-floating sections were immunofluorescently stained with mouse anti-NeuN (1:1000, Millipore, MA, USA, Cat# MAB377B) and chicken anti-GFP (1:2000, Abcam, MA, USA, Cat# ab13970) primary antibodies. Sections were blocked for 60 min in PBS containing 2.5% normal donkey serum (NDS) and 0.1% Triton-X-100 and then incubated at 4°C overnight with primary antibodies diluted in PBS containing 0.1% Triton-X-100 and 1% NDS. Sections were washed with PBS and incubated for one hour at room temperature with Alexa-fluor conjugated secondary antibodies (Life Technologies, MA, USA) diluted in PBS. All sections were imaged on a Zeiss LSM700 or LSM780 confocal microscope.

3.6.5 Translating Ribosome Affinity Purification

Affinity purification of EGFP-tagged polysomes was carried out as previously described (Heiman et al. 2014). IPs were done 3-4 weeks after viral injections in the case of mice, rats, and marmoset monkeys. Macaque IPs were conducted eight months after viral injection to account for the known pace of viral transduction in macaque monkeys. In mice, the three biological replicates consisted of brain tissue pooled from 3 animals (male and female). The four rat replicates consisted of brain tissue pooled from 2 rats each (male and female), while the four marmoset and two macaque replicates each contained brain tissue from just one animal. Dissection of brain tissue occurred in ice-cold HBSS containing 35 mM glucose, 4 mM NaHCO3, 2.5 mM HEPES-KOH (pH 7.4), and 100 μg/ml cycloheximide. Tissue containing specified brain regions was then homogenized in homogenization buffer containing 10 mM HEPES-KOH (pH 7.4), 150 mM KCl, 5 mM MgCl2, 0.5 mM DTT, 100 μg/ml cycloheximide, RNasin (Promega, Madison, WI) and SUPERas-InTM (Life Technologies) RNase inhibitors, and Complete-EDTA-free protease inhibitors (Roche), and then cleared by centrifugation at 2000 x g. IGEPAL CA630 (NP-40, Sigma) and DHPC (Avanti Polar Lipids, AL, USA) were both added to the S2 supernatant to a final

concentration of 1% for each, followed by centrifugation at 20,000 x g. Polysomes were immunoprecipitated from the S20 supernatant using 100 μg of monoclonal anti-EGFP antibodies (50 μg each of clones 19C8 and 19F7; see Heiman et al., 2008) bound to biotinylated-Protein L (Pierce, Thermo Fisher, MA, USA) coated streptavidin-conjugated magnetic beads (Life Technologies), and washed in high salt buffer containing 10 mM HEPES-KOH (pH7.4), 350 mM KCl, 5 mM MgCl2, 1% IGEPAL CA-630, 0.5 mM DTT, 100 μg/ml cycloheximide, and RNasin RNase inhibitors (Promega). IPs were rotated overnight at 4°C. Bound RNA was purified using the RNeasy Plus Micro kit (Qiagen, MD, USA). A saved fraction of the pre-IP S20 supernatant RNA was also purified to serve as whole-tissue "input" samples. RNA quantity was measured with a Nanodrop 1000 spectrophotometer and quality was assayed on an Agilent 4200 Tapestation. Successful samples were used for qPCR and RNA-Seq analyses.

3.6.6 qPCR and RNA sequencing

qPCR was performed on a Roche Lightcycler 480 using Taqman assays and following standard cycling conditions (50°C for 2 min, 95°C for 10 min, then 40 cycles of 95°C for 15 s and 60°C for 1 min). 1 ng of cDNA from the RNA-seq libraries was used for each qPCR reaction and technical triplicates were run for each biological replicate for each condition. The mean CT for technical replicates was used for quantification. Data are normalized to *Actb* by the comparative CT (2-ΔΔCT) method (Livak and Schmittgen 2001) and presented as mean ± SEM of biological triplicates. For all viable samples across each of the four model organisms, 15 ng of total RNA was amplified using the Ovation RNA-Seq System V2 Kit (NuGEN, CA, USA) and RNA-seq libraries were prepared from 10 μg amplified RNA using the TruSeq RNA Sample Preparation Kit v2 (Illumina, CA, USA) following kit protocols. Sequencing reactions (75bp, paired end) were done using the Illumina NextSeq 2500 platform with 10-12 samples multiplexed per sequencing lane.

3.6.7 Bioinformatics and analysis

All analyses on the RNA sequencing data were conducted in R (R-Foundation, Vienna Austria) in concert with The Rockefeller University Bioinformatics Research Core and were conducted using the following Bioconductor packages: DESeq2 normalization method (v1.20.0), Biobase (v2.40.0), fgsea (v1.8.0), GSEABase (v1.42.0), biomaRt (v2.42.1), AnnotationDbi (v1.48.0). FGSEA analysis was conducted to identify biological gene sets that were enriched or depleted within each animal (Sergushichev 2016). Orthologs across animals were determined using curated phylogenitcs analysis in ENSEMBL (Vilella et al. 2009). Across all analyses, the base value of comparison is the log2 fold change of TRAP IP over input samples and p-values for significance testing are multicomparison corrected using Benjamini Hochberg FDR test. Heatmaps in the from the differential analysis results are expressed as gene z-score to reveal patterns in gene expression. We used a cut-off of $p < 0.05$ for all analyses except for the final comparison of conserved gene sets for which we used a cut-off of $p< 0.1$. Final filtering of conserved orthologs expressed in gene sets were done with custom written MATLAB (MathWorks, MA, USA) scripts.

CHAPTER 4. Serial ultrasound atlas of the common marmoset reveals basis of developmental delay and an interventional opportunity

‡Portions of the work in this chapter were accomplished with co-first author, Rohan Soman of the in-preparation manuscript resulting from this work. All data were collected together. MF performed Carnegie Staging analyses; RS performed linear regressions of embryonic and fetal measures.

4.1 Historical context of Carnegie Staging and common marmoset development

The common marmoset (*Callithrix jacchus*) provides an ideal model for primate studies. At a systems level, they provide a unique platform for neuroscience and behavioral studies shedding light on to mechanisms of cognition (Miller 2017; Miller et al. 2016a). From a developmental biology perspective, they provide the only system to study early primate embryogenesis, *in vivo*, a prospect that is ethically impossible to contemplate in humans, even if it were to be technically feasible (Chambers and Hearn 1985; Hearn et al. 1978; Kropp, Di Marzo, and Golos 2017; National Academies of Sciences, Anestidou, and Johnson 2019). Recent advances at the tissue and cellular level, including self-organizing stem cells into embryoids and organoids, combined with the advanced molecular tools of genome editing and transgenic technologies will illuminate the primate-specific aspects of embryonic development. With a gestation period of 140-150 days most often producing dizygotic twins, it possesses numerous benefits for developmental studies and creating transgenic primates (Park et al. 2016; Park and Silva 2019; Sasaki 2015; Schiel and Souto 2017; Tomioka et al. 2017). There is an essential need to establish an accessible and scalable means by which to monitor embryonic and fetal development with demonstrated correlates to *ex vivo* references.

Previous studies have demonstrated organ development and fetal growth curves utilizing ultrasound (Jaquish et al. 1995; Tardif et al. 1998). They formed the foundational basis by which marmoset development could be tracked utilizing ultrasound, but they lacked the temporal resolution to capture all stages of development and thereby are limited in scope for examining particularly early developmental signatures. *Ex vivo* histological studies (Enders and Lopata 1999; Moore, Gems, and Hearn 1985; Phillips 1976; Smith, Moore, and Hearn 1987) have created the standard by which marmoset embryos can be staged into Carnegie Stages, classic reference markers for embryological development (O'Rahilly, Müller, and Streeter 1987). However, these lack a critical link to *in vivo* monitoring of the embryos at the same stages. There have been efforts to use ultrasound to identify Carnegie Stages in human embryos (Blaas 1999; Dickey and Gasser 1993; Harkness, Rodger, and Baird 1996; Verwoerd-Dikkeboom et al. 2008), with some even providing direct comparison to retrieved embryos demonstrating staging correspondence, but it has not been explored in the marmoset.

These *ex vivo* studies revealed a remarkable finding that marmoset embryos enter into a period of delayed development just after implantation and prior to gastrulation. Although, it is debated whether or not this constitutes a form of primate diapause, a state of either facultative or obligate embryonic suspension

at the blastocyst stage (Deng et al. 2018; Phillips 1976; Renfree and Fenelon 2017). Marmosets do not show evidence of instantiating any delay in their pregnancies based on season, resource availability, or hormonal state (Phillips 1976), but nevertheless, the embryos exhibit marked delay in progressing through the stages of embryonic development compared to all other mammals for which this has been measured (Hill 2020). Still, prior studies have been unable to temporally resolve the earliest stages of embryonic development in detail.

Specific organogenesis has been tracked grossly by *ex vivo* studies that measured the presence and weight of organs across development, but this offers little structural insight (Chambers and Hearn 1985). Other studies have focused on development of individual organs, such as the brain, and have been able to detail development both *in vivo* and *ex vivo* utilizing magnetic resonance imaging (MRI) (Hikishima et al. 2013; Sawada et al. 2014). This imaging method requires a significant investment in custom and costly equipment thereby making it infeasible to scale across marmoset colonies as a means by which each individual fetus can be screened and tracked for key developmental milestones. Further, although the spatial resolution in these MRI studies proved to be exquisite, temporal resolution and movement artifact limits the measure of functions such as the heart beat or blood flow which provide key markers of cardiac development. There exists an opportunity to better match standard human measures for key organ development including kidney, heart, and brain (R. H. Anderson et al. 2003; Moorman et al. 2003; Sousa et al. 2017; van Vuuren et al. 2012)

Here we present a high resolution, serial ultrasound atlas for embryonic and fetal marmoset development, that verifies ultrasound as an accessible technique, reveals insights into the period of delayed development as well key features of organogenesis, and offers functionality to be queried by individuals to stage their own marmoset ultrasound images.

4.2 Serial scans reveal early embryonic development with protracted gastrulation

Prior to this study, the initial insights into the earliest stages of marmoset development were accessible only with *ex vivo* histological studies (Moore, Gems, and Hearn 1985; Phillips 1976; Smith, Moore, and Hearn 1987). These studies revealed an intriguing developmental delay which was further confirmed with later stage ultrasound imaging (Jaquish et al. 1995). Utilizing the standard of Carnegie Stages as a common reference, it was noted that marmoset embryos take many more days to progress through the earliest stages (Jaquish et al. 1995; Phillips 1976) Their observed measurements started later in pregnancy on days 33 and 24, respectively. The cause for this delay remains unknown. It was previously hypothesized that this delayed development in the common marmoset could not be termed diapause due to the lack of delay dependence on neither seasonal nor lactational quiescence as is evident in most other mammals that exhibit diapause (Renfree and Fenelon 2017). It was instead suggested that the delay was simply a matter of slower growth as a result metabolic demand for the twinned blastocysts to develop a fused chorion (Phillips 1976).

In this study, we were able to capture our earliest measures at estimated day 12 post fertilization. Pooling scans across all of our subjects, we were able to capture 89% of the days covering embryonic debelopment. Using this serial, high resolution imaging, we were able to stage the ultrasounds using the Carnegie Staging method bridging the gap between histological and ultrasound measurements (Fig 4.1). In order to identify the exact stage in which a period of protracted growth causes a developmental delay in marmosets compared to humans, we plotted the first day during which each Carnegie Stage was entered in Fig 4.1.A. Given that marmoset gestation is approximately half that of human gestation, we would have expected marmosets to enter each stage of embryonic development earlier than humans. Instead, not only was there a marked delay, but it only occurred during one distinct stage. We then plotted the percentage of embryonic development spent in each stage (Fig 4.1.B). This revealed only a single stage, Stage VII, in which significantly more time was spent for marmoset development than human development as measured by a two-proportion z-test ($p = 0.0038$). Fig 4.1.C depicts representative features used to classify each of the 23 Carnegie Stages. Individual ultrasounds for every day captured of embryonic development can be found in Figs 4.2 and 4.3.

To further interrogate the patterns of marmoset early embryonic growth and development, measurements of the embryonic disk (which correspond to the crown-rump length (CRL) after day 50) and biparietal distance were first taken across all 35 fetuses (Fig 4.3.B). The initial segment in Fig 4.4.B revealed a period in which the CRL changes little over nearly a 40-day period, after which a rapid period of growth begins close to the first discernable heartbeat, at day 57 (Fig 4.4.A). However, when individual ultrasound scans were examined, it is clear that the embryos and uterus are not in a quiescent state even during these first 40 days, as evidenced by the dramatic extraembryonic growth and restructuring taking place during this time. Measures of maximum chorionic cavity cross-sectional area and yolk sac diameter were taken during days 14-62 (Figs 4.4.C and 4.4.D), confirming extraembryonic growth and development. Diapause is strictly defined as a quiescent period of no growth. This period can therefore not be considered diapause given the dramatic restructuring of the amnion. Shown in Fig 4.4.B are the outlines of the lumen, embryo, yolk sac, amnion. The original ultrasounds from which these outlines were taken can be found in Fig 4.2.

We next sought to determine which of these standard measures, if any, are reliable predictors of the day of fertilization. Data from each measure were fit to a polynomial linear regression (Fig 4.5.A). All measures proved useful predictors with 95% confidence intervals of approximately 10 days, with chorionic cavity area as the best predictor of early embryonic age (days 13-53) and BPD the best overall predictor (days 87-birth) (Fig 4.5.B). Previous studies suggest that BPD measurements diverge as an indicator of postnatal survival (Tardif et al. 1998). We see no such separation within our BPD measures. In fact, due to the lower variance of measures of BPD (Jaquish et al. 1995), we find them to be a better predictor of gestational age and due date.

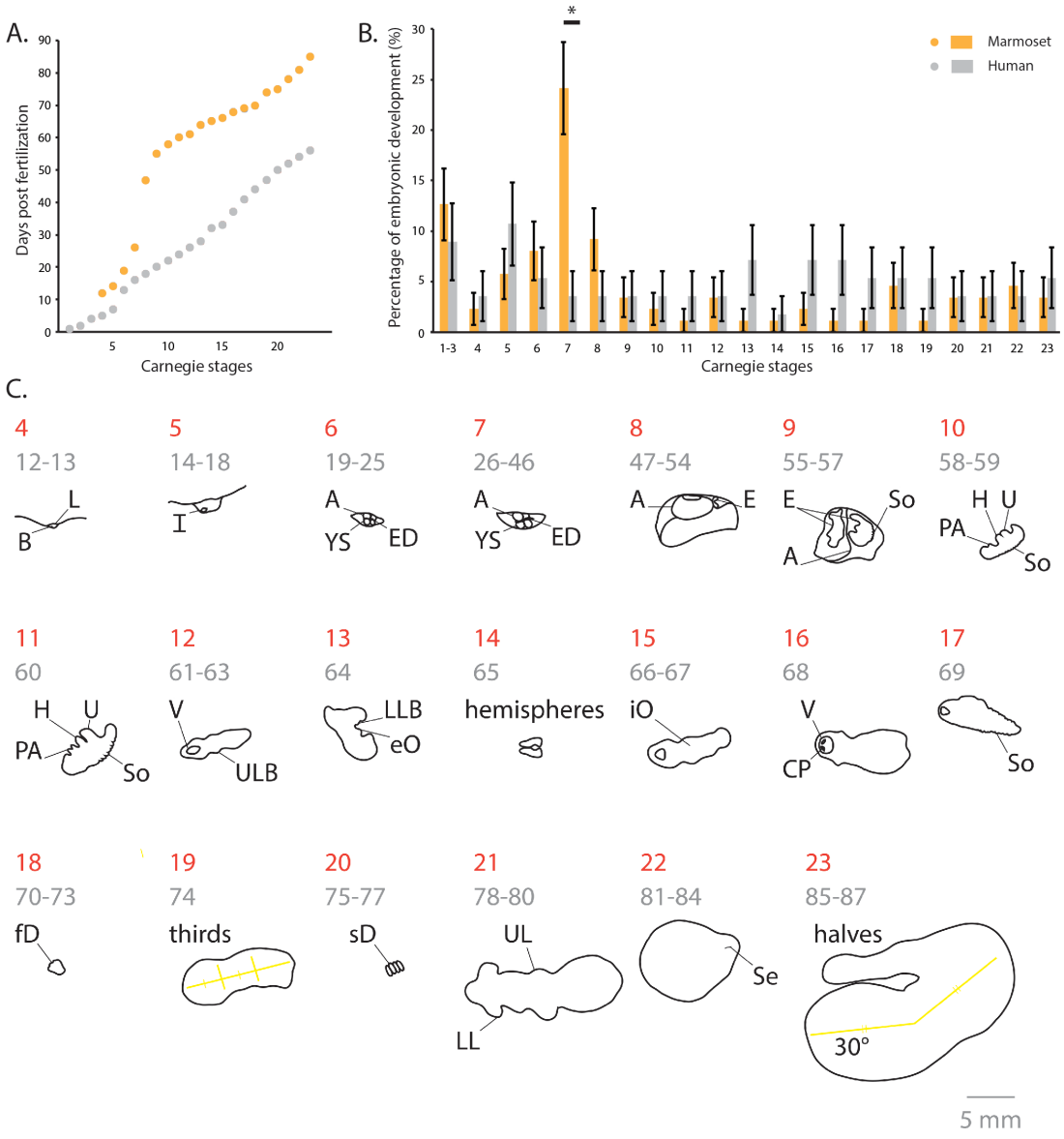

Figure 4.1. Early ultrasound measurements reveal Carnegie Stages
A. The first day post fertilization during which the developing embryo enters into each Carnegie Stage (orange, marmoset; gray, human). B. The percentage of the embryonic development (estimated to be 87 days marmoset, 56 days human) spent in each Carnegie Stage. C. Representative ultrasound images taken for each Carnegie Stage. Outlines in black reveal staging features relevant in ultrasounds. Yellow highlights key areas or orientations in figures. Red numbers indicate Carnegie Stage. Gray numbers indicate range of days per stage. A, amnion; B, blastocyst; CP, choroid plexus; E, embryo; eO, external organs; ED, embryonic disk; fD, fused digits; H, heart; I, implantation; iO, internal organs; L, lumen; LL, lower limb; LLB, lower limb bud; PA, pharyngeal arches; sD, separated digits; Se, septum; So, somites; U, umbilicus; UL, upper limb; ULB, upper limb bud; V, ventricle; YS, yolk sac.

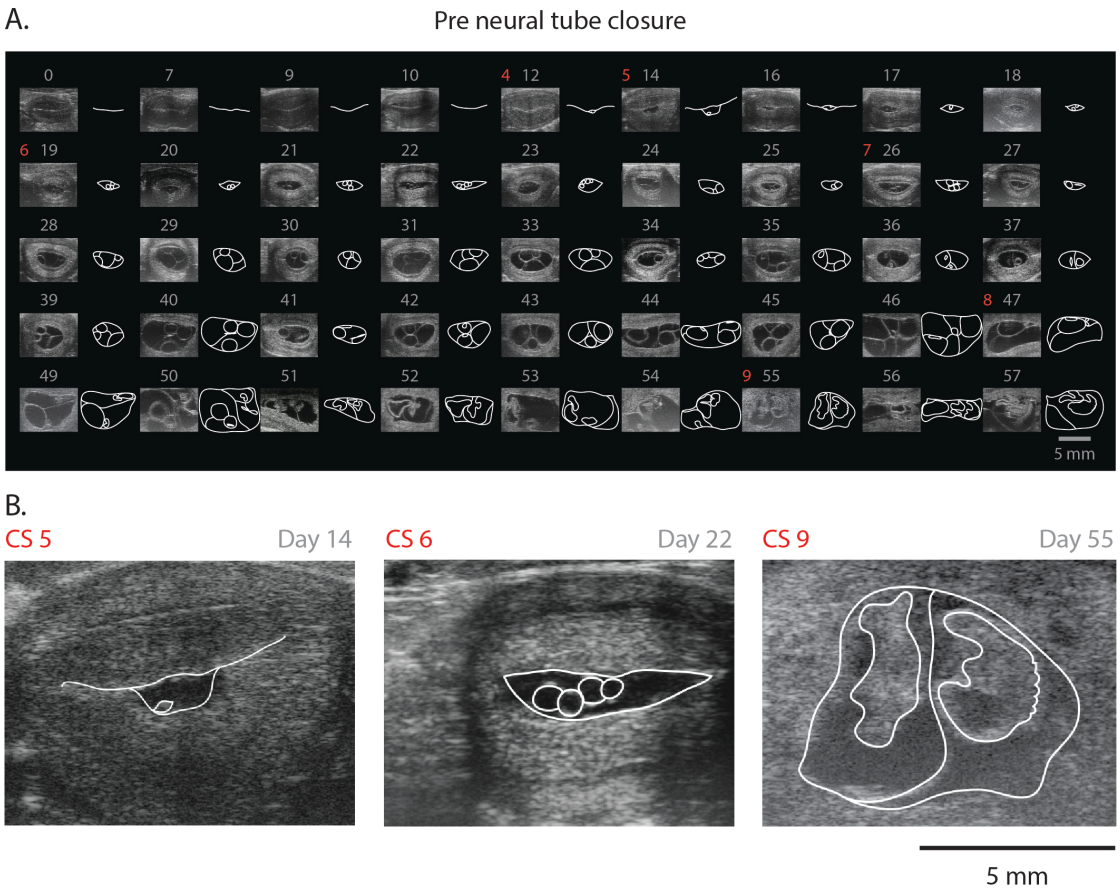

Figure 4.2. Daily ultrasound images with key features, pre neural tube closure Carnegie Stages preceding the closure of the neural tube. Outlines in white reveal the key features for staging. Yellow highlights key areas or orientations in figures. Red numbers indicate Carnegie Stage. Gray numbers indicate the estimated day post fertilization of the image. A. Individual ultrasound images taken from all days sampled for these stages. B. Selected days expanded to show detail.

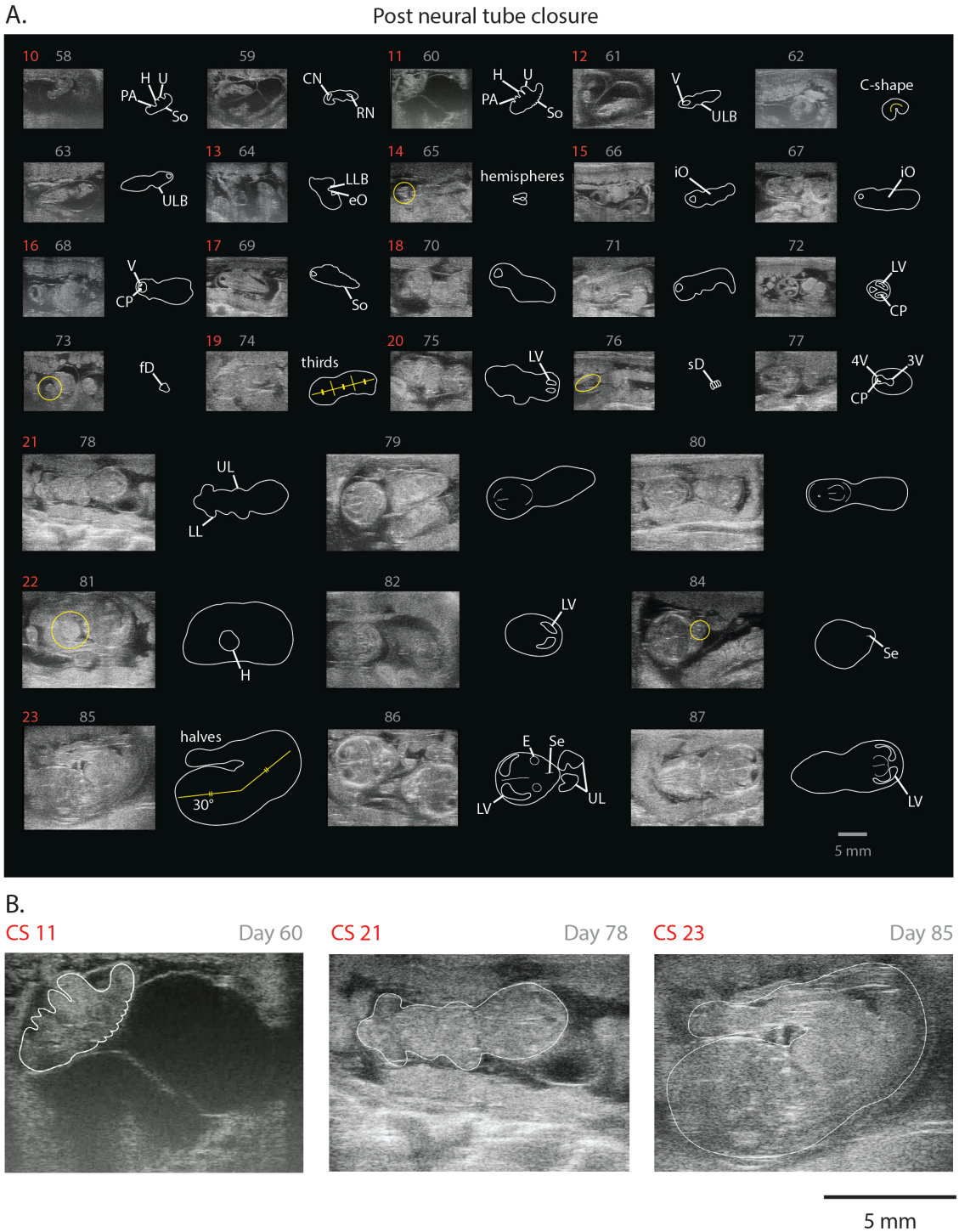

Figure 4.3 Daily ultrasound images with key features, post neural tube closure Carnegie Stages after the closure of the neural tube. Conventions follow Fig 4.2. A. Individual ultrasound images taken from all days sampled for these stages. B. Selected days expanded to show detail. CP, choroid plexus; E, eye; eO, external organs; fD, fused digits; H, heart; iO, internal organs; LL, lower limb; LLB, lower limb bud; PA, pharyngeal arches; sD, separated digits; Se, septum; So, somites; U, umbilicus; UL, upper limb; ULB, upper limb bud; V, ventricle.

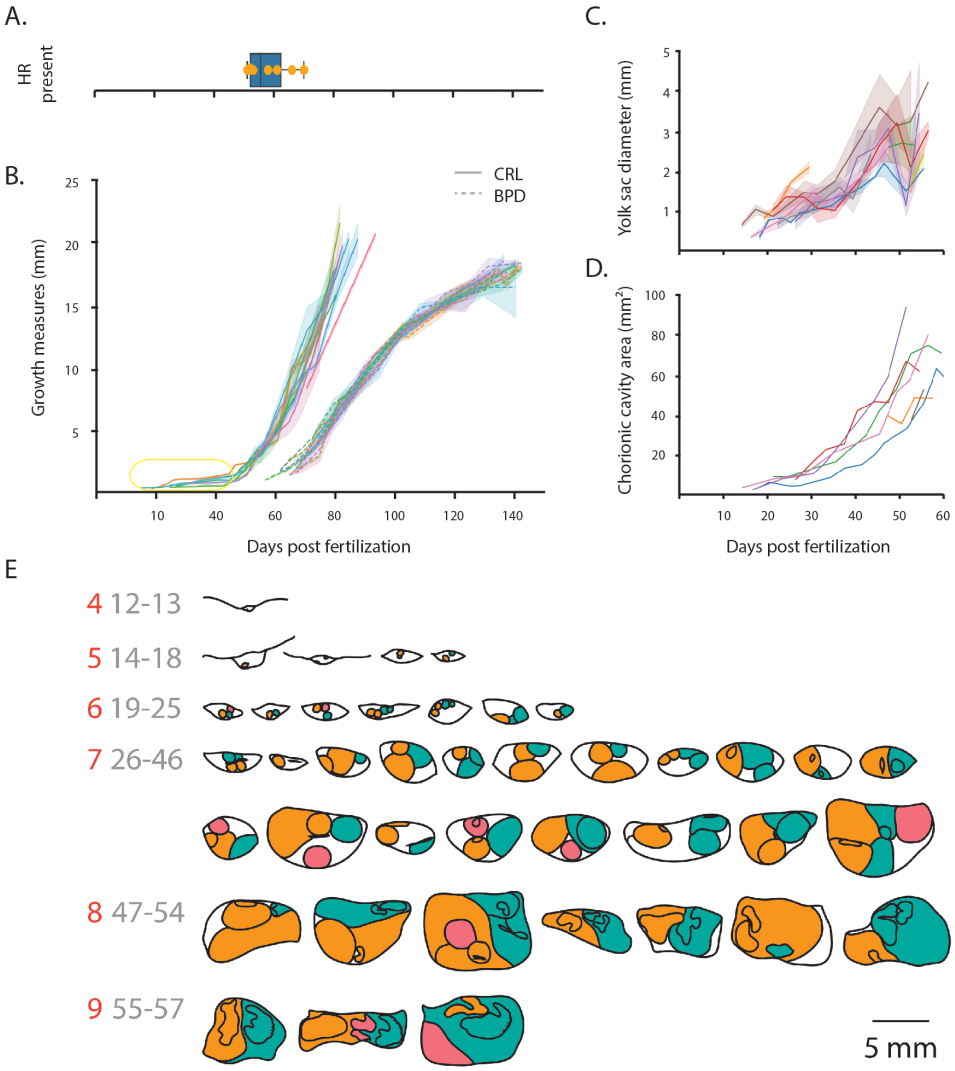

Figure 4.4 High resolution, serial ultrasounds reveal period of protracted embryonic development distinct from diapause during gastrulation
A. First measurable heart rates in embryos across seven pregnancies (mean =day 57, 95% CI = day 52-64). B. Classical clinical embryonic measurements for crown-rump length (CRL) from day 14-93 and biparietal distance (BPD) from 87 days to birth. Measurements are taken across all embryos during 7 pregnancies. Each colored line corresponds to one course of pregnancy; the width of shading represents the 95% confidence interval for each embryo in the pregnancy. Inset shows range of values for C, D. C. Yolk sac diameter measured from day 13-53 days before birth. D. Maximum chorionic cavity area was calculated from 13-53 days before birth as a correlate of chorionic volume. E. Relevant outlines of serial ultrasounds across all pregnancies to maximize coverage. Red numbers indicate Carnegie Stage. Gray numbers indicate range of approximate days post fertilization. Each embryo individual embryo and its respective structures are shaded in green, orange, and pink.

A.

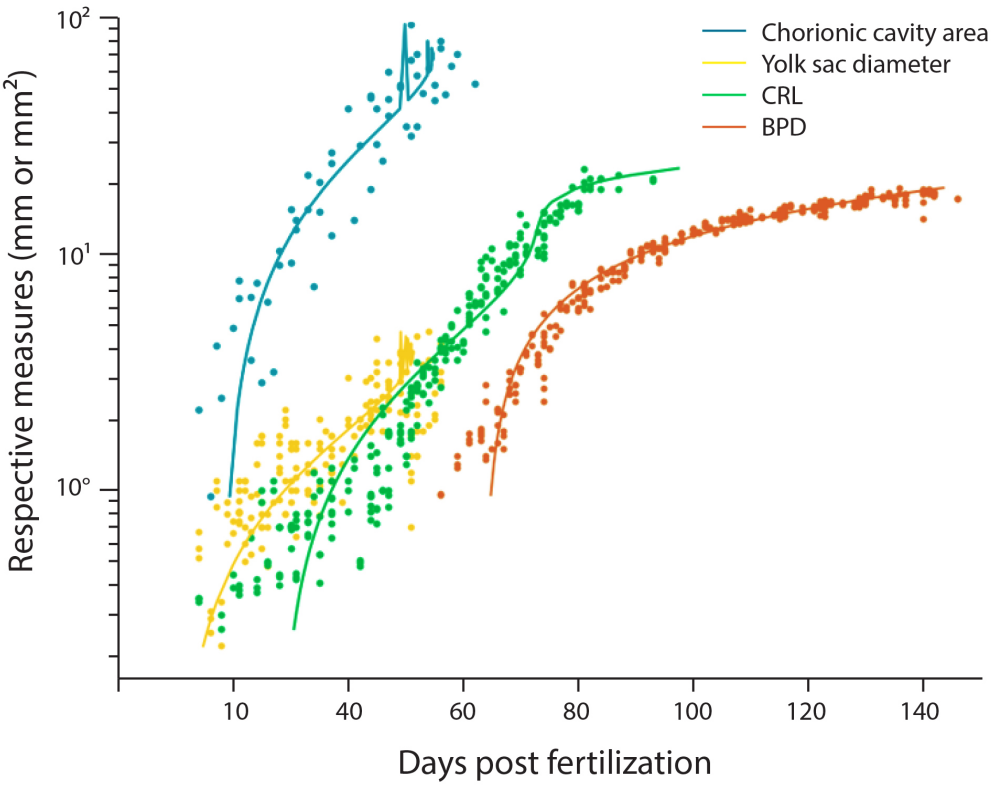

B.

Measure	R^2	95% CI (days)	Best Fit Curve
Chorionic Cavity Area	0.88	9.0	$y = -125 + 1.06x - 0.008x^2$
Yolk Sac Diameter	0.65	13.8	$y = -133 + 21.6x - 2.83x^2$
Crown-Rump Length	0.90	10.8	$y = -115 + 9.72x - 0.728x^2 + 0.019x^3$
Biparietal Distance	0.97	8.4	$y = -79.4 + 1.18x - 0.157x^2$

Figure 4.5 Embryonic and fetal measures as predictors of days post fertilization A. Linear regressions based upon each of CCA, YSD, CRL, BPD as individual predictors of fertilization age. Dots represent each measurement aggregated from collected data, and lines trace the curve of best fit. B. Model description and statistics for linear regression model performance for each measure.

4.3 Fetal organogenesis milestones visible on ultrasound

Throughout this ultrasound atlas, we identified key stages of organogenesis that may be of particular interest in tracking normal development of organ systems. This is of importance when creating transgenic animals such that you need to track both the expected and unexpected results of the phenotype, particularly in light of the fact that single mutations can have wide ranging effects across systems (Bakrania et al. 2008). A recent study has established an MRI fetal atlas for the common marmoset and demonstrate approximately similar findings between *ex vivo* and *in utero* MRI images (Hikishima et al. 2013). This work lays the foundation for the level of detail that can be achieved not only at resolution but with different scanning sequences. Nevertheless, for individuals in need of tracking development of their common marmoset fetuses but without access to the specialized equipment needed for *in utero* MRI, we demonstrated here that key findings can be appreciated on ultrasound. Thus, used in concert with the MRI atlas, it is possible to achieve a much more comprehensive and accessible understanding. Further, it is possible to use real time ultrasound with reference MRI atlas images to facilitate procedures that must be done *in utero*. Fig 4.6.A reveals the development of cortical layers through indirect cues. We found enlarged lateral ventricles and a thin cortical mantle that gradually get smaller and larger, respectively, as the ventricular zone gives rise to the progenitor cells which differentiate into the layered cortex. These findings are also demonstrated in the Hikishima et al., 2013 study confirming that we are not observing an artifact of a distorted image when seeing these enlarged ventricles. In fact, this layer development can be appreciated with the widely accessible ultrasound technique.

In regards to other organ systems, one of the first signs of a viable fetus is the presence of a heart tube that then allows flow of blood through the cardiovascular system as seen on Doppler and through measuring the fetal heartbeat. Fig 4.6.B shows the different stages of heart development and the first point at which we were able to observe a heart beat in the marmoset fetus, at day 57 ($\pm$3.8). Finally Fig 4.6.C reveals a surprising insight into adrenal and kidney development in the common marmoset. Whereas the fetal adrenal:kidney length ratio is approximately 2:7 in humans (van Vuuren et al. 2012) and is consistent throughout gestation, the comparable marmoset ratio was approximately 1:1. This is shifted dramatically later in life as was shown in the inset picturing a freshly dissected adult kidney next to a freshly dissected infant kidney taken on postnatal day 0.

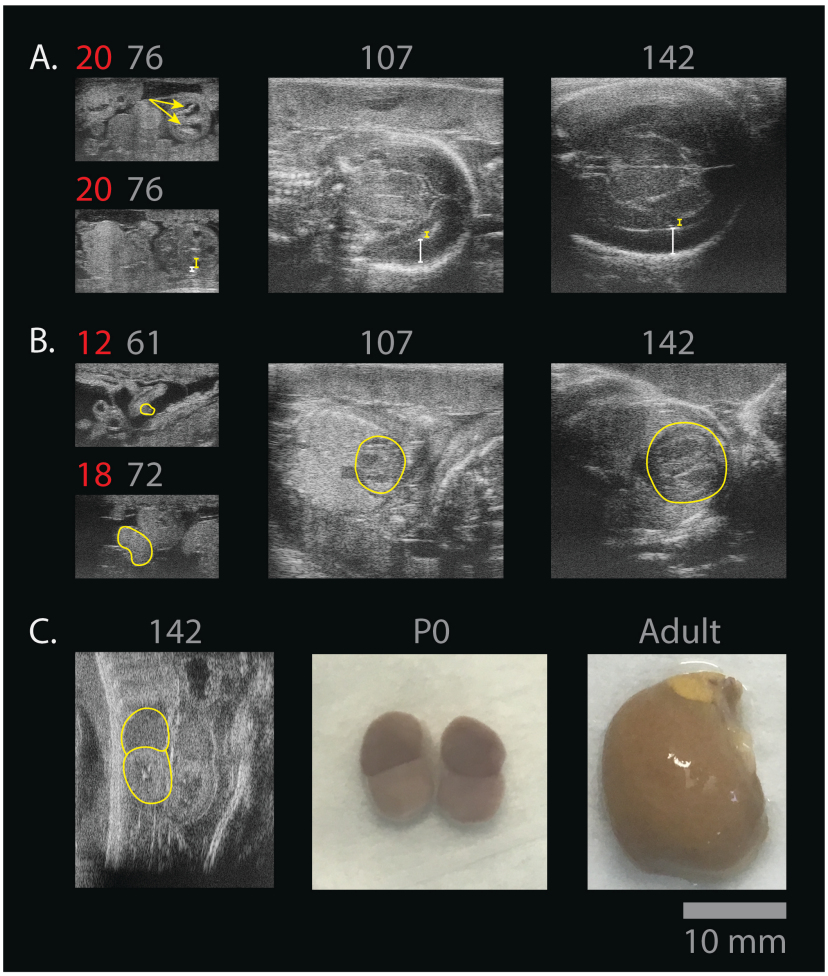

Figure 4.6 Organogenesis milestones tracked with ultrasound
A. Choroid plexus distinct within lateral ventricles as denoted by arrows. Large lateral ventricles (yellow bars) that gradually reduce in size as the cortical thickness increases over time (white bars). C. Development of the heart tube with subsequent inclusion into the thoracic cavity and development of distinct chambers. Yellow outlines indicate regions of heart development. D. (i) Adrenal to kidney ratio on ultrasound reveals ratio of 1:1 shown to be accurate with (ii) *ex vivo* gross dissection. (iii) This ratio dramatically decreases as the kidneys and adrenals mature. All red text indicates Carnegie Stage for images still classified as embryos. All gray text indicates days post fertilization except for P0 which is day of birth and Adult.

4.4 Methods

4.4.1 Animals

All animals were in normal health and were group housed with other conspecifics at the facility. All procedures were approved by The Rockefeller University Animal Care and Use Committee and were performed in accordance with the National Institute of Health guidelines for care and use of laboratory animals. The gross dissection of the ex vivo kidneys were conducted on kidneys taken from a pup that did not survive the birthing process and from an adult that was humanely euthanized for the project described in Chapter 2.

4.4.2 Ultrasound imaging of animals

We performed ultrasound measurements on 7 dams across 13 pregnancies totaling 34 fetuses. Each marmoset was kept in stable, bonded pairs on luetolytic cloprostenol (0.03 mL, 1x/28 days) until entering breeding. Upon commencing breeding, each marmoset was palpated weekly or by ultrasound exam if pregnancy was suspected. Once an open lumen in the uterus was observed, the dam underwent biweekly ultrasound examinations using the Vevo 2100 (FUJIFILM VisualSonics, Ontario, Canada) ultrasound. Probes used included MS700, MS550D, and MS250. Using these three probes, we are able to obtain a range of pixel sizes from 0.01 – 0.04 mm that covered fields of view from 1 – 2 cm wide. For the last half of pregnancy, ultrasounds were conducted on a weekly basis. Ultrasounds were conducted without sedation. Animals were behaviorally trained with positive reinforcement to remain still while being lightly held in a recumbent position.

4.4.3 Ultrasound analysis

An independent scorer who did not partake in the ultrasound examination took key measurements of crown-rump length and parietal distance for each fetus. Notes were made on stages of organogenesis. Across all animals in the study, there were 104 imaging days consisting of 289 individual ultrasound exams with a total of 6159 recordings. All recordings were exported as dicoms and converted into TIFF stacks using custom MATLAB code (MathWorks, MA, USA). Measurements were made in ImageJ (NIH, MD, USA) and notes were taken in Excel (Microsoft, WA, USA). Data were collected and analyzed in Python (Python Software Foundation, DE, USA) and comparison charts based on notes were made in Excel.

To calculate day post fertilization, we took each animal's date of birth and assumed a gestation period of 143 days (Jaquish et al. 1995). The day of each of ultrasound exam was then converted into a presumed date from fertilization. We plotted all data both in time from birth and presumed day post fertilization. For ease of comparison to other studies, all figures here are plotted only in day post fertilization.

CHAPTER 5. Discussion and conclusion

Throughout these experiments we have demonstrated three critical aspects of interrogating the social brain in the marmoset. In Chapter 2, we demonstrated the functional architecture supporting the representation of natural scenes in V2, which overlaps with face patch "O." We further established a method by which it will be possible to characterize the cell type specificity of this inherent map. In Chapter 3, we identified the genetic signature for the corticoaccumbal projection from mPFC to the NAc across marmoset, rat, and mouse. This conserved signature is a gene ontology set related to stress regulation. Finally, in chapter 3, we created a comprehensive, high resolution, serial ultrasound atlas detailing embryonic and fetal development of the marmoset. This atlas revealed the precise timing of the uniquely protracted stage of gastrulation, unique to the common marmoset. As this stage occurs before closure of the neural tube, it offers an opportunity to introduce genetic manipulations to the developing embryo *in utero*, creating a transgenic model in an otherwise wildtype animal.

Each line of inquiry poses multiple interpretations and raises exciting new propositions for the mechanisms underlying the social brain.

5.1 Reflections on functional architecture of naturalistic stimuli in V2 and "O"

What does the functional architecture underlying naturalistic stimuli processing in V2 mean for face patch "O?" Our findings here suggest that rather than "O" being comprised of a population of neurons selective only to faces, it is instead a part of a larger architecture supporting naturalistic stimuli. One limitation of this study is that we localize "O" only within the implanted window. It is possible that in the two animals studied in this experiment that "O" could have been localized more laterally or more anteriorly compared to the animals from which the coordinates were calculated. If this is the case, we can still be confident in our novel finding of a functional architecture for naturalistic stimuli located in V2.

However, the data more strongly support the interesting conclusion that face patch "O" is simply not a typical face patch. Instead, it is an area of V2 that may support recurrent activity that can receive modulation that may enhance particular representations of naturalistic stimuli. There are a few pieces of evidence supporting this from the Hung et al., 2015 paper discovering "O", from face patch literature, and from the data presented in this study.

Two key pieces of evidence from the Hung et al. 2015 paper support this. First, in analyzing the time course of percent signal change in marmoset face patch "O" as measured by fMRI, a canonically slow, it takes over 6 seconds to reach peak activation in this area and at this point faces, objects, and bodies are indistinguishable. It is only after 8 seconds that the activity for faces continues and maintains activity levels whereas the activity for objects and bodies instead declines. It is this separation that contributes to the reported selectivity as this being a face selective region. This is in contrast to more anterior face patches in which face selectivity peaks as early as 4 seconds. Further, if we look at the data from this paper collected using ECOG arrays, electrodes overlying face patch "O" show no preference for faces on the order of 400 ms. Together, these suggest

that although this area may be selective for faces, it is on a much longer time scale than one would suggest by a traditional population of neurons.

For if we compare this to traditional measures of macaque face patches, in the Tsao et al. 2006 study, they find 97% of cells within a face patch to be selective to faces with response latencies of less than 100 – 150 ms. From the data collected in this study and in comparison to the data in the Hung et al., 2015 paper, this area does not meet either of these criteria.

Rather, as was seen in Fig 2.5.B, c291, there do exist neurons in this population that appear to be active for much longer time scales than one would expect from only a 500 ms stimulus presentation with a 4 s ISI, even when taking into account the rise time of 0.5 s and decay time 1 – 3 s of GCaMP6s (T.-W. Chen et al. 2013). In this example, it is even possible to see the activity continuing through the ISI period and continuing at the start of subsequent trials. It is this type of long delay, sparse, and recurrent activity that is more likely to give rise to the signals found in face patch "O" in the Hung et al., 2015 paper. Furthermore, one observation that needs further analysis is the observation that many of the components identified in animal T that may be neuropil as indicated by their grid like structure and lack of direct relationship with any obvious somas on the field maps. These neuropil like components seem to be disproportionately selective to naturalistic images compared to other components. This neuropil signal maybe an indication that dendrites or axons transmit recurrent or feedback activity to this region selective for faces.

Although we do not find direct evidence supporting a canonical functional architecture of a face patch, we do find exciting evidence of natural scenes being represented in distinct clusters intercalated with low-level feature clusters. Given that V2 is an emergent area for natural scenes (Felsen et al. 2005; Gallant et al. n.d.; Koivisto et al. 2011; Ziemba et al. 2016) and feeds forward into the ventral stream, it may play a key role in filtering selected information forward to IT and providing an architecture to support recurrent and feedback activity to enhance particular signals.

Further, the suggestion that nearly 50% of cells in V2 are specific to natural scenes and exhibit increased suppressive tuning (Willmore, Prenger, and Gallant 2010) suggests that there may be a cell type identity giving rise to these clusters. To answer this question will necessitate the final execution of the volumetric immunohistochemistry and co-registration pipeline. Although we expect to find a distribution of inhibitory neurons supporting this architecture, it should be noted that the global effect of anesthesia is effected through altering the excitatory and inhibitory balance of neurons (Franks and Lieb 1994; Jevtović-Todorović et al. 1998). This may impact the ability to definitively characterize the selective, functional contribution of the inhibitory subclasses of neurons.

Throughout these analyses, strictly categorical analyses have been employed in which both a component's selectivity to a particular set of stimuli was categorized only in comparison to other stimulus sets. This approach was taken in order to compress the information contained in each component's activity into

fewer dimensions. Activity is averaged over a set window and only the significant maximal response of a component denotes its selectivity. Although this allows a clear categorization of components, it neither reveals the possibility that components may respond to more than one stimulus set nor does it allow insight into how the activity emerges over time. Future analyses will classify the components in respect to their graded encoding of multiple stimuli sets, in addition to revealing how their selectivity emerges in respect to time. For time based analyses, we will deconvolve the change in fluorescence to better approximate the underlying dynamics of the neural activity separate from the time constants of the genetically encoded calcium indicator.

Furthermore, in order to capture relationships across stimuli categories, we will perform high dimensional analyses with all stimuli categories and utilize PHATE (potential of heat-diffusion for affinity-base transition embedding) to visualize the analysis in 2D (Moon et al. 2019). This method of analysis preserves local and global structure in the data across dimensions.

5.2 Implications of negative regulation of endoplasmic reticulum stress-induced intrinsic apoptotic signaling in mPFC-NAc projection neurons

Through our retro-vTRAP study, we have shown that qPCR and IGV analyses show the expected patterns of enrichment and depletion of both positive and negative control genes across all four species. RNA-seq differential analyses demonstrate significant populations of enriched and depleted genes across all four species which are then curated by an ortholog analysis. Using the found orthologs to filter available gene ontology sets for each species reveals a single conserved gene ontology set that presents significant enrichment in marmoset and rat, with a non-significant enrichment also in mouse. This gene ontology set, GO: 1902236, is specific to negative regulation of ER-stress induced apoptosis. ER-stress induced apoptosis has been shown to be enhanced in mPFC and striatal circuits of depression. This specific population of layer V corticoaccumbal projection neurons may provide endogenous regulation of this pathway. In the context of the social brain, this may be critical to maintaining proper interactions, particularly in contexts of social dominance. When this projection becomes atypically regulated either through chronic social defeat or depression models, enhanced NAc ER-stress induced apoptotic activity is allowed to occur thereby remodulating the circuitry to critical to social behavior. More broadly, identifying this particular target conserved in at least three of our species, provides an intriguing possibility that this may be a critical signature of this projection in humans as well. If so, it could become a specific target not only for treatment of social disorders, but importantly, understanding the mechanisms by which we engage with stress typically.

A variety of physiological conditions, including hypoglycemia, oxidative stress, and a high-fat diet, can cause error in the protein-folding process within the ER. The accumulation of these misfolded proteins is the condition known as ER stress. Under ER stress, the Unfolded Protein Response (UPR) pathway is triggered to rescue the loss of function by reducing protein synthesis, promoting protein degradation, and increasing molecular chaperones of protein folding (Hetz and Papa 2018; Scheper and Hoozemans 2015). However, if the impacts of

ER stress overwhelm the stress response, apoptosis will occur (Hetz, Chevet, and Oakes 2015). In recent years ER stress has been hypothesized as a major culprit in the progression of major depressive disorder as well as other neurodegenerative diseases (Bown 2000; Nevell et al. 2014; Scheper and Hoozemans 2015; Xiang et al. 2017). Mice or rats exposed to chronic unpredictable mild stress (CUMS), chronic restraint stress (CRS), or social defeat stress in order to induce a model of depression have all shown an up regulation of ER stress-associated genes in key brain areas including the striatum and the PFC (Jangra et al. 2017; S.-Y. Liu et al. 2017; Mao et al. 2019; Pavlovsky et al. 2013). Further, pharmacological and genetic inhibition of these ER stress-related mediators have been proposed as a potential therapeutic strategy (Mao et al. 2019; Xiang et al. 2017). Evidence suggests antidepressants such as fluvoxamine, desipramine, and escitalopram among others exert their anti-depressant effect by reducing ER stress (Omi et al. 2014; L. Yang et al. 2018).

Our gene ontology set encompasses negative regulators of these ER stress pathways and may provide a modulation of negative regulation from the mPFC to the NAc. Given the areas involved, it may be a mechanism by which social interaction and reward reduce on going stress and could potentially be a genetic signature of this projection conserved across mice, rats, and marmosets. Given that the enrichment score fails to reach significance but shows a negative trend in the macaque does not reflect that it expresses a different pattern than the other three species, but rather, that the macaque data have much more noise, likely due to the more complicated surgical extraction. Further analysis on this data will need to be considered to determine if these are genuine species differences or if it is a reflection of the data quality. We additionally have a single section of the contralateral mPFC from macaque, St, brain banked for future studies. Processing of this last tissue sample may provide an additional data point to this set for further confirmation of seen patterns. However, due to the fact that our two macaque samples were both dedicated to RNA-sequencing experiments, we do not have the histological injection control for the macaque. There remains the possibility that the original injection failed to target the NAc. To address this confound, we will complete RNA-sequencing analyses on the tissue samples collected from the NAc in the macaque. We will compare the differentially expressed genes to known *in situ* hybridization (ISH) and immunohistochemistry markers such as calbindin-D28k (Meredith et al. 1996), to determine whether or not there is full confidence in our targeting. If these samples fail to show proper enrichment of these markers, we will need to exclude the macaque data. An alternative approach does not rely on the NAc tissue, but instead perform an extensive analysis of control genes within the mPFC tissue across all samples to ensure that we have specifically isolated projection neurons.

Upon selecting the final panel of input samples with or without the macaque samples, we will perform two additional analyses. The first will be a more relaxed, exploratory search for conserved genes within the gene ontologies. Originally, the gene ontology set of leading genes had to exclusively be comprised of conserved genes, but this is biased toward very small gene ontologies. As a result, we will create a graded analysis where we will look at different degrees of conservation within each gene ontology. This will also

enable us to more flexibly look at conserved genes that are differentially expressed per species thereby enabling the identification of a conserved gene that may identify this projection in only one of our species. Finally, we will take our identified genes and reference them against known ISH data sets and RNA-sequencing data sets from these species to determine whether retro-vTRAP can molecularly dissect this projection from population wide measures of the mPFC.

5.3 Identification of a protracted period of gastrulation reveals interventional opportunity in the developing marmoset embryo

This high resolution, serial marmoset ultrasound atlas builds on the tremendous work done in this field from the earliest *ex vivo* studies of embryos (Phillips 1976) through to the first ultrasound derived growth curves (Jaquish et al. 1995; Oerke, Einspanier, and Hodges 1995) and *in utero* MRI atlas (Hikishima et al. 2013). With ease of data sharing and accessibility to ultrasound units in most facilities, it establishes the opportunity to pursue not only remaining enigmas of common marmoset development but also facilitates utilizing their unique physiology to rapidly push forward molecular and transgenic utility to probe our understanding of reproduction, cognition, and biomedical interventions.

Excitingly, the evidence of this protracted growth period during gastrulation further reveals an opportunity to interrogate the molecular mechanisms underlying this delayed development. Given that there is nearly a two-week window during which gastrulation occurs in Stage VII (Fig 4.1.E), it is possible to sample amniotic fluid during this stage to determine what signaling factors occur locally. Similarly, there is a window of opportunity for introducing genetic manipulations using gene-editing tools such as CRISPR packaged in a lentivirus (Choi et al. 2016) into the amnion before closure of the neural tube. This is an unprecedented opportunity in non-human primates as it allows a transgenic model of the central nervous system without creating a transgenic whole animal model. Current work being done in the Brivanlou lab has shown promising success using this technique in the mouse and will be applied next to the marmoset.

One limitation of this ultrasound study is that there were no measured hormonal levels as measured in urine or blood to correspond to pregnancy staging or day of ovulation. In particular, measuring progesterone levels would give a more accurate day of ovulation and thereby fertilization (Oerke, Einspanier, and Hodges 1995). This would mitigate our uncertainty in calculating the estimated day post fertilization from gestation averages as provided in the literature. In future pregnancies, we plan to track these hormonal levels to confirm our estimations as made by ultrasound alone. Further, as we wish to make this an accessible resource to the community, there is a remaining uncertainty in how variable the quality of these measurements might be across different ultrasound machines and experimenters. As a result, we are creating a repository of database users so that they can submit their own ultrasound images to the database. Through crowdsourcing across machines and users, we aim to provide a more comprehensive and detailed atlas that will continue to be consistently refined and strengthened by the community.

5.4 Future directions

Individually, each finding contributes to a better understanding of the social brain and its underlying mechanisms in an animal model that shares many social behaviors with human behaviors. Taking these findings and the methods established together, it creates the opportunity to now be able to fully interrogate the social brain from across molecular and functional levels. This is an unprecedented opportunity in a primate species and creates the foundation for an extraordinary amount of exciting and promising research. It facilitates a critical inquiry into how typical neural populations functionally and genetically support typical social behavior in a genetically tractable primate, thereby making it possible to causally test how specific mechanisms of how psychiatric diseases give rise to atypical social behavior.

Utilizing all of the approaches established here, the next experiment we would like to conduct next builds off of the findings in the face patch network. In the first branch of this work, we aim to inject a genetically encoded calcium indictor into the amnion during stage VII of embryonic development. Depending on the efficiency of this viral transduction, it would allow interrogation of the functional architecture of more anterior face patches as well as the intervening cortex through the recording and volumetric immunohistochemistry methods detailed here. Further, upon identifying these face patches, we aim to inject each face patch retro-vTRAP to reveal the genetic signatures specific to the face patch network. Lastly, utilizing the genetic signatures identified, we will then be able to manipulate these genes through embryonic, amniotic injections. The degree of manipulation possible is dependent on the genetic signature found. Some genes may be able to be easily knocked out through CRISPR induced point mutations where as others may have a known promoter through which we could up regulate expression. Utilizing these manipulations with cell recording techniques as well as behavioral assays, we will have a fuller spectrum of insight into and control over a network within the social brain.

5.5 Final Remarks

With a rich history of scientific inquiry into understanding the social brain, we are still excitingly just at the beginning. However, utilizing the common marmoset as a bridge between the tremendous amounts of careful research done across classic techniques with the application of new methodologies well suited to the common marmoset; there is the opportunity to better understand our own cognitive and social functions. Using the marmoset, we are able to test hypotheses that not only have deep, conserved meaning in the shared aspects of our natural ethologies, but also that have tractability to reveal novel and scalable insights. The common marmoset provides a means by which we can establish a more common ground to understand ourselves in context.

REFERENCES

Adolphs, Ralph. 2009. "The Social Brain: Neural Basis of Social Knowledge." *Annual review of psychology* 60: 693–716. http://www.pubmedcentral.nih.gov/articlerender.fcgi?artid=2588649&tool=pmcentrez&rendertype=abstract (December 2, 2014).

Allison, Truett, Aina Puce, and Gregory McCarthy. 2000. "Social Perception from Visual Cues: Role of the STS Region." *Trends in Cognitive Sciences* 4(7): 267–78. http://www.sciencedirect.com/science/article/pii/S1364661300015011 (April 16, 2015).

Altmann, Stuart A. 1962. "A FIELD STUDY OF THE SOCIOBIOLOGY OF RHESUS MONKEYS, MACACA MULATTA." *Annals of the New York Academy of Sciences* 102(2): 338–435.

Anderson, Robert H et al. 2003. "Development of the Heart: (2) Septation of the Atriums and Ventricles." *Heart (British Cardiac Society)* 89(8): 949–58. http://www.ncbi.nlm.nih.gov/pubmed/12860885 (February 11, 2020).

Anderson, Steven W. et al. 1999. "Impairment of Social and Moral Behavior Related to Early Damage in Human Prefrontal Cortex." *Nature Neuroscience* 2(11): 1032–37.

Angelucci, Alessandra et al. 2002. "Circuits for Local and Global Signal Integration in Primary Visual Cortex." *The Journal of neuroscience : the official journal of the Society for Neuroscience* 22(19): 8633–46. http://www.ncbi.nlm.nih.gov/pubmed/12351737 (August 31, 2015).

Angelucci, Alessandra, and Paul C Bressloff. 2006. "Contribution of Feedforward, Lateral and Feedback Connections to the Classical Receptive Field Center and Extra-Classical Receptive Field Surround of Primate V1 Neurons." *Progress in brain research* 154: 93–120. http://www.sciencedirect.com/science/article/pii/S0079612306540051 (August 30, 2015).

Bakken, Trygve E. et al. 2020. "Evolution of Cellular Diversity in Primary Motor Cortex of Human, Marmoset Monkey, and Mouse." *bioRxiv*: 2020.03.31.016972.

Bakrania, Preeti et al. 2008. "Mutations in BMP4 Cause Eye, Brain, and Digit Developmental Anomalies: Overlap between the BMP4 and Hedgehog Signaling Pathways." *American journal of human genetics* 82(2): 304–19. http://www.ncbi.nlm.nih.gov/pubmed/18252212 (February 11, 2020).

Bao, Pinglei, Liang She, Mason McGill, and Doris Y. Tsao. 2020. "A Map of Object Space in Primate Inferotemporal Cortex." *Nature*: 1–6. http://www.nature.com/articles/s41586-020-2350-5 (June 8, 2020).

Barton, R A, and P H Harvey. 2000. "Mosaic Evolution of Brain Structure in Mammals." *Nature* 405(6790): 1055–58. http://dx.doi.org/10.1038/35016580 (August 30, 2015).

Belleau, Emily L., Michael T. Treadway, and Diego A. Pizzagalli. 2019. "The Impact of Stress and Major Depressive Disorder on Hippocampal and Medial Prefrontal Cortex Morphology." *Biological Psychiatry* 85(6): 443–53.

Belmonte, Juan Carlos Izpisua et al. 2015. "Brains, Genes, and Primates." *Neuron* 86(3): 617–31. http://www.sciencedirect.com/science/article/pii/S0896627315002172 (May 7, 2015).

Ben-Ami Bartal, Inbal et al. 2014. "Pro-Social Behavior in Rats Is Modulated by Social Experience." *eLife* 3: e01385.

Berkowitz, Laura A., Adam L. Knight, Guy A. Caldwell, and Kim A. Caldwell. 2008. "Generation of Stable Transgenic C. Elegans Using Microinjection." *Journal of Visualized Experiments* (18).

Bezerra, Bruna Martins, and Antonio Souto. 2008. "Structure and Usage of the Vocal Repertoire of Callithrix Jacchus." *International Journal of Primatology* 29(3): 671–701. http://link.springer.com/10.1007/s10764-008-9250-0 (August 7, 2015).

Bicks, Lucy K., Hiroyuki Koike, Schahram Akbarian, and Hirofumi Morishita. 2015. "Prefrontal Cortex and Social Cognition in Mouse and Man." *Frontiers in Psychology* 6(NOV): 1805.

Blaas, H. G.K. 1999. "The Examination of the Embryo and Early Fetus: How and by Whom?" *Ultrasound in Obstetrics and Gynecology* 14(3): 153–58.

Bonhomme, Vincent et al. 2019. "General Anesthesia: A Probe to Explore Consciousness." *Frontiers in Systems Neuroscience* 13: 36.

Bonin, Vincent, Mark H Histed, Sergey Yurgenson, and R Clay Reid. 2011. "Local Diversity and Fine-Scale Organization of Receptive Fields in Mouse Visual Cortex." *The Journal of neuroscience : the official journal of the Society for Neuroscience* 31(50): 18506–21. http://www.jneurosci.org/content/31/50/18506.short (September 15, 2015).

Bosking, William H., Ying Zhang, Brett Schofield, and David Fitzpatrick. 1997. "Orientation Selectivity and the Arrangement of Horizontal Connections in Tree Shrew Striate Cortex." *J. Neurosci.* 17(6): 2112–27. http://www.jneurosci.org/content/17/6/2112.short (August 31, 2015).

Bourne, James A, and Marcello G P Rosa. 2003. "Preparation for the in Vivo Recording of Neuronal Responses in the Visual Cortex of Anaesthetised Marmosets (Callithrix Jacchus)." *Brain research. Brain research protocols* 11(3): 168–77. http://www.ncbi.nlm.nih.gov/pubmed/12842222 (July 28, 2015).

Bown, C. 2000. "Increased Temporal Cortex ER Stress Proteins in Depressed Subjects Who Died by Suicide." *Neuropsychopharmacology* 22(3): 327–32. http://www.nature.com/doifinder/10.1016/S0893-133X(99)00091-3 (April 26, 2020).

Branch, Audrey et al. 2019. "An Optimized Protocol for IDISCO+ Rat Brain Clearing, Imaging, and Analysis." *bioRxiv*: 639674. https://www.biorxiv.org/content/10.1101/639674v1 (April 30, 2020).

Brosnan, Sarah F., Hillary C. Schiff, and Frans B. M. de Waal. 2005. "Tolerance for Inequity May Increase with Social Closeness in Chimpanzees." *Proceedings of the Royal Society B: Biological Sciences* 272(1560): 253–58. https://royalsocietypublishing.org/doi/10.1098/rspb.2004.2947 (April 30, 2020).

Brothers, L. 2002. "The Social Brain: A Project for Integrating Primate Behavior and Neurophysiology in a New Domain." *Foundations in social neuroscience*. https://books.google.com/books?hl=en&lr=&id=nQk5Pv9kf-YC&oi=fnd&pg=PA367&dq=The+social+brain:+a+project+for+integrating+primate+behavior+and+neurophysiology+in+a+new+domain&ots=rxaS1MydcP&sig=ISQJK3NjwalJRS_hyENcEFiAqxg (August 30, 2015).

Burkart, Judith M, and Christa Finkenwirth. 2014. "Marmosets as Model Species in Neuroscience and Evolutionary Anthropology." *Neuroscience research* 93: 8–19. http://www.sciencedirect.com/science/article/pii/S0168010214002144 (April 21, 2015).

Cacioppo, John T. 2002. "Social Neuroscience: Understanding the Pieces Fosters Understanding the Whole and Vice Versa." *The American psychologist* 57(11): 819–31.

Chambers, P. L., and J. P. Hearn. 1985. "Embryonic, Foetal and Placental Development in the Common Marmoset Monkey (Callithrix Jacchus)." *Journal of Zoology* 207(4): 545–61. http://doi.wiley.com/10.1111/j.1469-7998.1985.tb04951.x (December 19, 2019).

Chang, Le, and Doris Y. Tsao. 2017. "The Code for Facial Identity in the Primate Brain." *Cell* 169(6): 1013-1028.e14.

Chaplin, Tristan A, Hsin-Hao Yu, and Marcello G P Rosa. 2013. "Representation of the Visual Field in the Primary Visual Area of the Marmoset Monkey: Magnification Factors, Point-Image Size, and Proportionality to Retinal Ganglion Cell Density." *The Journal of comparative neurology* 521(5): 1001–19. http://www.ncbi.nlm.nih.gov/pubmed/22911425 (July 13, 2015).

Chen, Tsai-Wen et al. 2013. "Ultrasensitive Fluorescent Proteins for Imaging Neuronal Activity." *Nature* 499(7458): 295–300. http://www.nature.com/nature/journal/v499/n7458/fig_tab/nature12354_F2.html (July 9, 2014).

Chen, Xiaowei et al. 2011. "Functional Mapping of Single Spines in Cortical Neurons in Vivo." *Nature* 475(7357): 501–5. http://dx.doi.org/10.1038/nature10193 (August 8, 2015).

Chi, Jingyi, Audrey Crane, Zhuhao Wu, and Paul Cohen. 2018. "Adipo-Clear: A Tissue Clearing Method for Three-Dimensional Imaging of Adipose Tissue." *Journal of Visualized Experiments* (137). http://www.ncbi.nlm.nih.gov/pubmed/30102289 (June 4, 2019).

Choi, J. G. et al. 2016. "Lentivirus Pre-Packed with Cas9 Protein for Safer Gene Editing." *Gene Therapy* 23(7): 627–33.

Covington, Herbert E. et al. 2010. "Antidepressant Effect of Optogenetic Stimulation of the Medial Prefrontal Cortex." *Journal of Neuroscience* 30(48): 16082–90.

Crawley, Jacqueline N. et al. 2007. "Social Approach Behaviors in Oxytocin Knockout Mice: Comparison of Two Independent Lines Tested in Different Laboratory Environments." *Neuropeptides* 41(3): 145–63.

Dalgard, Clifton L. et al. 2015. "A Novel Analytical Brain Block Tool to Enable Functional Annotation of Discriminatory Transcript Biomarkers among Discrete Regions of the Fronto-Limbic Circuit in Primate Brain." *Brain Research* 1600: 42–58. https://www.sciencedirect.com/science/article/pii/S0006899314017193 (March 6, 2019).

Dalley, Jeffrey W., Rudolf N. Cardinal, and Trevor W. Robbins. 2004. "Prefrontal Executive and Cognitive Functions in Rodents: Neural and Neurochemical Substrates." In *Neuroscience and Biobehavioral Reviews*, Pergamon, 771–84.

Deng, Liang et al. 2018. "Research Advances on Embryonic Diapause in Mammals." *Animal Reproduction Science* 198: 1–10. http://www.ncbi.nlm.nih.gov/pubmed/30266523 (December 19, 2019).

Desimone, Robert, and Charles G. Gross. 1979. "Visual Areas in the Temporal Cortex of the Macaque." *Brain Research* 178(2–3): 363–80. http://www.sciencedirect.com/science/article/pii/0006899379906991 (August 30, 2015).

Dickey, Richard P., and Raymond F. Gasser. 1993. "Ultrasound Evidence for Variability in the Size and Development of Normal Human Embryos before the Tenth Post-Insemination Week after Assisted Reproductive Technologies." *Human Reproduction* 8(2): 331–37. https://academic.oup.com/humrep/article/665978/Ultrasound (April 9, 2020).

Dilks, Daniel D. et al. 2015. "Awake FMRI Reveals a Specialized Region in Dog Temporal Cortex for Face Processing." *PeerJ* 3: e1115. https://peerj.com/articles/1115 (August 8, 2015).

Dolan, R. J. 2002. "Neuroscience and Psychology: Emotion, Cognition, and Behavior." *Science* 298(5596): 1191–94.

Doyle, Joseph P et al. 2008. "Application of a Translational Profiling Approach for the Comparative Analysis of CNS Cell Types." *Cell* 135(4): 749–62. http://www.ncbi.nlm.nih.gov/pubmed/19013282.

Drane, Laurel, Joshua A. Ainsley, Mark R. Mayford, and Leon G. Reijmers. 2014. "A Transgenic Mouse Line for Collecting Ribosome-Bound MRNA Using the Tetracycline Transactivator System." *Frontiers in Molecular Neuroscience* 7: 82. http://journal.frontiersin.org/article/10.3389/fnmol.2014.00082/abstract (April 25, 2020).

Dunbar, R. I.M., and Susanne Shultz. 2007. "Evolution in the Social Brain." *Science* 317(5843): 1344–47.

Enders, Allen C., and Alexander Lopata. 1999. "Implantation in the Marmoset Monkey: Expansion of the Early Implantation Site." *The Anatomical Record* 256(3): 279–99. http://www.ncbi.nlm.nih.gov/pubmed/10521786 (January 7, 2020).

Eslinger, Paul J., Claire V. Flaherty-Craig, and Arthur L. Benton. 2004. "Developmental Outcomes after Early Prefrontal Cortex Damage." *Brain and Cognition* 55(1): 84–103.

Felsen, Gidon, Jon Touryan, Feng Han, and Yang Dan. 2005. "Cortical Sensitivity to Visual Features in Natural Scenes." *journals.plos.org* 3(10). www.plosbiology.org (April 30, 2020).

Finlay, B L, and R B Darlington. 1995. "Linked Regularities in the Development and Evolution of Mammalian Brains." *Science (New York, N.Y.)* 268(5217): 1578–84. http://www.ncbi.nlm.nih.gov/pubmed/7777856 (August 30, 2015).

Fisher, Clark, and Winrich A. Freiwald. 2015. "Whole-Agent Selectivity within the Macaque Face-Processing System." *Proceedings of the National Academy of Sciences of the United States of America* 112(47): 14717–22.

Forbes, Chad E., and Jordan Grafman. 2010. "The Role of the Human Prefrontal Cortex in Social Cognition and Moral Judgment." *Annual Review of Neuroscience* 33(1): 299–324.

Franks, N. P., and W. R. Lieb. 1994. "Molecular and Cellular Mechanisms of General Anaesthesia." *Nature* 367(6464): 607–14.

Freeman, Jeremy et al. 2013. "A Functional and Perceptual Signature of the Second Visual Area in Primates." *Nature Neuroscience* 16(7): 974–81. http://www.nature.com/articles/nn.3402 (September 28, 2018).

Freeman, Jeremy, and Eero P Simoncelli. 2011. "Metamers of the Ventral Stream." *Nature neuroscience* 14(9): 1195–1201. http://www.ncbi.nlm.nih.gov/pubmed/21841776 (September 5, 2018).

Freiwald, WA, and DY Tsao. 2010. "Functional Compartmentalization and Viewpoint Generalization within the Macaque Face-Processing System." *Science*. http://www.sciencemag.org/content/330/6005/845.short (August 31, 2015).

Freiwald, WA, DY Tsao, and MS Livingstone. 2009. "A Face Feature Space in the Macaque Temporal Lobe." *Nature neuroscience*. http://www.nature.com/neuro/journal/v12/n9/abs/nn.2363.html (August 31, 2015).

Friedman, Lauren G. et al. 2015. "Cadherin-8 Expression, Synaptic Localization, and Molecular Control of Neuronal Form in Prefrontal Corticostriatal Circuits." *Journal of Comparative Neurology* 523(1): 75–92.

Gallant, JL, CE Connor, DC Van Essen - Neuroreport, and undefined 1998. "Neural Activity in Areas V1, V2 and V4 during Free Viewing of Natural Scenes Compared to Controlled Viewing." *journals.lww.com*. https://journals.lww.com/neuroreport/Fulltext/1998/06220/Neural_activity_in_areas_V1,_V2_and_V4_during_free.45.aspx (April 30, 2020).

Gilbert, CD, and TN Wiesel. 1989. "Columnar Specificity of Intrinsic Horizontal and Corticocortical Connections in Cat Visual Cortex." *J. Neurosci.* 9(7): 2432–42. http://www.jneurosci.org/content/9/7/2432.short (August 31, 2015).

Giovannucci, Andrea et al. 2019. "CaImAn an Open Source Tool for Scalable Calcium Imaging Data Analysis." *eLife* 8. https://elifesciences.org/articles/38173 (April 1, 2019).

Grossmann, Tobias. 2013. "The Role of Medial Prefrontal Cortex in Early Social Cognition." *Frontiers in Human Neuroscience* 7(JUL): 340. http://journal.frontiersin.org/article/10.3389/fnhum.2013.00340/abstract (April 25, 2020).

Gunaydin, Lisa A. et al. 2014. "Natural Neural Projection Dynamics Underlying Social Behavior." *Cell* 157(7): 1535–51.

Guy, Joseph R. et al. 2016. "Custom Fit 3D-Printed Brain Holders for Comparison of Histology with MRI in Marmosets." *Journal of Neuroscience Methods* 257: 55–63. https://www.sciencedirect.com/science/article/pii/S0165027015003350 (January 3, 2020).

Harkness, L M, M Rodger, and D T Baird. 1996. 3 Human Reproduction Update *Morphological and Molecular Characteristics of Living Human Fetuses between Carnegie Stages 7 and 23: Ultrasound Scanning and Direct Measurements*. https://academic.oup.com/humupd/article-abstract/3/1/25/593774 (April 9, 2020).

Hearn, J P et al. 1978. "Use of the Common Marmoset, Callithrix Jacchus, in Reproductive Research." *Primates in medicine* 10: 40–49. http://www.ncbi.nlm.nih.gov/pubmed/417331 (February 11, 2020).

Heiman, Myriam et al. 2008. "A Translational Profiling Approach for the Molecular Characterization of CNS Cell Types." *Cell* 135(4): 738–48. http://www.ncbi.nlm.nih.gov/pubmed/19013281.

———. 2014. "Cell Type-Specific MRNA Purification by Translating Ribosome Affinity Purification (TRAP)." *Nature protocols* 9(6): 1282–91. http://www.ncbi.nlm.nih.gov/pubmed/24810037.

Hetz, Claudio, Eric Chevet, and Scott A. Oakes. 2015. "Proteostasis Control by the Unfolded Protein Response." *Nature Cell Biology* 17(7): 829–38.

Hetz, Claudio, and Feroz R. Papa. 2018. "The Unfolded Protein Response and Cell Fate Control." *Molecular Cell* 69(2): 169–81.

Hikishima, K. et al. 2013. "Atlas of the Developing Brain of the Marmoset Monkey Constructed Using Magnetic Resonance Histology." *Neuroscience* 230: 102–13. https://www.sciencedirect.com/science/article/pii/S0306452212009736?via%3Dihub (December 18, 2019).

Hill, M.A. 2020. "Embryology Carnegie Stage Comparison." https://embryology.med.unsw.edu.au/embryology/index.php/Carnegie_Stage_Comparison (February 11, 2020).

Hofer, Sonja B et al. 2011. "Differential Connectivity and Response Dynamics of Excitatory and Inhibitory Neurons in Visual Cortex." *Nature neuroscience* 14(8): 1045–52. http://dx.doi.org/10.1038/nn.2876 (July 16, 2014).

Hofman, Michel A. 2014. "Evolution of the Human Brain: When Bigger Is Better." *Frontiers in neuroanatomy* 8: 15. http://journal.frontiersin.org/article/10.3389/fnana.2014.00015/abstract (June 19, 2015).

Hubel, D. H., and T. N. Wiesel. 1968. "Receptive Fields and Functional Architecture of Monkey Striate Cortex." *The Journal of Physiology* 195(1): 215–43. http://doi.wiley.com/10.1113/jphysiol.1968.sp008455 (October 5, 2015).

Hubel, DH, and TN Wiesel. 1974. "Sequence Regularity and Geometry of Orientation Columns in the Monkey Striate Cortex." *Journal of Comparative Neurology*. http://onlinelibrary.wiley.com/doi/10.1002/cne.901580304/full (August 31, 2015).

Hung, Chia-Chun et al. 2015. "Functional Mapping of Face-Selective Regions in the Extrastriate Visual Cortex of the Marmoset." *J. Neurosci.* 35(3): 1160–72. http://www.jneurosci.org/content/35/3/1160.abstract?etoc (January 21, 2015).

Insel, Thomas R., and Russell D. Fernald. 2004. "HOW THE BRAIN PROCESSES SOCIAL INFORMATION: Searching for the Social Brain." *Annual Review of Neuroscience* 27(1): 697–722. http://www.annualreviews.org/doi/10.1146/annurev.neuro.27.070203.144148 (April 25, 2020).

Isaacson, Jeffry S, and Massimo Scanziani. 2011. "How Inhibition Shapes Cortical Activity." *Neuron* 72(2): 231–43. http://www.sciencedirect.com/science/article/pii/S0896627311008798 (July 11, 2014).

Ito, Minami, and Hidehiko Komatsu. 2004. "Representation of Angles Embedded within Contour Stimuli in Area V2 of Macaque Monkeys." *Journal of Neuroscience* 24(13): 3313–24.

Jangra, Ashok et al. 2017. "Sodium Phenylbutyrate and Edaravone Abrogate Chronic Restraint Stress-Induced Behavioral Deficits: Implication of Oxido-Nitrosative, Endoplasmic Reticulum Stress Cascade, and Neuroinflammation." *Cellular and Molecular Neurobiology* 37(1): 65–81.

Jaquish, Cashell E., Robert L. Toal, Suzette D. Tardif, and Robert L. Carson. 1995. "Use of Ultrasound to Monitor Prenatal Growth and Development in the Common Marmoset (Callithrix Jacchus)." *American Journal of Primatology* 36(4): 259–75. http://doi.wiley.com/10.1002/ajp.1350360402 (January 24, 2018).

Jevtović-Todorović, V. et al. 1998. "Nitrous Oxide (Laughing Gas) Is an NMDA Antagonist, Neuroprotectant and Neurotoxin." *Nature Medicine* 4(4): 460–63.

Juavinett, Ashley L. et al. 2017. "Automated Identification of Mouse Visual Areas with Intrinsic Signal Imaging." *Nature Protocols* 12(1): 32–43.

Kanwisher, Nancy, Josh McDermott, and Marvin M. Chun. 1997. "The Fusiform Face Area: A Module in Human Extrastriate Cortex Specialized for Face Perception." *J. Neurosci.* 17(11): 4302–11. http://www.jneurosci.org/content/17/11/4302.full (August 31, 2015).

Kanwisher, Nancy, and Galit Yovel. 2006. "The Fusiform Face Area: A Cortical Region Specialized for the Perception of Faces." *Philosophical transactions of the Royal Society of London. Series B, Biological sciences* 361(1476): 2109–28. http://www.pubmedcentral.nih.gov/articlerender.fcgi?artid=1857737&tool=pmcentrez&rendertype=abstract (April 29, 2015).

Kendrick, K M. 1991. "How the Sheep's Brain Controls the Visual Recognition of Animals and Humans." *Journal of animal science* 69(12): 5008–16. http://www.ncbi.nlm.nih.gov/pubmed/1808194 (August 31, 2015).

Kerlin, Aaron M, Mark L Andermann, Vladimir K Berezovskii, and R Clay Reid. 2010. "Broadly Tuned Response Properties of Diverse Inhibitory Neuron Subtypes in Mouse Visual Cortex." *Neuron* 67(5): 858–71. http://www.pubmedcentral.nih.gov/articlerender.fcgi?artid=3327881&tool=pmcentrez&rendertype=abstract (March 25, 2015).

Kingsbury, Lyle et al. 2019. "Correlated Neural Activity and Encoding of Behavior across Brains of Socially Interacting Animals." *Cell* 178(2): 429-446.e16.

Ko, Jaewon. 2017. "Neuroanatomical Substrates of Rodent Social Behavior: The Medial Prefrontal Cortex and Its Projection Patterns." *Frontiers in Neural Circuits* 11: 41.

Koivisto, Mika et al. 2011. "Brief Communications Recurrent Processing in V1/V2 Contributes to Categorization of Natural Scenes." *Soc Neuroscience*. www.iaps-association.org; (April 30, 2020).

Koski, Sonja E. et al. 2017. "Common Marmoset (Callithrix Jacchus) Personality." *Journal of Comparative Psychology* 131(4): 326–36. http://www.ncbi.nlm.nih.gov/pubmed/29022726 (July 5, 2019).

Kravitz, Dwight J et al. 2013. "The Ventral Visual Pathway: An Expanded Neural Framework for the Processing of Object Quality." *Trends in cognitive sciences* 17(1): 26–49. http://www.pubmedcentral.nih.gov/articlerender.fcgi?artid=3532569&tool=pmcentrez&rendertype=abstract (February 8, 2015).

Kriegeskorte, N. 2007. "Individual Faces Elicit Distinct Response Patterns in Human Anterior Temporal Cortex." *Proceedings of the ….* http://www.pnas.org/content/104/51/20600.short (August 31, 2015).

Kropp, Jenna, Andrea Di Marzo, and Thaddeus Golos. 2017. "Assisted Reproductive Technologies in the Common Marmoset: An Integral Species for Developing Nonhuman Primate Models of Human Diseases†." *Biology of Reproduction* 96(2): 277–87. https://academic.oup.com/biolreprod/article/96/2/277/2948764 (July 1, 2018).

Krueger, Frank, Aron K. Barbey, and Jordan Grafman. 2009. "The Medial Prefrontal Cortex Mediates Social Event Knowledge." *Trends in Cognitive Sciences* 13(3): 103–9.

Ku, Shih-Pi, Andreas S Tolias, Nikos K Logothetis, and Jozien Goense. 2011. "FMRI of the Face-Processing Network in the Ventral Temporal Lobe of Awake and Anesthetized Macaques." *Neuron* 70(2): 352–62. http://www.sciencedirect.com/science/article/pii/S0896627311002054 (July 1, 2015).

Kumar, Sunil et al. 2013. "Cortical Control of Affective Networks." *Journal of Neuroscience* 33(3): 1116–29.

Kumar, T. Rajendra et al. 2009. "Transgenic Mouse Technology: Principles and Methods." *Methods in molecular biology (Clifton, N.J.)* 590: 335–62.

Landi, Sofia M, and Winrich A Freiwald. 2017. "Two Areas for Familiar Face Recognition in the Primate Brain." *Science (New York, N.Y.)* 357(6351): 591–95. http://www.ncbi.nlm.nih.gov/pubmed/28798130.

Lee, Seung-Hee et al. 2012. "Activation of Specific Interneurons Improves V1 Feature Selectivity and Visual Perception." *Nature* 488(7411): 379–83. http://dx.doi.org/10.1038/nature11312 (June 10, 2015).

Leopold, David A, and Gillian Rhodes. 2010. "A Comparative View of Face Perception." *Journal of comparative psychology (Washington, D.C. : 1983)* 124(3): 233–51. http://www.pubmedcentral.nih.gov/articlerender.fcgi?artid=2998394&tool=pmcentrez&rendertype=abstract (August 31, 2015).

Levy, Dana Rubi et al. 2019. "Dynamics of Social Representation in the Mouse Prefrontal Cortex." *Nature Neuroscience* 22(12): 2013–22.

Liu, Jing et al. 2014. "Cell-Specific Translational Profiling in Acute Kidney Injury." *Journal of Clinical Investigation* 124(3): 1242–54.

Liu, Junjie V. et al. 2013. "FMRI in the Awake Marmoset: Somatosensory-Evoked Responses, Functional Connectivity, and Comparison with Propofol Anesthesia." *NeuroImage* 78: 186–95. https://www.sciencedirect.com/science/article/pii/S1053811913002875 (July 16, 2018).

Liu, Shu-Yun et al. 2017. "Hydrogen Sulfide Inhibits Chronic Unpredictable Mild Stress-Induced Depressive-Like Behavior by Upregulation of Sirt-1: Involvement in Suppression of Hippocampal Endoplasmic Reticulum Stress." *The international journal of neuropsychopharmacology* 20(11): 867–76. http://www.ncbi.nlm.nih.gov/pubmed/28482013 (April 26, 2020).

Liu, Zheng et al. 2016. "Prefrontal Cortex to Accumbens Projections in Sleep Regulation of Reward." *Journal of Neuroscience* 36(30): 7897–7910.

Livak, Kenneth J., and Thomas D. Schmittgen. 2001. "Analysis of Relative Gene Expression Data Using Real-Time Quantitative PCR and the 2-ΔΔCT Method." *Methods* 25(4): 402–8.

Love, Michael I, Wolfgang Huber, and Simon Anders. 2014. "Moderated Estimation of Fold Change and Dispersion for RNA-Seq Data with DESeq2." *Genome biology* 15(12): 550. http://www.ncbi.nlm.nih.gov/pubmed/25516281.

Lund, J. S. 2003. "Anatomical Substrates for Functional Columns in Macaque Monkey Primary Visual Cortex." *Cerebral Cortex* 13(1): 15–24. http://cercor.oxfordjournals.org/content/13/1/15.short (August 31, 2015).

Machado, Christopher J., and Jocelyne Bachevalier. 2003. "Non-Human Primate Models of Childhood Psychopathology: The Promise and the Limitations." *Journal of Child Psychology and Psychiatry* 44(1): 64–87. http://doi.wiley.com/10.1111/1469-7610.00103 (April 25, 2020).

Mao, Jiaxin et al. 2019. "Role of Endoplasmic Reticulum Stress in Depression (Review)." *Molecular Medicine Reports* 20(6): 4774–80.

"Marmoset Gene Atlas." https://gene-atlas.brainminds.riken.jp/ (April 28, 2020).

McLoughlin, Niall, and Ingo Schiessl. 2006. "Orientation Selectivity in the Common Marmoset (Callithrix Jacchus): The Periodicity of Orientation Columns in V1 and V2." *NeuroImage* 31(1): 76–85. https://www.sciencedirect.com/science/article/pii/S1053811905025206?via%3Dihub (July 23, 2018).

Mellén, Marian et al. 2012. "MeCP2 Binds to 5hmC Enriched within Active Genes and Accessible Chromatin in the Nervous System." *Cell* 151(7): 1417–30. http://www.ncbi.nlm.nih.gov/pubmed/23260135.

Meredith, G.E., A. Pattiselanno, H.J. Groenewegen, and S.N. Haber. 1996. "Shell and Core in Monkey and Human Nucleus Accumbens Identified with Antibodies to Calbindin-D28k." *The Journal of Comparative Neurology* 365(4): 628–39. http://doi.wiley.com/10.1002/%28SICI%291096-9861%2819960219%29365%3A4%3C628%3A%3AAID-CNE9%3E3.0.CO%3B2-6 (March 6, 2019).

Miller, Cory T. et al. 2016a. "Marmosets: A Neuroscientific Model of Human Social Behavior." *Neuron* 90(2): 219–33. http://linkinghub.elsevier.com/retrieve/pii/S0896627316300071 (July 3, 2017).

Miller, Cory T. et al. 2016b. "Marmosets: A Neuroscientific Model of Human Social Behavior." *Neuron* 90(2): 219–33.

———. 2017. "Why Marmosets?" *Developmental Neurobiology* 77(3): 237–43. http://doi.wiley.com/10.1002/dneu.22483 (September 5, 2017).

Mitchell, Jude F, and David A Leopold. 2015. "The Marmoset Monkey as a Model for Visual Neuroscience." *Neuroscience research* 93: 20–46. http://www.sciencedirect.com/science/article/pii/S0168010215000267 (April 20, 2015).

Mitchell, Jude F, John H Reynolds, and Cory T Miller. 2014. "Active Vision in Marmosets: A Model System for Visual Neuroscience." *The Journal of neuroscience : the official journal of the Society for Neuroscience* 34(4): 1183–94. http://www.pubmedcentral.nih.gov/articlerender.fcgi?artid=3898283&tool=pmcentrez&rendertype=abstract (October 17, 2014).

Moeller, S, WA Freiwald, and DY Tsao. 2008. "Patches with Links: A Unified System for Processing Faces in the Macaque Temporal Lobe." *Science*. http://www.sciencemag.org/content/320/5881/1355.short (August 31, 2015).

Moon, Kevin R. et al. 2019. "Visualizing Structure and Transitions in High-Dimensional Biological Data." *Nature Biotechnology* 37(12): 1482–92.

Moore, H. D. M., Sara Gems, and J. P Hearn. 1985. "Early Implantation Stages in the Marmoset Monkey (Callithrix Jacchus)." *American Journal of Anatomy* 172(4): 265–78. http://www.ncbi.nlm.nih.gov/pubmed/3922211 (November 12, 2019).

Moorman, Antoon et al. 2003. "Development of the Heart: (1) Formation of the Cardiac Chambers and Arterial Trunks." *Heart (British Cardiac Society)* 89(7): 806–14. http://www.ncbi.nlm.nih.gov/pubmed/12807866 (February 11, 2020).

Mountcastle, VB. 1957. "Modality and Topographic Properties of Single Neurons of Cat's Somatic Sensory Cortex." *Journal of neurophysiology*. http://jn.physiology.org/content/jn/20/4/408.full.pdf (August 31, 2015).

———. 1997. "The Columnar Organization of the Neocortex." *Brain*. http://brain.oxfordjournals.org/content/brain/120/4/701.full.pdf (August 31, 2015).

Nakajima, Miho, Andreas Görlich, and Nathaniel Heintz. 2014. "Oxytocin Modulates Female Sociosexual Behavior through a Specific Class of Prefrontal Cortical Interneurons." *Cell* 159(2): 295–305. http://www.ncbi.nlm.nih.gov/pubmed/25303526.

National Academies of Sciences, Engineering, and Medicine; Division on Earth and Life Studies; Institute for Laboratory Animal Research; Roundtable on Science and Welfare in Laboratory Animal Use, Lida Anestidou, and Anne Frances Johnson. 2019. Care, Use, and Welfare of Marmosets as Animal Models for Gene Editing-Based Biomedical Research: Proceedings of a Workshop *Care, Use, and Welfare of Marmosets as Animal Models for Gene Editing-Based Biomedical Research*. National Academies Press (US). http://www.ncbi.nlm.nih.gov/pubmed/31381285 (February 11, 2020).

Nectow, Alexander R et al. 2017. "Rapid Molecular Profiling of Defined Cell Types Using Viral TRAP." *Cell reports* 19(3): 655–67. http://www.ncbi.nlm.nih.gov/pubmed/28423326.

Nestler, Eric J., and Steven E. Hyman. 2010. "Animal Models of Neuropsychiatric Disorders." *Nature Neuroscience* 13(10): 1161–69.

Nevell, Lisa et al. 2014. "Elevated Systemic Expression of ER Stress Related Genes Is Associated with Stress-Related Mental Disorders in the Detroit Neighborhood Health Study." *Psychoneuroendocrinology* 43: 62–70.

O'Rahilly, Ronan., Fabiola. Müller, and George Linius Streeter. 1987. *Developmental Stages in Human Embryos : Including a Revision of Streeter's "Horizons" and a Survey of the Carnegie Collection*. [Washington D.C.]: Carnegie Institution of Washington.

Oerke, A.-K., A. Einspanier, and J. K. Hodges. 1995. "Detection of Pregnancy and Monitoring Patterns of Uterine and Fetal Growth in the Marmoset Monkey (Callithrix Jacchus) by Real-Time Ultrasonography." *American Journal of Primatology* 36(1): 1–13. http://doi.wiley.com/10.1002/ajp.1350360102 (June 8, 2020).

Omi, T. et al. 2014. "Fluvoxamine Alleviates ER Stress via Induction of Sigma-1 Receptor." *Cell Death and Disease* 5(7): e1332–e1332.

Park, Jung Eun et al. 2016. "Generation of Transgenic Marmosets Expressing Genetically Encoded Calcium Indicators." *Scientific Reports* 6(1): 34931. http://www.nature.com/articles/srep34931 (December 20, 2019).

Park, Jung Eun, and Afonso C. Silva. 2019. "Generation of Genetically Engineered Non-Human Primate Models of Brain Function and Neurological Disorders." *American Journal of Primatology* 81(2): e22931. http://doi.wiley.com/10.1002/ajp.22931 (December 20, 2019).

Pavlovsky, A. A. et al. 2013. "Psychological Stress, Cocaine and Natural Reward Each Induce Endoplasmic Reticulum Stress Genes in Rat Brain." *Neuroscience* 246: 160–69.

Perrett, D.I., E.T. Rolls, and W. Caan. 1982. "Visual Neurones Responsive to Faces in the Monkey Temporal Cortex." *Experimental Brain Research* 47(3). http://link.springer.com/10.1007/BF00239352 (August 31, 2015).

Phillips, I R. 1976. "The Embryology of the Common Marmoset (Callithrix Jacchus)." *Advances in anatomy, embryology, and cell biology* 52(5): 3–47. http://www.ncbi.nlm.nih.gov/pubmed/827927 (December 18, 2019).

Platt, Michael L., Robert M. Seyfarth, and Dorothy L. Cheney. 2016. "Adaptations for Social Cognition in the Primate Brain." *Philosophical Transactions of the Royal Society B: Biological Sciences* 371(1687).

Prins, Noeline W. et al. 2017. "Common Marmoset (Callithrix Jacchus) as a Primate Model for Behavioral Neuroscience Studies." *Journal of Neuroscience Methods* 284: 35–46.

"QuickGO::Term GO:1902236." https://www.ebi.ac.uk/QuickGO/term/GO:1902236 (April 28, 2020).

Renfree, Marilyn B, and Jane C Fenelon. 2017. "The Enigma of Embryonic Diapause." *Development (Cambridge, England)* 144(18): 3199–3210. http://www.ncbi.nlm.nih.gov/pubmed/28928280 (December 18, 2019).

Renier, Nicolas et al. 2014. "IDISCO: A Simple, Rapid Method to Immunolabel Large Tissue Samples for Volume Imaging." *Cell* 159(4): 896–910. http://www.sciencedirect.com/science/article/pii/S0092867414012975 (October 30, 2014).

Richardson, DS, and JW Lichtman. 2015. "Clarifying Tissue Clearing." *Cell*. http://www.sciencedirect.com/science/article/pii/S0092867415008375 (June 13, 2016).

Riga, Danai et al. 2014. "Optogenetic Dissection of Medial Prefrontal Cortex Circuitry." *Frontiers in systems neuroscience* 8: 230. http://www.ncbi.nlm.nih.gov/pubmed/25538574 (March 5, 2019).

Ringach, Dario L, Robert M Shapley, and Michael J Hawken. 2002. "Orientation Selectivity in Macaque V1: Diversity and Laminar Dependence." *The Journal of neuroscience : the official journal of the Society for Neuroscience* 22(13): 5639–51. http://www.ncbi.nlm.nih.gov/pubmed/12097515 (August 31, 2015).

Roberts, Angela C et al. 2007. "Forebrain Connectivity of the Prefrontal Cortex in the Marmoset Monkey (Callithrix Jacchus): An Anterograde and Retrograde Tract-Tracing Study." *The Journal of comparative neurology* 502(1): 86–112. http://www.ncbi.nlm.nih.gov/pubmed/17335041 (October 28, 2014).

Robinson, Gene E., Russell D. Fernald, and David F. Clayton. 2008. "Genes and Social Behavior." *Science* 322(5903): 896–900.

Rochefort, Nathalie L et al. 2011. "Development of Direction Selectivity in Mouse Cortical Neurons." *Neuron* 71(3): 425–32. http://www.sciencedirect.com/science/article/pii/S0896627311005186 (October 1, 2015).

Roe, Anna Wang, Kerstin Fritsches, and John D Pettigrew. 2005. "Optical Imaging of Functional Organization of V1 and V2 in Marmoset Visual Cortex." *The anatomical record. Part A, Discoveries in molecular, cellular, and evolutionary biology* 287(2): 1213–25. http://www.ncbi.nlm.nih.gov/pubmed/16235264 (August 30, 2015).

Rosa, Marcello G.P., Kerstin A. Fritsches, and Guy N. Elston. 1997. "The Second Visual Area in the Marmoset Monkey: Visuotopic Organisation, Magnification Factors, Architectonical Boundaries, and Modularity." *The Journal of Comparative Neurology* 387(4): 547–67. http://doi.wiley.com/10.1002/%28SICI%291096-9861%2819971103%29387%3A4%3C547%3A%3AAID-CNE6%3E3.0.CO%3B2-2 (September 28, 2018).

Ross, K. G. 2001. "Molecular Ecology of Social Behaviour: Analyses of Breeding Systems and Genetic Structure." *Molecular Ecology* 10(2): 265–84.

Rossion, Bruno, Bernard Hanseeuw, and Laurence Dricot. 2012. "Defining Face Perception Areas in the Human Brain: A Large-Scale Factorial FMRI Face Localizer Analysis." *Brain and cognition* 79(2): 138–57. http://www.sciencedirect.com/science/article/pii/S0278262612000024 (August 31, 2015).

Saleem, Kadharbatcha S., and Nikos K. Logothetis. 2012. *A Combined MRI and Histology Atlas of the Rhesus Monkey Brain in Stereotaxic Coordinates*. Academic Press.

Sanz, Elisenda et al. 2009. "Cell-Type-Specific Isolation of Ribosome-Associated MRNA from Complex Tissues." *Proceedings of the National Academy of Sciences of the United States of America* 106(33): 13939–44.

Sasaki, Erika. 2015. "Prospects for Genetically Modified Non-Human Primate Models, Including the Common Marmoset." *Neuroscience Research* 93: 110–15. http://www.sciencedirect.com/science/article/pii/S0168010215000292 (March 15, 2015).

Sawada, K. et al. 2014. "Fetal Sulcation and Gyrification in Common Marmosets (Callithrix Jacchus) Obtained by Ex Vivo Magnetic Resonance Imaging." *Neuroscience* 257: 158–74. https://www.sciencedirect.com/science/article/pii/S0306452213009202 (January 6, 2020).

Scheper, Wiep, and Jeroen J.M. Hoozemans. 2015. "The Unfolded Protein Response in Neurodegenerative Diseases: A Neuropathological Perspective." *Acta Neuropathologica* 130(3): 315–31.

Schiel, Nicola, and Antonio Souto. 2017. "The Common Marmoset: An Overview of Its Natural History, Ecology and Behavior." *Developmental Neurobiology* 77(3): 244–62. http://doi.wiley.com/10.1002/dneu.22458 (September 5, 2017).

Schilman, Eduardo A. et al. 2008. "The Orbital Cortex in Rats Topographically Projects to Central Parts of the Caudate-Putamen Complex." *Neuroscience Letters* 432(1): 40–45.

Schmidt, Eric F et al. 2012. "Identification of the Cortical Neurons That Mediate Antidepressant Responses." *Cell* 149(5): 1152–63. http://www.ncbi.nlm.nih.gov/pubmed/22632977.

Schneeberger, Marc et al. 2018. "Functional Analysis Reveals Differential Effects of Glutamate and MCH Neuropeptide in MCH Neurons." *Molecular Metabolism* 13: 83–89.

Seo, J. S. et al. 2017. "Cellular and Molecular Basis for Stress-Induced Depression." *Molecular Psychiatry* 22(10): 1440–47.

Sergushichev, Alexey A. 2016. "An Algorithm for Fast Preranked Gene Set Enrichment Analysis Using Cumulative Statistic Calculation." *bioRxiv*: 060012. http://dx.doi.org/10.1101/060012%0Ahttps://www.biorxiv.org/content/10.1101/060012v1 (April 25, 2020).

Shah, Sheel et al. 2016. "Single-Molecule RNA Detection at Depth by Hybridization Chain Reaction and Tissue Hydrogel Embedding and Clearing." https://www.moleculartechnologies.org/supp/shah16.pdf (May 28, 2019).

Shapley, Robert, Michael Hawken, and Dario L Ringach. 2003. "Dynamics of Orientation Selectivity in the Primary Visual Cortex and the Importance of Cortical Inhibition." *Neuron* 38(5): 689–99. http://www.ncbi.nlm.nih.gov/pubmed/12797955 (August 30, 2015).

Shmuel, Amir et al. 2005. "Retinotopic Axis Specificity and Selective Clustering of Feedback Projections from V2 to V1 in the Owl Monkey." *The Journal of neuroscience : the official journal of the Society for Neuroscience* 25(8): 2117–31. http://www.ncbi.nlm.nih.gov/pubmed/15728852 (August 28, 2015).

Shrestha, Prerana, Awni Mousa, and Nathaniel Heintz. 2015. "Layer 2/3 Pyramidal Cells in the Medial Prefrontal Cortex Moderate Stress Induced Depressive Behaviors." *eLife* 4. http://www.ncbi.nlm.nih.gov/pubmed/26371510.

Silverman, Jill L., Mu Yang, Catherine Lord, and Jacqueline N. Crawley. 2010. "Behavioural Phenotyping Assays for Mouse Models of Autism." *Nature Reviews Neuroscience* 11(7): 490–502.

Skuse, David H., and Louise Gallagher. 2011. "Genetic Influences on Social Cognition." *Pediatric Research* 69(5 PART 2): 85–91.

Sliwa, J, and W A Freiwald. 2017. "A Dedicated Network for Social Interaction Processing in the Primate Brain." *Science (New York, N.Y.)* 356(6339): 745–49. http://www.ncbi.nlm.nih.gov/pubmed/28522533.

Smith, C A, H D Moore, and J P Hearn. 1987. "The Ultrastructure of Early Implantation in the Marmoset Monkey (Callithrix Jacchus)." *Anatomy and embryology* 175(3): 399–410. http://www.ncbi.nlm.nih.gov/pubmed/3103485 (November 12, 2019).

Solomon, Samuel G, and Marcello G P Rosa. 2014. "A Simpler Primate Brain: The Visual System of the Marmoset Monkey." *Frontiers in neural circuits* 8: 96. http://journal.frontiersin.org/article/10.3389/fncir.2014.00096/abstract (July 13, 2015).

Sousa, André M.M. et al. 2017. "Evolution of the Human Nervous System Function, Structure, and Development." *Cell* 170(2): 226–47. http://www.ncbi.nlm.nih.gov/pubmed/28708995 (February 11, 2020).

Stanley, Damian A., and Ralph Adolphs. 2013. "Toward a Neural Basis for Social Behavior." *Neuron* 80(3): 816–26.

Stanley, Sarah et al. 2013. "Profiling of Glucose-Sensing Neurons Reveals That Ghrh Neurons Are Activated by Hypoglycemia." *Cell Metabolism* 18(4): 596–607.

Stojanoski, B., and R. Cusack. 2014. "Time to Wave Good-Bye to Phase Scrambling: Creating Controlled Scrambled Images Using Diffeomorphic Transformations." *Journal of Vision* 14(12): 6–6. http://jov.arvojournals.org/Article.aspx?doi=10.1167/14.12.6 (August 30, 2018).

Tan, A. Y. Y. et al. 2011. "Orientation Selectivity of Synaptic Input to Neurons in Mouse and Cat Primary Visual Cortex." *Journal of Neuroscience* 31(34): 12339–50. http://www.jneurosci.org/content/31/34/12339.short (October 1, 2015).

Tanaka, K. 2003. "Columns for Complex Visual Object Features in the Inferotemporal Cortex: Clustering of Cells with Similar but Slightly Different Stimulus Selectivities." *Cerebral Cortex* 13(1): 90–99. http://cercor.oxfordjournals.org/content/13/1/90.abstract (October 2, 2015).

Tardif, Suzette D. et al. 1998. "Estimation of Gestational Ages in the Common Marmoset (Callithrix Jacchus) from Published Prenatal Growth Curves." *Journal of Medical Primatology* 27(1): 28–32. http://doi.wiley.com/10.1111/j.1600-0684.1998.tb00065.x (November 11, 2019).

Tervo, D. Gowanlock R., Bum-Yeol Hwang, Sarada Viswanathan, Thomas Gaj, Maria Lavzin, Kimberly D. Ritola, et al. 2016. "A Designer AAV Variant Permits Efficient Retrograde Access to Projection Neurons." *Neuron* 92(2): 372–82. http://linkinghub.elsevier.com/retrieve/pii/S0896627316305803 (October 25, 2016).

Tervo, D Gowanlock R, Bum-Yeol Hwang, Sarada Viswanathan, Thomas Gaj, Maria Lavzin, Kimberly D Ritola, et al. 2016. "A Designer AAV Variant Permits Efficient Retrograde Access to Projection Neurons." *Neuron* 92(2): 372–82. http://www.ncbi.nlm.nih.gov/pubmed/27720486.

Tomioka, Ikuo et al. 2017. "Generation of Transgenic Marmosets Using a Tetracyclin-Inducible Transgene Expression System as a Neurodegenerative Disease Model†." *Biology of Reproduction* 97(5): 772–80. http://academic.oup.com/biolreprod/article/97/5/772/4553515 (December 20, 2019).

Ts'O, Daniel Y., Anna Wang Roe, and Charles D. Gilbert. 2001. "A Hierarchy of the Functional Organization for Color, Form and Disparity in Primate Visual Area V2." In *Vision Research*, Pergamon, 1333–49.

Tsao, Doris Y, Sebastian Moeller, and Winrich A Freiwald. 2008. "Comparing Face Patch Systems in Macaques and Humans." *Proceedings of the National Academy of Sciences of the United States of America* 105(49): 19514–19. http://www.pubmedcentral.nih.gov/articlerender.fcgi?artid=2614792&tool=pmcentrez&rendertype=abstract (July 20, 2015).

Tsao, DY, and WA Freiwald. 2003. "Faces and Objects in Macaque Cerebral Cortex." *Nature* …. http://www.nature.com/neuro/journal/v6/n9/abs/nn1111.html (August 31, 2015).

Tsao, DY, WA Freiwald, RBH Tootell, and MS Livingstone. 2006. "A Cortical Region Consisting Entirely of Face-Selective Cells." *Science*. http://www.sciencemag.org/content/311/5761/670.short (August 31, 2015).

Tsao, DY, N Schweers, S Moeller, and WA Freiwald. 2008. "Patches of Face-Selective Cortex in the Macaque Frontal Lobe." *Nature neuroscience*. http://www.nature.com/articles/nn.2158 (August 31, 2015).

Uemura, M et al. 2018. "Optimization of a GCaMP Expression System for Functional Calcium Imagining in the Marmoset Brain." In *Society for Neuroscience*, https://www.abstractsonline.com/pp8/#!/4649/presentation/15894 (April 30, 2020).

Valverde Salzmann, M. F., A. Bartels, N. K. Logothetis, and A. Schuz. 2012. "Color Blobs in Cortical Areas V1 and V2 of the New World Monkey Callithrix Jacchus, Revealed by Non-Differential Optical Imaging." *Journal of Neuroscience* 32(23): 7881–94. http://www.ncbi.nlm.nih.gov/pubmed/22674264 (December 4, 2017).

Valverde Salzmann, Matthias F, Damian J Wallace, Nikos K Logothetis, and Almut Schüz. 2011. "Multimodal Vessel Mapping for Precise Large Area Alignment of Functional Optical Imaging Data to Neuroanatomical Preparations in Marmosets." *Journal of neuroscience methods* 201(1): 159–72. http://www.sciencedirect.com/science/article/pii/S0165027011004584 (August 30, 2015).

Venken, Koen J.T., and Hugo J. Bellen. 2007. "Transgenesis Upgrades for Drosophila Melanogaster." *Development* 134(20): 3571–84.

Verwoerd-Dikkeboom, C.M. et al. 2008. "Embryonic Staging Using a 3D Virtual Reality System." *Human Reproduction* 23(7): 1479–84. http://www.ncbi.nlm.nih.gov/pubmed/18296447 (December 18, 2019).

Vialou, Vincent et al. 2014. "Prefrontal Cortical Circuit for Depression- and Anxiety-Related Behaviors Mediated by Cholecystokinin: Role of ΔFosB." *The Journal of neuroscience : the official journal of the Society for Neuroscience* 34(11): 3878–87. http://www.ncbi.nlm.nih.gov/pubmed/24623766 (March 5, 2019).

Vilella, Albert J. et al. 2009. "EnsemblCompara GeneTrees: Complete, Duplication-Aware Phylogenetic Trees in Vertebrates." *Genome Research* 19(2): 327–35.

van Vuuren, S. H. et al. 2012. "Size and Volume Charts of Fetal Kidney, Renal Pelvis and Adrenal Gland." *Ultrasound in Obstetrics & Gynecology* 40(6): 659–64. http://doi.wiley.com/10.1002/uog.11169 (December 18, 2019).

de Waal, Frans B.M. 1989. "The Myth of a Simple Relation between Space and Aggression in Captive Primates." *Zoo Biology* 8(1 S): 141–48.

Wang, G., K. Tanaka, and M. Tanifuji. 1996. "Optical Imaging of Functional Organization in the Monkey Inferotemporal Cortex." *Science* 272(5268): 1665–68. http://www.sciencemag.org/content/272/5268/1665.abstract?ijkey=3dab22228a2e982f91dedd1f2edbdf681ce259fc&keytype2=tf_ipsecsha (July 20, 2015).

Watakabe, Akiya et al. 2014. "Comparative Analyses of Adeno-Associated Viral Vector Serotypes 1, 2, 5, 8 and 9 in Marmoset, Mouse and Macaque Cerebral Cortex." *Neuroscience research*. http://www.sciencedirect.com/science/article/pii/S0168010214002132 (March 9, 2015).

Watson, Karli K., and Michael L. Platt. 2012. "Social Signals in Primate Orbitofrontal Cortex." *Current Biology* 22(23): 2268–73. http://www.ncbi.nlm.nih.gov/pubmed/23122847 (April 25, 2020).

Weiner, Kevin S, and Kalanit Grill-Spector. 2015. "The Evolution of Face Processing Networks." *Trends in cognitive sciences*. http://www.ncbi.nlm.nih.gov/pubmed/25840651 (April 15, 2015).

Wiesel, T.N., D.H. Hubel, and D.M.K. Lam. 1974. "Autoradiographic Demonstration of Ocular-Dominance Columns in the Monkey Striate Cortex by Means of Transneuronal Transport." *Brain Research* 79(2): 273–79. http://www.sciencedirect.com/science/article/pii/0006899374904168 (August 31, 2015).

Willenbockel, Verena et al. 2010. "Controlling Low-Level Image Properties: The SHINE Toolbox." *Behavior research methods* 42(3): 671–84. http://www.ncbi.nlm.nih.gov/pubmed/20805589 (July 20, 2016).

Willmore, Ben D.B., Ryan J. Prenger, and Jack L. Gallant. 2010. "Neural Representation of Natural Images in Visual Area V2." *Journal of Neuroscience* 30(6): 2102–14.

Wise, Steven P. 2008. "Forward Frontal Fields: Phylogeny and Fundamental Function." *Trends in Neurosciences* 31(12): 599–608.

Xiang, Chunchen, Yujia Wang, Han Zhang, and Fang Han. 2017. "The Role of Endoplasmic Reticulum Stress in Neurodegenerative Disease." *Apoptosis* 22(1): 1–26. http://www.ncbi.nlm.nih.gov/pubmed/27815720 (April 26, 2020).

Xu, Pan et al. 2019. "Medial Prefrontal Cortex in Neurological Diseases." *Physiological Genomics* 51(9): 432–42.

Yang, Lixia et al. 2018. "Metoprolol, N-Acetylcysteine, and Escitalopram Prevents Chronic Unpredictable Mild Stress-Induced Depression by Inhibition of Endoplasmic Reticulum Stress." *Frontiers in Psychiatry* 9: 696. https://www.frontiersin.org/article/10.3389/fpsyt.2018.00696/full (April 26, 2020).

Yang, Yaling, and Adrian Raine. 2009. "Prefrontal Structural and Functional Brain Imaging Findings in Antisocial, Violent, and Psychopathic Individuals: A Meta-Analysis." *Psychiatry Research - Neuroimaging* 174(2): 81–88.

Yue, Xiaomin, Irene S. Pourladian, Roger B.H. Tootell, and Leslie G. Ungerleider. 2014. "Curvature-Processing Network in Macaque Visual Cortex." *Proceedings of the National Academy of Sciences of the United States of America* 111(33): E3467–75.

Zhou, Pingzhu et al. 2013. "Interrogating Translational Efficiency and Lineage-Specific Transcriptomes Using Ribosome Affinity Purification." *Proceedings of the National Academy of Sciences of the United States of America* 110(38): 15395–400.

Ziemba, Corey M, Jeremy Freeman, J Anthony Movshon, and Eero P Simoncelli. 2016. "Selectivity and Tolerance for Visual Texture in Macaque V2." *Proceedings of the National Academy of Sciences of the United States of America* 113(22): E3140-9. http://www.ncbi.nlm.nih.gov/pubmed/27173899 (September 5, 2018).